Ecole Doctorale de l'Université Blaise Pascal

Laboratoire de Physique Corpusculaire de Clermont-Ferrand

Mémoire d'Habilitation à Diriger des Recherches

Supersymmetry in the LHC era

Interplay between flavour physics, cosmology and collider physics

par

Farvah MAHMOUDI

Soutenance le 13 décembre 2012
à l'Université Blaise Pascal
devant la commission d'examen composée de :

Prof. Benjamin ALLANACH ..... Examinateur
Dr. Geneviève BELANGER ..... Rapporteur
Prof. Aldo DEANDREA ..... Rapporteur
Prof. Ulrich ELLWANGER ..... Rapporteur
Dr. Michelangelo MANGANO ..... Examinateur
Prof. Jean ORLOFF ..... Examinateur
Dr. Dirk ZERWAS ..... Examinateur

Contents

Prelude

During my Ph.D. thesis at LAPTH (Annecy, France) I worked in the field of phenomenology of colliders and mainly focused on QCD loop calculations. In particular we applied the methods we developed to the calculation of the $gg \longrightarrow \gamma\gamma g$ process, which is an important background for the Higgs boson search at the LHC.

After my Ph.D., I joined the theoretical particle group at IPNL (Lyon, France) as postdoc and started working on the phenomenology of supersymmetry. After this period, I joined the Physics Department at Mount Allison University (Canada) where I worked on the possibility to constrain supersymmetric scenarios with the isospin asymmetry of $B \to K^*\gamma$ decays. The results we obtained were very encouraging, as we found that this asymmetry was at least as constraining as the inclusive branching fraction of $B \to X_s\gamma$. I moved then to Uppsala University, where I continued working on flavour physics, two-Higgs doublet model and supersymmetry. At that time, I designed and wrote the `SuperIso` public program, which was first developed in order to provide a precise calculation of the isospin asymmetry in $B \to K^*\gamma$ and the branching fraction of $B \to X_s\gamma$ in the MSSM, but rapidly included many other observables such as the $B_s \to \mu^+\mu^-$ and $B_u \to \tau\nu_\tau$ branching ratios and the anomalous magnetic moment of the muon. In parallel, I was also working on the Randall-Sundrum model, a 5-dimensional model with the fifth dimension, a slice of anti-de Sitter spacetime with strong curvature, compactified (to a size comparable to the Planck length) on a S_1/Z_2 orbifold. In the Bulk Randall-Sundrum model, the Kaluza-Klein (KK) excitations of the gauge bosons are the primary signatures. In particular, the search for the KK excitation of the gluon at hadron colliders is of great importance in testing this model. In this context, we obtained the first direct collider bound from Tevatron on the mass of the KK gluon to be 770 GeV, and calculated the production cross section of $pp \to KKg$ both through $q\bar{q}$ annihilation and gluon fusion (at loop level). These studies will not be covered in this manuscript.

The `SuperIso` program was further developed by addition of interfaces with many other MSSM programs, new models and observables, and improved precision for many calculations. Then with Alexandre Arbey, we started implementing in `SuperIso` the calculation of the relic density (`SuperIso Relic`), in order to analyse the influence of cosmological assumptions on the relic density constraints in supersymmetry and astonishingly found that cosmological models can change the computed relic density by orders of magnitude.

I was recruited as a Maître de Conférences in 2008 at Université Blaise Pascal (Clermont-Ferrand, France) where I joined the theory group at LPC. I extended my research interests, working simultaneously on flavour physics, predictions for high-p_T physics at the LHC and

dark matter, still continuing the development of `SuperIso`. In 2010, I was appointed CERN research fellow, and I joined the TH Division. That was a very interesting period to be at CERN, since the LHC had only (re-)started a few months before. Taking advantage of the CERN cosmopolitan environment, I could establish new collaborations on LHC related topics. Together with other colleagues, we started the seminar series "Collider Cross Talks", which encourages cross-talking between theorists and experimentalists. This seminar series has proved its interest and is still very active.

In 2011, in collaboration with Alexandre Arbey and Marco Battaglia, we started setting-up a complex machinery to study the implications of the ATLAS and CMS results on the MSSM, considering also the information from flavour physics and dark matter sectors. With `SuperIso` as the central core, we built up many interfaces to other codes, starting from the spectrum generation all the way to the calculation of the constraints, SUSY and Higgs decays and cross sections, event generation and detector simulation. After the publication of our first SUSY results, the evidence for a new particle decaying to two photons, compatible with the SM Higgs boson, was announced in December 2011. Our collaboration was joined by Abdelhak Djouadi, and we started working on the consequences of the Higgs search results in the MSSM, in combination with the constraints from the other sectors. The discovery of the new particle was confirmed in July 2012 and we further studied the implications of the new results. These studies revealed important consequences from the Higgs search results on the MSSM and we look forward to the final results of the LHC 8 TeV run.

The purpose of this manuscript is not to report a complete overview of my research projects, but rather to focus on a selection of the results obtained in supersymmetry since the start of the LHC.

Introduction

Supersymmetry (SUSY) has emerged over the past decades as possibly the best motivated model of new physics beyond the Standard Model (SM). Together with stabilising the masses at the electroweak scale, it provides gauge coupling unification and viable candidates for cold dark matter. Expectations for an observation of supersymmetric partners of the strongly interacting SM particles in the early stage of the LHC run have been high. In fact, global fits to constrained SUSY models, such as the CMSSM, including data from flavour physics, lower energy experiments and relic dark matter density have favoured SUSY particle masses below, or around, 1 TeV. Recent searches for supersymmetric particles by the ATLAS and CMS experiments at the LHC have now excluded most of this portion of the parameter space for these models, raising questions about the range of SUSY particle masses still allowed by the present data. Several studies have been carried out to evaluate the impact of LHC and other data on SUSY parameters. Most of these studies considered the highly constrained models with a small number of free parameters and large correlations between the masses of supersymmetric particles, which had been used for earlier benchmark studies and model parameter fits. In these constrained models, the LHC searches have resulted in a significant exclusion of masses at, or beyond, 1 TeV for the majority of SUSY particles. However, these models are not representative of a generic minimal supersymmetric extension of the Standard Model (MSSM), where the particle mass parameters are independent. The phenomenological MSSM (pMSSM), with its 19-parameter phase space, was proposed to reduce the theoretical prejudices of these constraints.

In this report, I will describe my work in the context of Supersymmetry in light of flavour physics, cosmology and collider physics. In Chapter 1, I will first focus on flavour physics observables and their constraints on new physics, in a model-independent way and in supersymmetry. In Chapter 2, I will discuss the dark matter data and their consequences on supersymmetric model. In Chapter 3, I will focus on the LHC results for SUSY and Higgs searches, and the important constraints we obtain when combining them with the limits from flavour physics and dark matter. I will finally present my future projects. The two appendices contain a brief description of the `SuperIso` and `SuperIso Relic` programs.

Chapter 1

Flavour physics

At the end of the B factories at SLAC (BaBar experiment) and at KEK (Belle experiment) and of the Tevatron B physics experiments, all present measurements in flavour physics are consistent with the simple Cabibbo-Kobayashi-Maskawa (CKM) theory of the Standard Model (SM). The recent measurements by the high-statistics LHCb experiment have not changed this feature. In principle (loop-induced) flavour changing neutral current (FCNC) processes like $\bar{B} \to X_s\gamma$ offer high sensitivity to new physics (NP) due to the simple fact that additional contributions to the decay rate, in which SM particles are replaced by new particles such as the supersymmetric charginos or gluinos, are not suppressed by the loop factor $\alpha/4\pi$ relative to the SM contribution.

The FCNC decays therefore provide information about the SM and its extensions via virtual effects to scales presently not accessible by the direct search for new particles. Thus, the information offered by the FCNC is complementary to the one provided by the high-p_T experiments ATLAS and CMS. It is also obvious, that the indirect information on NP by FCNC (even if SM-like) will be most valuable when the general nature of NP will be identified in the direct search, especially when the mass scale of NP will be fixed.

Indeed, in the SM the Glashow-Iliopoulos-Maiani (GIM) mechanism, small CKM elements and often helicity, all suppress FCNC processes. These suppression factors stem from the particle content of the SM and the unexplained smallness of most Yukawa couplings and are absent in generic extensions of the SM. Hence FCNCs are an excellent testing ground to probe new physics up to scales of 100 TeV, depending on the model. As a consequence, the present data of the B physics experiments already imply significant restrictions for the parameter space of new physics models – as we will explicitly discuss in this chapter – and lead to important clues for the direct search for new particles and for model building beyond the SM.

In the context of supersymmetric (SUSY) extensions of the SM, the measurements of rare decays such as $B \to X_s\gamma$ and the purely leptonic decay $B_s \to \mu\mu$ provide important constraints on the masses of new particles which are too heavy to be produced directly.

In this chapter, after discussing briefly the theoretical framework and flavour observables we first investigate the impact the recent measurements of the rare decays of beauty mesons in a model independent way and then show the constraints in supersymmetry.

1.1 Effective Hamiltonian

The effective Hamiltonian describing the $b \to s$ transitions has the following generic structure:

$$\mathcal{H}_{\text{eff}} = -\frac{4G_F}{\sqrt{2}} V_{tb} V_{ts}^* \Big(\sum_{i=1\cdots 10} \big(C_i(\mu) O_i(\mu) + C_i'(\mu) O_i'(\mu) \big) \Big) \,, \tag{1.1}$$

where $O_i(\mu)$ are the relevant operators and $C_i(\mu)$ the corresponding Wilson coefficients evaluated at the scale μ which encode short-distance physics. The primed operators are chirality flipped compared to the non-primed operators, and they are highly suppressed in the SM. Contributions from physics beyond the SM to the observables can be described by the modification of Wilson coefficients or by the addition of new operators. The most relevant operators in rare radiative, semileptonic and leptonic B decays are:

$$\begin{aligned}
O_1 &= (\bar{s}\gamma_\mu T^a P_L c)(\bar{c}\gamma^\mu T^a P_L b) \,, & O_2 &= (\bar{s}\gamma_\mu P_L c)(\bar{c}\gamma^\mu P_L b) \,, \\
O_3 &= (\bar{s}\gamma_\mu P_L b) \sum_q (\bar{q}\gamma^\mu q) \,, & O_4 &= (\bar{s}\gamma_\mu T^a P_L b) \sum_q (\bar{q}\gamma^\mu T^a q) \,, \\
O_5 &= (\bar{s}\gamma_{\mu_1}\gamma_{\mu_2}\gamma_{\mu_3} P_L b) \sum_q (\bar{q}\gamma^{\mu_1}\gamma^{\mu_2}\gamma^{\mu_3} q) \,, & O_6 &= (\bar{s}\gamma_{\mu_1}\gamma_{\mu_2}\gamma_{\mu_3} T^a P_L b) \sum_q (\bar{q}\gamma^{\mu_1}\gamma^{\mu_2}\gamma^{\mu_3} T^a q) \,, \\
O_7 &= \frac{e}{(4\pi)^2} m_b (\bar{s}\sigma^{\mu\nu} P_R b) F_{\mu\nu} \,, & O_8 &= \frac{g}{(4\pi)^2} m_b (\bar{s}\sigma^{\mu\nu} T^a P_R b) G^a_{\mu\nu} \,, \\
O_9 &= \frac{e^2}{(4\pi)^2} (\bar{s}\gamma^\mu P_L b)(\bar{\ell}\gamma_\mu \ell) \,, & O_{10} &= \frac{e^2}{(4\pi)^2} (\bar{s}\gamma^\mu P_L b)(\bar{\ell}\gamma_\mu\gamma_5 \ell) \,, \\
Q_1 &= \frac{e^2}{(4\pi)^2} (\bar{s} P_R b)(\bar{\ell}\,\ell) \,, & Q_2 &= \frac{e^2}{(4\pi)^2} (\bar{s} P_R b)(\bar{\ell}\gamma_5 \ell) \,,
\end{aligned} \tag{1.2}$$

where Q_1 and Q_2 are the scalar and pseudo-scalar operators arising in new physics scenarios.

The Wilson coefficients $C_i(\mu)$ are calculated at scale $\mu \sim \mathcal{O}(M_W)$ by requiring matching between the effective and full theories. They can be expanded perturbatively:

$$C_i(\mu) = C_i^{(0)}(\mu) + \frac{\alpha_s(\mu)}{4\pi} C_i^{(1)}(\mu) + \cdots \tag{1.3}$$

and are subsequently evolved to scale $\mu \sim \mathcal{O}(m_b)$ at which they can be used to calculate the flavour observables, using the renormalisation group equations:

$$\mu \frac{d}{d\mu} C_i(\mu) = C_j(\mu) \gamma_{ji}(\mu) \tag{1.4}$$

driven by the anomalous dimension matrix $\hat{\gamma}(\mu)$:

$$\hat{\gamma}(\mu) = \frac{\alpha_s(\mu)}{4\pi} \hat{\gamma}^{(0)} + \frac{\alpha_s^2(\mu)}{(4\pi)^2} \hat{\gamma}^{(1)} + \cdots \tag{1.5}$$

which are known to high accuracy. A review on effective methods is given in [1] and the analytical expressions for the Wilson coefficients and the renormalisation group equations can be found in [2].

1.2 Minimal Flavour Violation

The SM gauge interactions are universal in quark flavour space, this means the gauge sector of the SM is invariant under the flavour group G_{flavour} which can be decomposed as

$$G_{\text{flavour}} = U(3)_{Q_L} \times U(3)_{U_R} \times U(3)_{D_R} \,. \tag{1.6}$$

In the SM this symmetry is only broken by the Yukawa couplings. Any new physics model in which all flavour- and CP-violating interactions can be linked to the known Yukawa couplings is *minimal flavour violating*. In order to implement this principle in a renormalisation group invariant way [3], one promotes G_{flavour} to a symmetry of the theory by introducing auxiliary fields Y_U and Y_D transforming under $SU(3)^3_q$ as

$$Y_U \ (3, \bar{3}, 1) \ \text{ and } \ Y_D \ (3, 1, \bar{3}) \,. \tag{1.7}$$

The Yukawa couplings are then introduced as background fields of these so-called spurions transforming under the flavour group. An effective theory satisfies the criterion of MFV if all higher-dimensional, constructed from SM and Y fields, are invariant under CP and under the flavour group G_{flavour} [3].

In the construction of the effective field theory, operators with arbitrary powers of the dimensionless $Y_{U/D}$ have to be considered in principle. However, the specific structure of the SM, with its hierarchy of CKM matrix elements and quark masses, drastically reduces the number of numerically relevant operators. For example, it can be shown that in MFV models with one Higgs doublet, all FCNC processes with external d-type quarks are governed by the following combination of spurions due to the dominance of the top Yukawa coupling y_t:

$$(Y_U Y_U^\dagger)_{ij} \approx y_t^2 V_{3i}^* V_{3j} \,, \tag{1.8}$$

where a basis is used in which the d-type quark Yukawa is diagonal.

There are two strict predictions in this general class of models which have to be tested. First, the MFV hypothesis implies the usual CKM relations between $b \to s$, $b \to d$, and $s \to d$ transitions. For example, this relation allows for upper bounds on NP effects in $\text{BR}(\bar{B} \to X_d\gamma)$, and $\text{BR}(\bar{B} \to X_s\nu\bar{\nu})$ using experimental data or bounds from $\text{BR}(\bar{B} \to X_s\gamma)$, and $\text{BR}(K \to \pi^+\nu\bar{\nu})$, respectively. This emphasises the need for high-precision measurements of $b \to s/d$, but also of $s \to d$ transitions such as the rare kaon decay $K \to \pi\nu\bar{\nu}$.

The second prediction is that the CKM phase is the only source of CP violation. This implies that any phase measurement as in $B \to \phi K_s$ or $\Delta M_{B_{(s/d)}}$ is not sensitive to new physics. This is an additional assumption because the breaking of the flavour group and the discrete CP symmetry is in principle not connected at all. For example there is also a renormalisation-group invariant extension of the MFV concept allowing for flavour-blind phases as was shown in Ref. [4]; however these lead to non-trivial CP effects, which get strongly constrained by flavour-diagonal observables such as electric dipole moments. So within the model-independent effective field theory approach of MFV we keep the minimality condition regarding CP. But in specific models like MSSM the discussion of additional CP phases within the MFV framework makes sense.

Scenarios with two Higgs doublets with large $\tan\beta = \mathcal{O}(m_t/m_b)$ allow for the unification of top and bottom Yukawa couplings as predicted in grand-unified models and for sizeable new effects in helicity-suppressed decay models. There are more general MFV relations existing in this scenario due to the dominant role of scalar operators. However, since $\tan\beta$ is large, there is a new combination of spurions numerically relevant in the construction of higher-order MFV effective operators, namely

$$(Y_D Y_D^\dagger)_{ij} \approx y_d^2 \delta_{ij} \,, \tag{1.9}$$

which invalidates the general MFV relation between $b \to s/d$ and $s \to d$ transitions.

Finally, the MFV hypothesis solves the NP flavour problem only formally. One still has to find explicit dynamical structures to realise the MFV hypothesis like gauge-mediated supersymmetric theories. And of course the MFV hypothesis is not a theory of flavour; it does not explain the hierarchical structure of the CKM matrix and the large mass splittings of the SM fermions.

1.3 Observables and theoretical uncertainties

We present here the most important $\Delta F = 1$ observables in the context of search for new physics effects. We focus on their dependence on the (non-standard) Wilson coefficients of the MFV effective theory and on the main sources of the theoretical uncertainty.

1.3.1 Radiative decay $\bar{B} \to X_{s,d}\gamma$

The branching fraction of $B \to X_q\gamma$ ($q = s, d$) for a photon energy cut $E_\gamma > E_0$ can be parametrised as

$$\mathrm{BR}(B \to X_q\gamma)_{E_\gamma > E_0} = \mathrm{BR}(B \to X_c e\bar{\nu})_{\mathrm{exp}} \, \frac{6\alpha_{\mathrm{em}}}{\pi C} \left| \frac{V_{tq}^* V_{tb}}{V_{cb}} \right|^2 \Big[P(E_0) + N(E_0) \Big] \,, \tag{1.10}$$

where $\alpha_{\mathrm{em}} = \alpha_{\mathrm{em}}^{\text{on shell}}$, $C = |V_{ub}|^2/|V_{cb}|^2 \times \Gamma[B \to X_c e\bar{\nu}]/\Gamma[B \to X_u e\bar{\nu}]$ and $P(E_0)$ and $N(E_0)$ denote the perturbative and nonperturbative contributions, respectively. The latter are normalised to the charmless semileptonic rate to separate the charm dependence. The perturbative part of the branching ratio of $\bar{B} \to X_s\gamma$ is known to NNLL precision [5], while the nonperturbative corrections are now estimated to be well below 10% [6]. The overall uncertainty consists of nonperturbative (5%), parametric (3%), perturbative (scale) (3%) and m_c-interpolation ambiguity (3%), which are added in quadrature. An additional scheme dependence in the determination of the pre-factor C has been found [7]; it is within the perturbative uncertainty of 3%. The dependence of the dominating perturbative part from the Wilson coefficients can be parametrised at NNL [8]:

$$P(E_0) = P^{(0)}(\mu_b) + \left(\frac{\alpha_s(\mu_b)}{4\pi} \right) \Big[P_1^{(1)}(\mu_b) + P_2^{(1)}(E_0, \mu_b) \Big] + \mathcal{O}\left(\alpha_s^2(\mu_b)\right) \,, \tag{1.11}$$

where

$$\begin{aligned} P^{(0)}(\mu_b) &= \left[C_7^{(0)\text{eff}}(\mu_b)\right]^2 , \quad P_1^{(1)}(\mu_b) = 2\, C_7^{(0)\text{eff}}(\mu_b)\, C_7^{(1)\text{eff}}(\mu_b) , \\ P_2^{(1)}(E_0,\mu_b) &= \sum_{i,j=1}^{8} C_i^{(0)\text{eff}}(\mu_b)\; C_j^{(0)\text{eff}}(\mu_b)\; K_{ij}^{(1)}(E_0,\mu_b) . \end{aligned} \tag{1.12}$$

The functions $K_{ij}^{(1)}$ can be found in Ref. [8]. The effective Wilson coefficients are given in [2]. We stress that we use NNLL precision (means inclusion of $\mathcal{O}\left(\alpha_s^2(\mu_b)\right)$ terms) in our numerical analysis.

The branching ratio of $\bar{B} \to X_d\gamma$ is only known to NLL QCD precision [4]. The error at this order is dominated by a large scale renormalisation uncertainty of more than 12% and by uncertainties due to CKM matrix elements of 10%.

1.3.2 Isospin asymmetry $\Delta_0(B \to K^*\gamma)$

Another important observable which is already measured is the isospin-breaking ratio in $B \to K^*\gamma$ decays. It arises when the photon is emitted from the spectator quark:

$$\Delta_{0\pm} = \frac{\Gamma(\bar{B}^0 \to \bar{K}^{*0}\gamma) - \Gamma(B^\pm \to K^{*\pm}\gamma)}{\Gamma(\bar{B}^0 \to \bar{K}^{*0}\gamma) + \Gamma(B^\pm \to K^{*\pm}\gamma)} , \tag{1.13}$$

where the partial decay rates are CP-averaged. In the SM spectator-dependent effects enter only at the order Λ/m_b, whereas isospin-breaking in the form factors is expected to be a negligible effect. Therefore, the SM prediction is as small as $\mathcal{O}(8\%)$. Moreover, a part of the Λ/m_b (leading) contribution cannot be calculated within the QCD factorisation approach which leads to a large uncertainty [9]. However, the ratio is shown to be especially sensitive to NP effects in the penguin sector. The isospin asymmetry can be written as [9]:

$$\Delta_0 = \text{Re}(b_d - b_u) , \tag{1.14}$$

where the spectator-dependent coefficients b_q take the form:

$$b_q = \frac{12\pi^2 f_B\, Q_q}{m_b\, T_1^{B\to K^*} a_7^c} \left(\frac{f_{K^*}^\perp}{m_b}\, K_1 + \frac{f_{K^*} m_{K^*}}{6\lambda_B m_B}\, K_{2q} \right) , \tag{1.15}$$

in which f_B, $f_{K^*}^\perp$ and f_{K^*} are decay constants of the B and K^* mesons, $T_1^{B\to K^*}$ is a form factor in the decomposition of the $B \to K^*$ matrix element of the tensor current and λ_B is an hadronic parameter defined in [9]. The coefficient a_7^c reads [10]:

$$\begin{aligned} a_7^c(K^*\gamma) &= C_7(\mu_b) + \frac{\alpha_s(\mu_b) C_F}{4\pi}\Big[C_2(\mu_b) G_2(x_{cb}) + C_8(\mu_b) G_8\Big] \\ &\quad + \frac{\alpha_s(\mu_h) C_F}{4\pi}\Big[C_2(\mu_h) H_2(x_{cb}) + C_8(\mu_h) H_8\Big] , \end{aligned} \tag{1.16}$$

where $\mu_h = \sqrt{\Lambda_h \mu_b}$ is the spectator scale. The functions G_2, G_8, H_2, and H_8 can be found in Ref. [10]. The functions K_1 and K_{2q} can be written in terms of the Wilson coefficients C_i at scale μ_b [9]:

$$\begin{aligned} K_1 &= -\left(C_6(\mu_b) + \frac{C_5(\mu_b)}{N}\right) F_\perp + \frac{C_F}{N}\,\frac{\alpha_s(\mu_b)}{4\pi}\,\left\{\left(\frac{m_b}{m_B}\right)^2 C_8(\mu_b)\, X_\perp \right. \\ &\quad \left. -C_2(\mu_b)\left[\left(\frac{4}{3}\ln\frac{m_b}{\mu_b} + \frac{2}{3}\right) F_\perp - G_\perp(x_{cb})\right] + r_1\right\}\,, \end{aligned} \tag{1.17}$$

$$\begin{aligned} K_{2q} &= \frac{V_{us}^* V_{ub}}{V_{cs}^* V_{cb}}\left(C_2(\mu_b) + \frac{C_1(\mu_b)}{N}\right)\delta_{qu} + \left(C_4(\mu_b) + \frac{C_3(\mu_b)}{N}\right) \\ &\quad + \frac{C_F}{N}\,\frac{\alpha_s(\mu_b)}{4\pi}\left[C_2(\mu_b)\left(\frac{4}{3}\ln\frac{m_b}{\mu_b} + \frac{2}{3} - H_\perp(x_{cb})\right) + r_2\right]\,, \end{aligned} \tag{1.18}$$

where $x_{cb} = \dfrac{m_c^2}{m_b^2}$ and $N = 3$ and $C_F = 4/3$ are colour factors. The convolution integrals of the hard-scattering kernels with the meson distribution amplitudes $F_\perp, G_\perp, H_\perp$, and $X_\perp$ can be found in Ref. [9], as well as the residual NLO corrections r_1 and r_2.

The largest theoretical uncertainties from input parameters come from λ_B (25%), the integral $X_\perp$ (12%), and the decay constant f_B (10%). The perturbative uncertainty is about 12%.

1.3.3 Leptonic decays $B_{s,d} \to \mu^+\mu^-$

Of much interest for the LHC experiments is the unobserved decay $B_s \to \mu^+\mu^-$. This rare decay proceeds via Z^0 penguin and box diagrams in the SM. It is highly helicity-suppressed. However, in the MSSM for large values of $\tan\beta$ this decay can receive large contributions.

The average branching ratio is expressed as [2, 11]:

$$\begin{aligned} BR(B_s \to \mu^+\mu^-) &= \frac{G_F^2\alpha^2}{64\pi^3} f_{B_s}^2 m_{B_s}^3 |V_{tb}V_{ts}^*|^2 \tau_{B_s}\sqrt{1 - \frac{4m_\mu^2}{m_{B_s}^2}} \\ &\quad \times \left\{\left(1 - \frac{4m_\mu^2}{m_{B_s}^2}\right)|C_{Q_1} - C'_{Q_1}|^2 + \left|(C_{Q_2} - C'_{Q_2}) + 2(C_{10} - C'_{10})\frac{m_\mu}{m_{B_s}}\right|^2\right\}, \end{aligned} \tag{1.19}$$

where f_{B_s} is the B_s decay constant, m_{B_s} is the B_s meson mass and τ_{B_s} is the B_s mean life. In the Standard Model, only C_{10} is non-vanishing and gets its largest contributions from a Z penguin top loop (75%), and from a charmed box diagram (24%) . With the inputs of Table 1.4, $C_{10} = -4.21$, from which $BR(B_s \to \mu^+\mu^-)|_{SM} = (3.53 \pm 0.38) \times 10^{-9}$ [12]. The latest experimental limit thus severely restraints the room for new physics, and its proximity with the 2σ upper value calls for a discussion of the uncertainties in this SM prediction.

The main theoretical uncertainty comes from f_{B_s}, which has recently been re-evaluated by independent lattice QCD groups of Table 1.1. Their 4.3% uncertainties agree, as do

Lattice QCD Group	Ref.	f_{B_s}	f_B
ETMC-11	[13]	232 ± 10 MeV	195 ± 12 MeV
Fermilab-MILC-11	[14, 15]	242 ± 9.5 MeV	197 ± 9 MeV
HPQCD-12	[16]	227 ± 10 MeV	191 ± 9 MeV
Average		234 ± 10 MeV	194 ± 10 MeV

Table 1.1: Average of lattice QCD results used in this work.

their results within these uncertainties, so that we have chosen an average of these three results in what follows. This implies a 8.7% uncertainty on the branching ratio. The most important parametric uncertainty comes from the CKM matrix element V_{ts} with 5%.

Within MFV, this decay receives contributions only from the effective operators C_{10} and $C_0^l = 2C_{Q_1} = -2C_{Q_2}$. These are free from the contamination of four-quark operators, making the generalisation to the $b \to d$ case straightforward. The $B_d \to \ell^+\ell^-$ rate can be obtained from the one of $B_s \to \ell^+\ell^-$ with the exchange (V_{ts}, m_{B_s}, m_s, f_{B_s}) $\to$ (V_{td}, m_{B_d}, m_d, f_{B_d}). This implies a very important MFV relation ($\mathcal{O}(m_d/m_s)$ are neglected),

$$\frac{\Gamma(B_s \to \ell^+\ell^-)}{\Gamma(B_d \to \ell^+\ell^-)} \approx \frac{f_{B_s} m_{B_s}}{f_{B_d} m_{B_d}} \left|\frac{V_{ts}}{V_{t_d}}\right|^2 . \tag{1.20}$$

There is a remark in order regarding the branching fraction of $B_s \to \mu^+\mu^-$. Its value provided by the experiments corresponds to an untagged value, while the theoretical predictions are CP-averaged. As pointed out recently in [17,18], the untagged branching ratio is related to the CP-averaged one by:

$$\mathrm{BR}^{\mathrm{untag}}(B_s \to \mu^+\mu^-) = \left[\frac{1 + \mathcal{A}_{\Delta\Gamma}\, y_s}{1 - y_s^2}\right] \mathrm{BR}(B_s \to \mu^+\mu^-) , \tag{1.21}$$

where

$$y_s \equiv \frac{1}{2}\tau_{B_s}\Delta\Gamma_s = 0.088 \pm 0.014 , \tag{1.22}$$

and

$$\mathcal{A}_{\Delta\Gamma} = \frac{|P|^2\cos(2\varphi_P) - |S|^2\cos(2\varphi_S)}{|P|^2 + |S|^2} , \tag{1.23}$$

with

$$S \equiv \sqrt{1 - 4\frac{m_\mu^2}{M_{B_s}^2}}\, \frac{M_{B_s}^2}{2m_\mu}\, \frac{1}{m_b + m_s} \frac{C_0^l/2}{C_{10}^{SM}} , \tag{1.24}$$

$$P \equiv \frac{C_{10}}{C_{10}^{SM}} + \frac{M_{B_s}^2}{2m_\mu}\, \frac{1}{m_b + m_s} \frac{-C_0^l/2}{C_{10}^{SM}} , \tag{1.25}$$

and

$$\varphi_S = \arg(S) , \qquad \varphi_P = \arg(P) . \tag{1.26}$$

The corrected branching ratio can then be directly compared to the experimental result.

1.3.4 Inclusive decays $\bar{B} \to X_s\mu^+\mu^-$ and $\bar{B} \to X_s\tau^+\tau^-$

The decay $B \to X_s\ell^+\ell^-$ ($\ell = e, \mu, \tau$) is particularly attractive because it offers several kinematic observables. The angular decomposition of the decay rate provides three independent observables, H_T, H_A and H_L, from which one can extract the short-distance electroweak Wilson coefficients that test for NP:

$$\frac{d^3\Gamma}{dq^2\,dz} = \frac{3}{8}\Big[(1+z^2)H_T(q^2) + 2(1-z^2)H_L(q^2) + 2zH_A(q^2)\Big]\,. \tag{1.27}$$

Here $z = \cos\theta_\ell$ with θ_ℓ the angle between the negatively charged lepton and the $\bar{B}$ meson in the center-of-mass frame of the dilepton system, and q^2 is the dilepton mass squared. H_A is equivalent to the forward-backward asymmetry, and the dilepton-mass spectrum is given by $H_T + H_L$. The observables mainly constrain the Wilson coefficients $C_7^{\rm eff}$, $C_9^{\rm eff}$ and $C_{10}^{\rm eff}$.

One defines perturbatively dominated (means theoretically clean) observables within two dilepton-mass windows avoiding the region with the $c\bar{c}$ resonances: the low-q^2 region ($1\ \text{GeV}^2 < q^2 < 6\ \text{GeV}^2$) and the high-$q^2$ region ($q^2 > 14.4\ \text{GeV}^2$).

In order to show the dependence of the observables on the Wilson coefficients, we use the conventions of Ref. [19]. For the branching ratio within the MFV framework we find:

$$\begin{aligned}
\frac{d\text{BR}(B\to X_s\ell^+\ell^-)}{d\hat{s}} &= \text{BR}(B\to X_c\ell\bar{\nu})\frac{\alpha^2}{4\pi^2 f(z)\kappa(z)}\frac{|V_{tb}V_{ts}^*|^2}{|V_{cb}|^2}(1-\hat{s})^2\sqrt{1-\frac{4\hat{m}_\ell^2}{\hat{s}}} \\
&\times\Bigg\{|C_9^{new}|^2(1+\frac{2\hat{m}_\ell^2}{\hat{s}})(1+2\hat{s})\left(1+\frac{\alpha_s}{\pi}\tau_{99}(\hat{s})\right) + 4|C_7^{new}|^2(1+\frac{2\hat{m}_\ell^2}{\hat{s}})(1+\frac{2}{\hat{s}})\left(1+\frac{\alpha_s}{\pi}\tau_{77}(\hat{s})\right) \\
+\ & |C_{10}^{new}|^2[(1+2\hat{s})+\frac{2\hat{m}_\ell^2}{\hat{s}}(1-4\hat{s})]\left(1+\frac{\alpha_s}{\pi}\tau_{99}(\hat{s})\right) + 12\text{Re}(C_7^{new}C_9^{new*})(1+\frac{2\hat{m}_\ell^2}{\hat{s}})\left(1+\frac{\alpha_s}{\pi}\tau_{79}(\hat{s})\right) \\
+\ & \frac{3}{4}|C_0^l|^2(\hat{s}-2\hat{m}_\ell^2) - 3Re(C_{10}^{new}C_0^{\ell *})\hat{m}_\ell\Bigg\} + \delta^{brems}_{d\mathcal{B}/d\hat{s}} + \delta^{1/m_b^2}_{d\mathcal{B}/d\hat{s}} + \delta^{1/m_b^3}_{d\mathcal{B}/d\hat{s}} + \delta^{1/m_c^2}_{d\mathcal{B}/d\hat{s}} + \delta^{em}_{d\mathcal{B}/d\hat{s}}\,,
\end{aligned} \tag{1.28}$$

where the hat indicates a normalisation by m_b. The functions τ_i correspond to specific bremsstrahlung terms. The *new* Wilson coefficients are defined in Ref. [19]. As indicated, further (but finite) bremsstrahlung, electromagnetic and power corrections have to be added.

For the dependence of the forward-backward asymmetry on the Wilson coefficients we find within the MFV setting:

$$\begin{aligned}
A_{FB}(\hat{s}) &= \int_0^1 dz\frac{d^2\text{BR}}{d\hat{s}dz} - \int_{-1}^0 dz\frac{d^2\text{BR}}{d\hat{s}dz} = -\text{BR}(B\to X_c\ell\bar{\nu})\frac{3\alpha^2}{4\pi^2 f(z)\kappa(z)}\frac{|V_{tb}V_{ts}^*|^2}{|V_{cb}|^2}(1-\hat{s})^2\Big(1-\frac{4\hat{m}_\ell^2}{\hat{s}}\Big) \\
&\times\ \Bigg\{\text{Re}(C_9^{new}C_{10}^{new*})\hat{s}\left(1+\frac{\alpha_s}{\pi}\tau_{910}(\hat{s})\right) + 2\text{Re}(C_7^{new}C_{10}^{new*})\left(1+\frac{\alpha_s}{\pi}\tau_{710}(\hat{s})\right) \\
&+\ \text{Re}(\,(C_9^{new}/2 + C_7^{new})\,C_0^{\ell *})\hat{m}_\ell\Bigg\} + \delta_{A_{FB}}^{1/m_b^2}(\hat{s}) + \delta_{A_{FB}}^{1/m_c^2}(\hat{s}) + \delta_{A_{FB}}^{brems}(\hat{s}) + \delta_{A_{FB}}^{em}(\hat{s})\,.
\end{aligned} \tag{1.29}$$

In the low-q^2 region the theoretical uncertainty is around 7% for the branching ratio, however there is an additional 5% uncertainty due to non-local power corrections to be added [20]. In the high-q^2 region, one encounters the breakdown of the heavy-mass expansion at the endpoint. However, for an integrated high-q^2 spectrum an effective expansion exists in inverse powers of $m_b^{\rm eff} = m_b \times (1 - \sqrt{s_{\rm min}})$ rather than m_b. The resulting large theoretical uncertainties in the high-q^2 due to the power corrections of around 25% could be significantly reduced by normalising the $\bar{B} \to X_s \ell^+ \ell^-$ decay rate to the semileptonic $\bar{B} \to X_u \ell \bar{\nu}$ decay rate with the same q^2 cut [21]. For example, the uncertainty due to the dominating $1/m_b^3$ term would be reduced from 19% to 9%.

1.3.5 Exclusive decay $B \to K^* \mu\mu$

The exclusive semi-leptonic penguin modes offer a larger variety of experimentally accessible observables than do the inclusive ones, but the hadronic uncertainties in the theoretical predictions are in general larger.

The physics opportunities of $B \to K^* \ell\ell$ ($\ell = e, \mu, \tau$) decays depend strongly on the measurement of their angular distributions. This decay with K^* on the mass shell has a 4-fold differential distribution [22, 23]

$$\frac{d^4\Gamma[B \to K^*(\to K\pi)\ell\ell]}{dq^2\, d\cos\theta_l\, d\cos\theta_K\, d\phi} = \frac{9}{32\pi} \sum_i J_i(q^2)\, g_i(\theta_l, \theta_K, \phi) \,, \tag{1.30}$$

w.r.t. the dilepton invariant mass q^2 and the angles θ_l, θ_K, and ϕ. It offers 12 observables $J_i(q^2)$, from which all other known ones can be derived upon integration over appropriate combinations of angles.

The J_i depend on products of the eight theoretical complex K^* spin amplitudes A_i, $A^{L,R}_{\perp,\parallel,0}, A_t, A_S$. They are bi-linear functions of the spin amplitudes such as

$$J_s^1 = \frac{3}{4}\left[|A_\perp^L|^2 + |A_\parallel^L|^2 + |A_\perp^R|^2 + |A_\parallel^R|^2\right] \,, \tag{1.31}$$

with the expression for the eleven other J_i terms given for example in [23–25].

The dilepton invariant mass spectrum for $B \to K^* \ell^+ \ell^-$ can be recovered after integrating the 4-differential distribution over all angles, while the (normalised) forward-backward asymmetry $A_{\rm FB}$ can be defined after full ϕ and θ_{K^*} integration [26]:

$$\frac{d\Gamma}{dq^2} = \frac{3}{4}\left(J_1 - \frac{J_2}{3}\right), \quad A_{\rm FB}(q^2) \equiv \left[\int_{-1}^{0} - \int_{0}^{1}\right] d\cos\theta_l \, \frac{d^2\Gamma}{dq^2\, d\cos\theta_l} \Bigg/ \frac{d\Gamma}{dq^2} = -\frac{3}{8}\frac{J_6}{d\Gamma/dq^2} \,, \tag{1.32}$$

where $J_i \equiv 2J_i^s + J_i^c$. Moreover, the fraction of the longitudinal polarised K^* is given by $F_L = (3\, J_1^c - J_2^c)/(4\, d\Gamma/dq^2)$. These three observables represent the *early* ones, which have been measured already by the B factories and now with much better precision by the LHCb experiment.

With more luminosity, theoretically much cleaner angular observables will be available. In the low- and high-q^2 region it is always appropriate to design optimised observables

by using specifically chosen normalisations for the independent set of observables. In the low-q^2region, specific ratios of observables allow for a complete cancellation of the hadronic uncertainties due to the form factors in leading order and, thus, for a high increase in the sensitivity to new physics structures, for example the transversity amplitudes [25, 27]:

$$A_T^{(2)} = \frac{1}{2}\frac{J_3}{J_2^s}\ ,\ \ A_T^{(3)} = \sqrt{\frac{4J_4^2+\beta_l^2 J_7^2}{-2J_2^c(2J_2^s+J_3)}}\ ,\ \ A_T^{(4)} = \sqrt{\frac{\beta_l^2 J_5^2+4J_8^2}{4J_4^2+\beta_l^2 J_7^2}}\ . \tag{1.33}$$

In the high-q^2 region, two groups of ratios of observables can be constructed which dominantly depend either on short- or on long-distance physics [28, 29]. In addition to the $A_T^{(i)}$ observables some new transversity observables were proposed:

$$H_T^{(1)} = \frac{\sqrt{2}J_4}{\sqrt{-J_2^c\,(2J_2^s-J_3)}}\ ,\ \ H_T^{(2)} = \frac{\beta_l J_5}{\sqrt{-2J_2^c\,(2J_2^s+J_3)}}\ ,\ \ H_T^{(3)} = \frac{\beta_l J_6}{2\sqrt{(2J_2^s)^2-J_3^2}}\ . \tag{1.34}$$

$H_T^{(2,3)}$ in the high-q^2 region depend only on short-distance information in leading order, while F_L and $A_T^{(2,3)}$ depend only on long-distance quantities[1].

The theoretical treatment in the low- and high-q^2 is based on different theoretical concepts. Thus, the consistency of the consequences out of the two sets of measurements will allow for an important cross-check.

In the low-q^2 region, the up-to-date description of exclusive heavy-to-light $B \to K^*\ell^+\ell^-$ decays is the method of QCD-improved Factorisation (QCDF) and its field-theoretical formulation of Soft-Collinear Effective Theory (SCET). In the combined limit of a heavy b-quark and of an energetic K^* meson, the decay amplitude factorises to leading order in Λ/m_b and to all orders in α_s into process-independent nonperturbative quantities like $B \to K^*$ form factors and light-cone distribution amplitudes (LCDAs) of the heavy (light) mesons and perturbatively calculable quantities, which are known to $\mathcal{O}(\alpha_s^1)$ [30, 31]. Further, the seven a priori independent $B \to K^*$ QCD form factors reduce to two universal *soft* form factors $\xi_{\perp,\parallel}$ [32]. The factorisation formula applies well in the range of the dilepton mass range, $1\ \text{GeV}^2 < q^2 < 6\ \text{GeV}^2$.

Taking into account all these simplifications, the various K^* spin amplitudes at leading order in Λ_{QCD}/m_b and α_S turn out to be linear in the soft form factors $\xi_{\perp,\parallel}$ and also in the short-distance Wilson coefficients which allows to design a set of optimised observables in which any soft form factor dependence (and its corresponding uncertainty) cancels out for

[1] There are three observables which are already measured beyond the early observables mentioned above: $S_3 = (J_3+\bar{J}_3)/[d(\Gamma+\bar{\Gamma})/dq^2]$, A_{im}, and the isospin asymmetry, but all three observables have no significant impact on the MFV scenario yet.

all low dilepton masses q^2 at leading order in α_s and $\Lambda_{\rm QCD}/m_b$:

$$A_\perp^L R = \sqrt{2} N m_B (1-\hat{s}) \left[(C_9^{(\rm eff)} \mp C_{10}) + \frac{2\hat{m}_b}{\hat{s}} C_7^{(\rm eff)} \right] \xi_\perp(E_{K^*}) \,, \tag{1.35a}$$

$$A_\parallel^L R = -\sqrt{2} N m_B (1-\hat{s}) \left[(C_9^{(\rm eff)} \mp C_{10}) + \frac{2\hat{m}_b}{\hat{s}} C_7^{(\rm eff)} \right] \xi_\perp(E_{K^*}) \,, \tag{1.35b}$$

$$A_0^{L,R} = -\frac{N m_B}{2\hat{m}_{K^*}\sqrt{\hat{s}}} (1-\hat{s})^2 \left[(C_9^{(\rm eff)} \mp C_{10}) + 2\hat{m}_b C_7^{(\rm eff)} \right] \xi_\parallel(E_{K^*}) \,, \tag{1.35c}$$

$$A_t = \frac{N m_B}{\hat{m}_{K^*}\sqrt{\hat{s}}} (1-\hat{s})^2 \left[C_{10} - \frac{q^2}{4 m_\ell m_b} C_0^l \right] \xi_\parallel(E_{K^*}) \,, \tag{1.35d}$$

$$A_S = \frac{N m_B^2}{2\hat{m}_{K^*} m_b} (1-\hat{s})^2 \left[(-1) C_0^l \right] \xi_\parallel(E_{K^*}) \,, \tag{1.35e}$$

with $\hat{s} = q^2/m_B^2$, $\hat{m}_i = m_i/m_B$. Here we neglect terms of $\mathcal{O}(\hat{m}_{K^*}^2)$ but we include these terms in our numerical analysis. The factor N collects all pre-factors and can be found in Ref. [25, 27].

However, in the early observables, namely $d\Gamma/dq^2, A_{\rm FB}, F_{\rm L}$ there is still a large theoretical uncertainty due to the form factors which do not cancel out to first order in these cases.

Within the QCDF/SCET approach, a general, quantitative method to estimate the important $\Lambda_{\rm QCD}/m_b$ corrections to the heavy quark limit is missing. In semileptonic decays a simple dimensional estimate of 10% is often used. Under the assumption that the main part of the $\Lambda_{\rm QCD}/m_b$ corrections is included in the full form factors, the difference of the theoretical results using the full QCD form factors on one hand and the soft form factors on the other hand confirms this simple dimensional estimate. In fact, the comparison of the approaches leads to a 7% shift of the central value.

The low-hadronic recoil region is characterised by large values of the dilepton invariant mass $q^2 \gtrsim (14-15)$ GeV^2 above the two narrow resonances of J/ψ and $\psi(2S)$. It is shown that local operator product expansion is applicable ($q^2 \sim m_b^2$) [33, 34] and it allows to obtain the $B \to K^* \ell^+ \ell^-$ matrix element in a systematic expansion in α_s and in Λ/m_b. Most importantly, the leading power corrections are shown to be suppressed by $(\Lambda_{\rm QCD}/m_b)^2$ or $\alpha_s \Lambda_{\rm QCD}/m_b$ [34] and to contribute only at the few percent level. The only caveat is that heavy-to-light form factors are known only from extrapolations from LCSR calculations at low-q^2 at present. But this may improve in the future when direct lattice calculations in the high-q^2 are available.

There are improved Isgur-Wise relations between the form factors in leading power of Λ/m_b. Their application and the introduction of specific modified Wilson coefficients lead to simple expressions for the K^* spin amplitudes to leading order in $1/m_b$ in the low recoil region, for example we have [28]

$$A_{\perp}^{L,R} = +i\{(C_9^{\text{eff,mod}} \mp C_{10}) + \kappa\frac{2\hat{m}_b}{\hat{s}}\, C_7^{\text{eff,mod}}\} f_{\perp} \,, \tag{1.36}$$

$$A_{\parallel}^{L,R} = -i\{(C_9^{\text{eff,mod}} \mp C_{10}) + \kappa\frac{2\hat{m}_b}{\hat{s}}\, C_7^{\text{eff,mod}}\} f_{\parallel} \,, \tag{1.37}$$

$$A_{0}^{L,R} = -i\{(C_9^{\text{eff,mod}} \mp C_{10}) + \kappa\frac{2\hat{m}_b}{\hat{s}}\, C_7^{\text{eff,mod}}\} f_{0} \,, \tag{1.38}$$

where the form factors $f_\perp, f_\parallel$, and f_0 are linearly connected to the QCD form factors. The *modified* effective Wilson coefficients are introduced in Ref. [33]. Then, the three considered observables at leading order can be written in the high-q^2 region as [28]

$$\frac{\mathrm{d}\Gamma}{\mathrm{d}q^2} = 2\,\rho_1 \times (f_0^2 + f_\perp^2 + f_\parallel^2) \,, \;\; A_{\mathrm{FB}} = 3\,\frac{\rho_2}{\rho_1} \times \frac{f_\perp f_\parallel}{(f_0^2 + f_\perp^2 + f_\parallel^2)} \,, \quad F_{\mathrm{L}} = \frac{f_0^2}{f_0^2 + f_\perp^2 + f_\parallel^2} \,, \tag{1.39}$$

where only the two independent combinations of Wilson coefficients enter, namely

$$\rho_1 \equiv \left| C_9^{\text{eff}} + \kappa\frac{2\hat{m}_b}{\hat{s}} C_7^{\text{eff}} \right|^2 + |C_{10}|^2 \;\; , \;\; \rho_2 \equiv \mathrm{Re}\left(C_9^{\text{eff}} + \kappa\frac{2\hat{m}_b}{\hat{s}} C_7^{\text{eff}} \right) C_{10}^* \,. \tag{1.40}$$

ρ_1 and ρ_2 are shown to be largely μ-scale independent [33].

As mentioned above, the leading power corrections of the OPE arise at $\mathcal{O}(\alpha_s\Lambda/m_b, m_c^4/Q^4)$ and of the order of a few percent. The Λ/m_b corrections to the amplitudes from the form factor relations are parametrically suppressed as well, by small dipole coefficients, such that one can estimate the leading power correction from the form factor relations to the decay amplitudes of order $(2C_7^{\text{eff}}/C_9^{\text{eff}})\Lambda/m_b$. So in general, the dominant power corrections to the transversity amplitudes are of the order of a few percent.

1.3.6 Leptonic decay $B_u \to \tau\nu_\tau$

In the SM the purely leptonic decays of charged pseudoscalar mesons proceed via annihilation in the s-channel to a W boson. The decay rates are proportional to the lepton mass which arises from the chirality flip of the lepton required to conserve angular momentum. Such decays have traditionally been used to measure the decay constants of the pseudoscalar mesons, and thus provide an important test of lattice QCD calculations.

These purely leptonic decays are sensitive to charged Higgs boson ($H^\pm$) at the *tree level* and thus provide valuable probes of such particles which are complementary to constraints provided by loop-induced decays (e.g., $b \to s\gamma$). Importantly, in SUSY models the loop-induced decays are particularly sensitive to the sparticle spectrum and the assumptions made for the SUSY breaking sector, and thus the purely leptonic decays offer a more model-independent probe of parameters in the Higgs sector. The measurement of $B_u \to \tau\nu_\tau$ [35,36], although in rough agreement with the SM prediction, provides important constraints on the mass and couplings of $H^\pm$ from the Two Higgs Doublet Model (Type II) [37,38], with some dependence on SUSY parameters which enters at higher orders in perturbation theory. Improved measurements of $B_u \to \tau\nu_\tau$ (and first observation of $B_u \to \mu\nu_\mu$) are thus certainly

desirable and such decays play a prominent role in the physics case for a high luminosity flavour factory.

In the SM, the $W^\pm$ mediated diagram is helicity suppressed, whereas there is no such suppression for the scalar $H^\pm$ exchange, whose contribution is proportional to the b quark and τ lepton Yukawa couplings. In the limit of high $\tan\beta$ such Yukawa couplings are enhanced, and the contribution from $H^\pm$ can be comparable in magnitude to that of $W^\pm$. The leading order SM prediction for this decay is:

$$\mathrm{BR}(B_u \to \tau\nu_\tau)_{\mathrm{SM}} = \frac{G_F^2 f_B^2 |V_{ub}|^2}{8\pi\Gamma_B} m_B m_\tau^2 \left(1 - \frac{m_\tau^2}{m_B^2}\right)^2 , \tag{1.41}$$

while the New Physics contribution from $H^\pm$ is expressed through the ratio [37, 39, 40]

$$r_B \equiv \frac{\mathrm{BR}(B_u \to \tau\nu_\tau)_{\mathrm{MSSM}}}{\mathrm{BR}(B_u \to \tau\nu_\tau)_{\mathrm{SM}}} = \left[1 - \left(\frac{m_B^2}{M_{H^+}^2}\right) \frac{\tan^2\beta}{1 + \epsilon_0 \tan\beta}\right]^2 . \tag{1.42}$$

Here M_{H^+} is the mass of the charged Higgs boson, m_B is the mass of the B_u meson, Γ_B is the total decay width of the B_u meson, and G_F is the Fermi constant. The leading SUSY-QCD corrections are included in this expression through ϵ_0. The Yukawa couplings of the MSSM take the form of a 2HDM (Type II) at tree level, but at higher orders the structure becomes of the type 2HDM (Type III) in which ϵ_0 is a function of SUSY parameters [41–44] and $|\epsilon_0|$ can reach values of order 0.01. We use the average $f_B = 194 \pm 10$ MeV (see Table 1.1) and the average of the inclusive and exclusive determinations of $|V_{ub}| = (3.92 \pm 0.09 \pm 0.45) \times 10^{-3}$ [45] to evaluate the branching ratio.

Significant improvements in the precision of the measurement of $B_u \to \tau\nu$ will require a high-luminosity B factory. The two measurements by BABAR [36, 46] have used a large amount ($\sim 70\%$) of the available data taken at $\Upsilon(4S)$. The two measurements by BELLE [35,47] are with 414 fb^{-1} and 605 fb^{-1}, and so these could be significantly updated with the total integrated luminosity of 1000 fb^{-1}. A high-luminosity B factory with around 50 ab^{-1} could measure $B_u \to \tau\nu_\tau$ to a precision of around 6%. Moreover, with 50 ab^{-1} the decay $B_u \to \mu\nu$ (for which there is currently an upper limit) could be measured with about the same precision as $B_u \to \tau\nu$. Hence a precision of around 3% for $|V_{ub}| f_B$ could be achieved from each decay at a high-luminosity B factory. A combination of the measurements of $|V_{ub}| f_B$ from $B_u \to \tau\nu$ and $B_u \to \mu\nu$ would (presumably) further reduce the uncertainty.

1.4 Model independent constraints

We first study the impact of flavour observables in a model independent way and investigate the constraints on the Wilson coefficients assuming minimal flavour violation [48].

Contributions from physics beyond the SM to the observables in rare radiative, semileptonic and leptonic B decays can be described by the modification of Wilson coefficients:

$$\delta C_i(\mu_b) = C_i^{\mathrm{NP}}(\mu_b) - C_i^{\mathrm{SM}}(\mu_b) , \tag{1.43}$$

where the $C_i^{\mathrm{SM}}(\mu_b)$ are given in Table 1.2. For the numerical analysis we use the most recent

$C_7^{\rm eff}(\mu_b)$	$C_8^{\rm eff}(\mu_b)$	$C_9(\mu_b)$	$C_{10}(\mu_b)$	$C_0^l(\mu_b)$
-0.2974	-0.1614	4.2297	-4.2068	0

Table 1.2: SM Wilson coefficients at $\mu_b = m_b^{\rm pole}$ and $\mu_0 = 2M_W$ to NNLO accuracy in α_s.

Observable	Experiment (post-LHCb)	Experiment (pre-LHCb)	SM prediction
$\mathrm{BR}(B_s \to \mu^+\mu^-)$	$< 4.5 \times 10^{-9}$ [49]	$< 5.8 \times 10^{-8}$ [50]	$(3.53 \pm 0.38) \times 10^{-9}$
$\langle dBR/dq^2(B \to K^*\mu^+\mu^-)\rangle_{lq^2}$	$(0.42 \pm 0.04 \pm 0.04) \times 10^{-7}$ [51]	$(0.32 \pm 0.11 \pm 0.03) \times 10^{-7}$ [52]	$(0.47 \pm 0.27) \times 10^{-7}$
$\langle dBR/dq^2(B \to K^*\mu^+\mu^-)\rangle_{hq^2}$	$(0.59 \pm 0.07 \pm 0.04) \times 10^{-7}$ [51]	$(0.83 \pm 0.20 \pm 0.07) \times 10^{-7}$ [52]	$(0.71 \pm 0.18) \times 10^{-7}$
$\langle A_{FB}(B \to K^*\mu^+\mu^-)\rangle_{lq^2}$	$-0.18 \pm 0.06 \pm 0.02$ [51]	$0.43 \pm 0.36 \pm 0.06$ [52]	-0.06 ± 0.05
$\langle A_{FB}(B \to K^*\mu^+\mu^-)\rangle_{hq^2}$	$0.49 \pm 0.06 \pm 0.05$ [51]	$0.42 \pm 0.16 \pm 0.09$ [52]	0.44 ± 0.10
$q_0^2(A_{FB}(B \to K^*\mu^+\mu^-))$	$4.9^{+1.1}_{-1.3}$ GeV^2 [51]	–	4.26 ± 0.34 GeV^2
$\langle F_L(B \to K^*\mu^+\mu^-)\rangle_{lq^2}$	$0.66 \pm 0.06 \pm 0.04$ [51]	$0.50 \pm 0.30 \pm 0.03$ [52]	0.72 ± 0.13
$\mathrm{BR}(B \to X_s\gamma)$	$(3.55 \pm 0.24 \pm 0.09) \times 10^{-4}$ [53]	$(3.55 \pm 0.24 \pm 0.09) \times 10^{-4}$ [53]	$(3.08 \pm 0.24) \times 10^{-4}$
$\Delta_0(B \to K^*\gamma)$	$(5.2 \pm 2.6) \times 10^{-2}$ [53]	$(5.2 \pm 2.6 \pm 0.09) \times 10^{-2}$ [53]	$(8.0 \pm 3.9) \times 10^{-2}$
$\mathrm{BR}(B \to X_d\gamma)$	$(1.41 \pm 0.57) \times 10^{-5}$ [54,55]	$(1.41 \pm 0.57) \times 10^{-5}$ [54,55]	$(1.49 \pm 0.30) \times 10^{-5}$
$\mathrm{BR}(B \to X_s\mu^+\mu^-)_{q^2\in[1,6]\mathrm{GeV}^2}$	$(1.60 \pm 0.68) \times 10^{-6}$ [56,57]	$(1.60 \pm 0.68) \times 10^{-6}$ [56,57]	$(1.78 \pm 0.16) \times 10^{-6}$
$\mathrm{BR}(B \to X_s\mu^+\mu^-)_{q^2>14.4\mathrm{GeV}^2}$	$(4.18 \pm 1.35) \times 10^{-7}$ [56,57]	$(4.18 \pm 1.35) \times 10^{-7}$ [56,57]	$(2.19 \pm 0.44) \times 10^{-7}$

Table 1.3: Post- and pre-LHCb results for rare decays with the updated SM predictions [48]. lq^2 refers to $q^2 \in [1,6]$ GeV^2 and hq^2 to $q^2 \in [14.18, 16]$ GeV^2.

LHCb results for the exclusive decays $B_s \to \mu^+\mu^-$ and $B \to K^*\mu^+\mu^-$, and Belle, BaBar and CDF results for the other decays. The experimental values are provided in Table 1.3. For comparison, we also consider the pre-LHCb data that are given in the Table. The SM predictions entering the MFV-fit are based on the theoretical analyses given in Section 1.3. We have used the input parameters of Table 1.4 and the program `SuperIso` [2] in order to update the SM predictions. They are given in Table 1.3.

To obtain constraints on the Wilson coefficients, we scan over δC_7, δC_8, δC_9, δC_{10} and δC_0^l. For each point, we then compute the flavour observables using `SuperIso` and compare with the experimental results by calculating χ^2 as:

$$\chi^2 = \sum_i \frac{(O_i^{\rm exp} - O_i^{\rm th})^2}{(\sigma_i^{\rm exp})^2 + (\sigma_i^{\rm th})^2} \,, \tag{1.44}$$

where $O_i^{\rm exp}$ and $O_i^{\rm th}$ are the central values of the experimental result and theoretical prediction of observable i respectively, and $\sigma_i^{\rm exp}$ and $\sigma_i^{\rm th}$ are the experimental and theoretical errors respectively. The global fits are obtained by minimisation of the χ^2.

Separate bounds

We first study the individual constraints from the observables described in Section 1.3. The main players in our analysis are the radiative decay $\bar{B} \to X_s\gamma$, the leptonic decay $B \to \mu^+\mu^-$, and the semileptonic decays $\bar{B} \to X_s/K^*\mu^+\mu^-$.

Fig. 1.1 shows that similar zones are probed by the inclusive decays $\bar{B} \to X_s\gamma$ and $\bar{B} \to X_d\gamma$. The bounds in the $(\delta C_7, \delta C_8)$ planes induced by the two inclusive decays are nicely consistent with each other as expected in the MFV framework which predicts a strong

$m_B = 5.27950$ GeV	[58]	$m_{B_s} = 5.3663$ GeV	[58]
$m_{K^*} = 0.89594$ GeV	[58]	$\lvert V_{tb}V_{ts}^*\rvert = 0.0403^{+0.0011}_{-0.0007}$	[58]
$m_b^{\overline{MS}}(m_b) = 4.19^{+0.18}_{-0.06}$ GeV	[58]	$m_c^{\overline{MS}}(m_c) = 1.29^{+0.05}_{-0.11}$ GeV	[58]
$m_t^{pole} = 172.9 \pm 0.6 \pm 0.9$ GeV	[58]	$m_\mu = 0.105658$ GeV	[58]
$\alpha_s(M_Z) = 0.1184 \pm 0.0007$	[58]	$\hat{\alpha}_{em}(M_Z) = 1/127.916$	[58]
$\alpha_s(\mu_b) = 0.2161$		$\hat{\alpha}_{em}(m_b) = 1/133$	
$\sin^2\hat{\theta}_W(M_Z) = 0.23116(13)$	[58]	$G_F/(\hbar c)^3 = 1.16637(1)$ GeV^{-2}	[58]
$f_B = 194 \pm 10$ MeV	Table 1.1	$\tau_B = 1.519 \pm 0.007$ ps	[58]
$f_{B_s} = 234 \pm 10$MeV	Table 1.1	$\tau_{B_s} = 1.472 \pm 0.026$ ps	[58]
$f_{K^*,\perp}(1\text{ GeV}) = 0.185 \pm 0.009$ GeV	[59]	$f_{K^*,\parallel} = 0.220 \pm 0.005$ GeV	[59]
$a_{1,\perp}(1\text{ GeV}) = 0.10 \pm 0.07$	[60]	$a_{1,\parallel}(1\text{ GeV}) = 0.10 \pm 0.07$	[60]
$a_{2,\perp}(1\text{ GeV}) = 0.13 \pm 0.08$	[60]	$a_{2,\parallel}(1\text{ GeV}) = 0.09 \pm 0.05$	[60]
$\lambda_{B,+}(1\text{ GeV}) = 0.46 \pm 0.11$ GeV	[61]		
$\mu_b = m_b^{pole}$		$\mu_0 = 2M_W$	
$\mu_f = \sqrt{0.5 \times \mu_b}$ GeV	[31]		

Table 1.4: Input parameters.

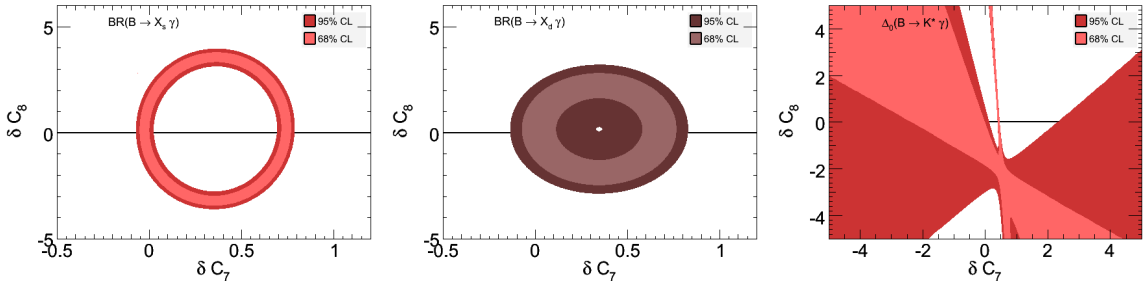

Figure 1.1: 68% and 95% C.L. bounds on δC_7 and δC_8 induced by the inclusive decays $\bar{B} \to X_s\gamma$ (left), $\bar{B} \to X_d\gamma$ (middle) and isospin asymmetry in $B \to K^*\gamma$ (right).

correlation between the two decays. Clearly, due to the smaller theoretical and experimental errors the $\bar{B} \to X_s\gamma$ bound is much stronger. In the previous MFV analysis [62] the approximation was used that the NP contributions to the electromagnetic and chromomagnetic operators appear in a fixed linear combination, namely $\delta C_7 + 0.3\delta C_8$. This additional assumption was necessary due to the limited number of independent experimental measurements. The correlations between δC_7 and δC_8, shown in Fig. 1.1, do not support this simplifying assumption.

The isospin asymmetry in the exclusive mode $B \to K^*\gamma$ brings complementary information to the inclusive branching ratios. The right plot in Fig. 1.1 shows that the isospin asymmetry seems to favour opposite signs for δC_7 and δC_8.

The leptonic decays $B_s \to \mu^+\mu^-$ and $B_d \to \mu^+\mu^-$ are sensitive to δC_{10} and the scalar contribution δC_0^l. The shapes in the corresponding correlation plots induced by the two leptonic decays are very similar, thus, highly consistent with each other as can be seen in Fig. 1.2. This feature strongly supports the MFV hypothesis which predicts a strong

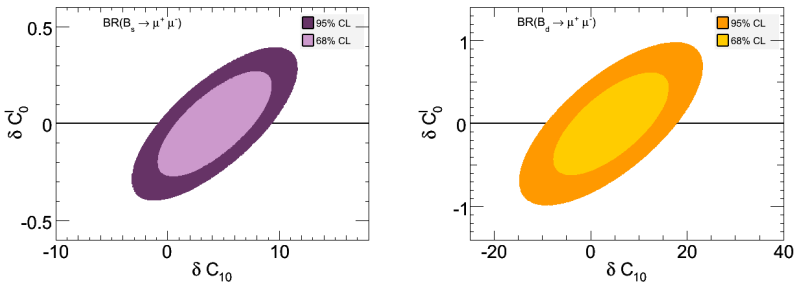

Figure 1.2: 68% and 95% C.L. bounds on δC_{10} and δC_0^l induced by the decays $B_s \to \mu^+\mu^-$ (left), $B_d \to \mu^+\mu^-$ (right).

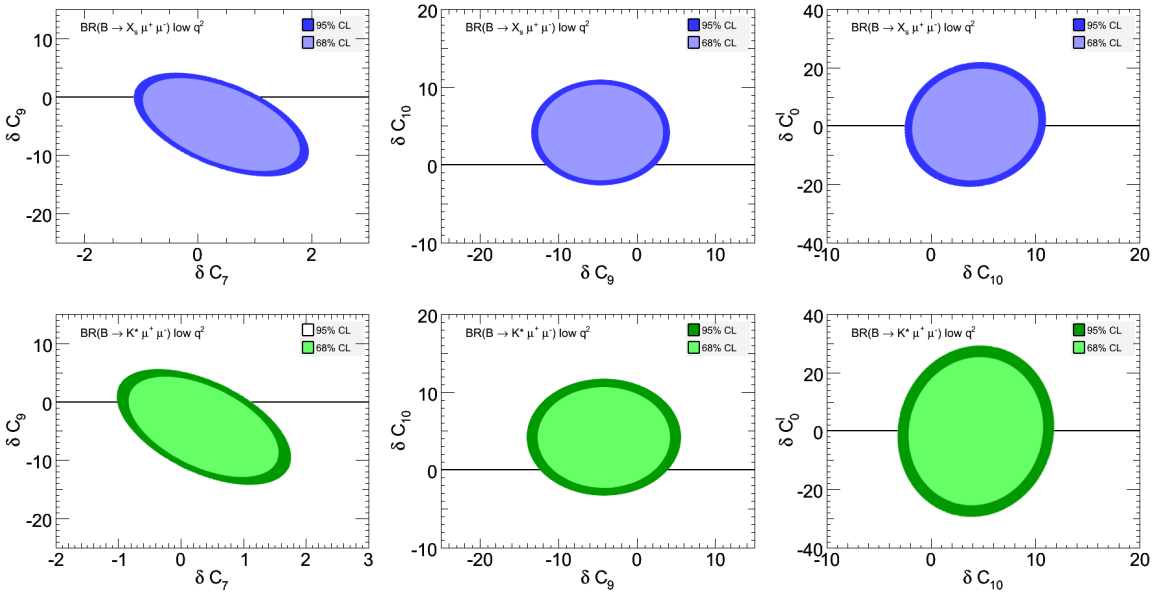

Figure 1.3: 68% and 95% C.L. bounds on various δC_i induced by the decays $B \to X_s\mu^+\mu^-$ (upper panel) and $B \to K^*\mu^+\mu^-$ (lower panel) at low-q^2.

correlation between these two decays as given in Eq. (1.20). Of course, the experimental limit for the decay $B_s \to \mu^+\mu^-$ is much tighter and therefore the present constraints are much stronger. We therefore take the decay $B_d \to \mu^+\mu^-$ out of the global MFV fit and will make a prediction for this decay within the MFV framework below.

We notice that the constraint on the scalar coefficient induced by the decay $B_s \to \mu^+\mu^-$ is very strong and a large scalar contribution is not allowed anymore.

The low-q^2 data of the inclusive decay $\bar{B} \to X_s\mu^+\mu^-$ and of the exclusive decay $B \to K^*\mu^+\mu^-$ have similar constraining power, as can be seen in Fig. 1.3. It is non-trivial that the correlation plots of the various δC_i look almost identical for the inclusive and the exclusive

mode. $\bar{B} \to X_s\mu^+\mu^-$ has small theoretical errors and large experimental errors, while the situation is reversed for $B \to K^*\mu^+\mu^-$. A statistical combination of both allows to enhance their effect. However, one realises the potential of the inclusive mode if one takes into account the fact that the recent BaBar and Belle measurements of the inclusive branching ratios [56, 57] only use less than a quarter of the available data sets of the B factories. The constraints on C_{10} are similar to those from $B_s \to \mu^+\mu^-$, but contrary to $B_s \to \mu^+\mu^-$, the constraints on the scalar contributions here is very weak.

Finally, we note that the allowed values of δC_9 and δC_{10} are much smaller in specific NP models than within a model-independent analysis, so for example the structure of the CMSSM already bounds their values significantly before any experimental data is used (see Fig. 1.6).

Fit results

We made two global MFV fits in order to make the significance of the latest LHCb data manifest, see Fig. 1.4. First we have used the experimental data before the start of the LHCb experiment (pre-LHCb, upper plots). Then we have included the latest LHCb measurements (post-LHCb, lower plots). These measurements are listed in Table 1.3.

Here C_8 is mostly constrained by $\bar{B} \to X_{s,d}\gamma$, while C_7 is constrained by many other observables as well. C_9 is highly constrained by $b \to s\mu^+\mu^-$ (inclusive and exclusive). C_{10} is in addition further constrained by $B_s \to \mu^+\mu^-$. C_0^l is dominantly constrained by $B_s \to \mu^+\mu^-$.

There are always two allowed regions at 95% C.L. in the correlation plots within the post-LHCb fit; one corresponds to SM-like MFV coefficients and one to coefficients with flipped sign. The allowed region with the SM is more favoured. The various δC_i-correlation plots show the flipped-sign for C_7 is only possible if C_9 and C_{10} receive large non-standard contributions which finally also change the sign of these coefficients.

We have also studied the impact of the LHCb measurements of the branching ratio, of the forward-backward asymmetry, and of the K^* polarisation within the exclusive decay $B \to K^*\ell^+\ell^-$ by taking these LHCb measurements out of the fit. The results in Fig. 1.5 show that these pieces of experimental information from the LHCb experiment are very important. They significantly reduce the allowed areas for δC_9 and δC_{10}.

Predictions within the MFV benchmark

With the help of the results of the global fit, which restricts the NP contributions δC_i, we can now derive several interesting predictions of observables which are not yet well measured. This analysis also enables to spot the observables which still allow for relatively large deviations from the SM even within the MFV benchmark scenario. Any measurement beyond the MFV bounds would indicate the existence of new flavour structures.

- For the branching ratio of the decay $\bar{B} \to X_s\tau\tau$ we get the 95% C.L. bounds

$$0.2 \times 10^{-7} \;<\; \mathrm{BR}(\bar{B} \to X_s\tau^+\tau^-)_{q^2>14.4\mathrm{GeV}^2} \;<\; 3.7 \times 10^{-7}\,. \tag{1.45}$$

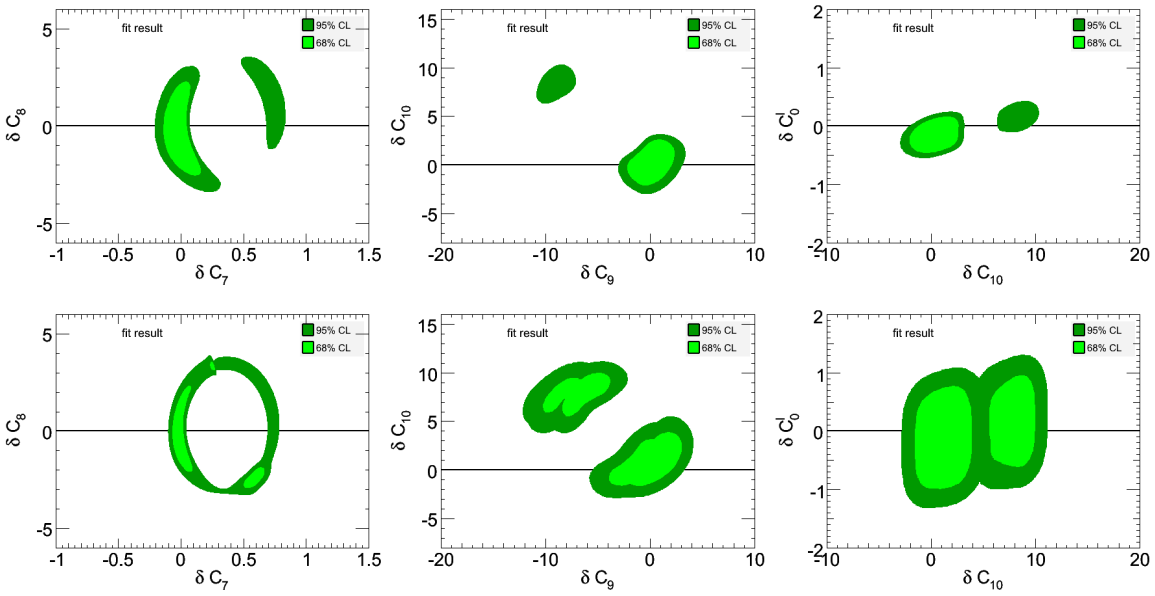

Figure 1.4: Global MFV fit to the various NP coefficients δC_i in the MFV effective theory *with* (upper panel) and *without* experimental data of LHCb (lower panel).

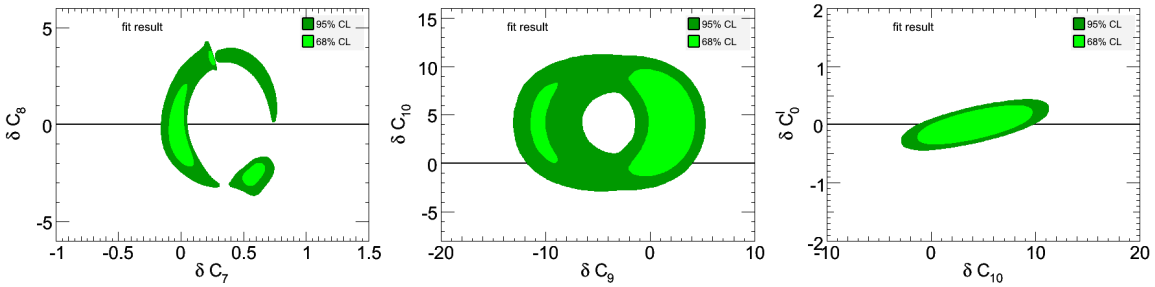

Figure 1.5: Global MFV fit with the latest data set *excluding* all LHCb measurements of $B \to K^* \mu^+ \mu^-$ observables.

This has to be compared with the SM prediction

$$\mathrm{BR}(\bar{B} \to X_s \tau^+ \tau^-)_{q^2 > 14.4\,\mathrm{GeV}^2} = (1.61 \pm 0.40) \times 10^{-7} \,. \tag{1.46}$$

So there are still large deviations from the SM prediction of this observable possible within the MFV scenario.

- For the zero-crossing of the forward-backward asymmetry in the inclusive decay $\bar{B} \to X_s \mu^+ \mu^-$, we get the lower bound at the 95% C.L.

$$A_{FB}(q_0^2) = 0 \,; \quad 1.94\,\mathrm{GeV}^2 < q_0^2 \,, \tag{1.47}$$

while the very precise SM prediction is $(q_0^2)^{\rm SM} = (3.40 \pm 0.25)\text{GeV}^2$. There is natural upper bound given by the cut due to the charm resonances. Due to the theoretical cleanliness of this observable, there are still large deviations from the SM prediction within the MFV benchmark possible. This is also true for the complete function $A_{FB}(q^2)$.

- We have taken the measurements of the decays $\bar{B} \to X_d\gamma$ and $B_d \to \mu^+\mu^-$ out of the global fit and find the following MFV predictions again at the 95% C.L.:

$$1.0\times10^{-5} < \text{BR}(\bar{B} \to X_d\gamma) < 4.0\times10^{-5}\,; \;\; \text{BR}(B_d \to \mu^+\mu^-) < 3.8\times10^{-10}\,. \quad (1.48)$$

The corresponding SM predictions are:

$$\text{BR}(\bar{B} \to X_d\gamma)^{\rm SM} = (1.49\pm0.30)\times10^{-5}\,; \;\; \text{BR}(B_d \to \mu^+\mu^-)^{\rm SM} = (1.11\pm0.27)\times10^{-10}\,, \quad (1.49)$$

and the present experimental data give:

$$\text{BR}(\bar{B} \to X_d\gamma)^{\rm Exp.} = (1.41 \pm 0.57) \times 10^{-5}\,; \;\; \text{BR}(B_d \to \mu^+\mu^-)^{\rm Exp.} < 10.0 \times 10^{-10}\,. \quad (1.50)$$

So the present $\bar{B} \to X_d\gamma$ measurement is already below the MFV bound and is nicely consistent with the correlation between the decays $\bar{B} \to X_s\gamma$ and $\bar{B} \to X_d\gamma$ predicted in the MFV scenario. In the case of the leptonic decay $B_d \to \mu^+\mu^-$, however, the MFV bound is stronger than the current experimental limit. And there are still sizeable deviations from the SM prediction within and beyond the MFV benchmark possible but an enhancement by orders of magnitudes due to large $\tan\beta$ effects is already ruled out by the latest measurements.

- For the large set of angular $B \to K^*\mu^+\mu^-$ observables discussed in Section 1.3 we also can easily derive their MFV predictions. In an exemplary mode, we give the 95% C.L. MFV predictions for the $A_T^{(i)}$, averaged over the low-q^2 region ($1\,\text{GeV}^2 < q^2 < 6\,\text{GeV}^2$),

$$-0.065 < \langle A_T^{(2)}\rangle < -0.022\,; \quad 0.34 < \langle A_T^{(3)}\rangle < 0.99\,; \quad 0.19 < \langle A_T^{(4)}\rangle < 1.27\,, \quad (1.51)$$

and for the $H_T^{(i)}$, averaged over the high-q^2 region ($14.18\,\text{GeV}^2 < q^2 < 16\,\text{GeV}^2$),

$$\langle H_T^{(1)}\rangle = 1\,; \quad -1.01 < \langle H_T^{(2)}\rangle < -0.44\,; \quad -1.01 < \langle H_T^{(3)}\rangle < -0.44\,. \quad (1.52)$$

Due to the experimental and theoretical uncertainties of the $A_T^{(i)}$ observables, the predicted MFV range cannot be really separated from the SM prediction; any significant deviation from the SM prediction indicates new flavour structures. But for the $H_T^{(i)}$ observables deviations from the SM are still possible within the MFV scenario.

1.5 Constraints in supersymmetry

We now turn our attention to the constraints in supersymmetry. As most of the rare decays can receive substantial contributions from Higgs bosons and supersymmetric particles, important constraints on SUSY parameters can be obtained.

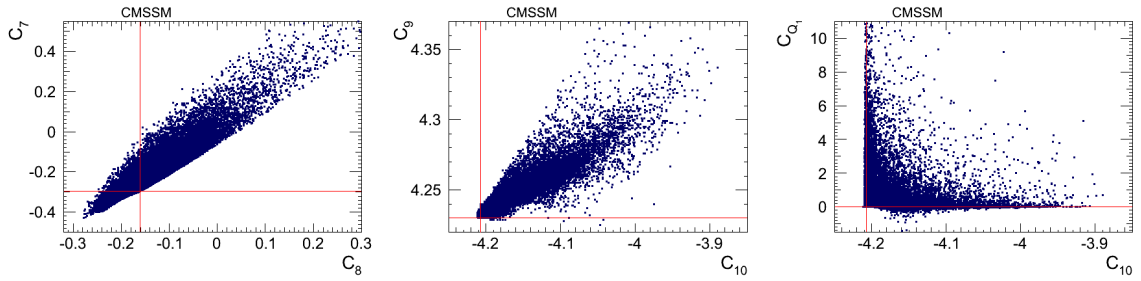

Figure 1.6: Variation of the Wilson coefficients in the CMSSM. The red lines correspond to the SM predictions.

1.5.1 Constrained MSSM

To illustrate the impact of the flavour observables on supersymmetry, we first consider constrained MSSM scenarios. The observables are calculated as described in section 1.3 using `SuperIso` [2].

We focus on two specific scenarios, both assuming SUSY breaking mediated by gravity and invoking unification boundary conditions at a very high scale $M_{\rm GUT}$ where the universal mass parameters are specified. The first model is the CMSSM, characterised by the set of parameters $\{m_0, m_{1/2}, A_0, \tan\beta, \text{sign}(\mu)\}$. Here m_0 is the universal mass of the scalars, $m_{1/2}$ the universal gaugino mass, A_0 the universal trilinear coupling, and $\tan\beta$ the ratio of the vacuum expectation values of the Higgs doublets. The second model we consider involves non-universal Higgs masses (NUHM). This model generalises the CMSSM, allowing for the GUT scale mass parameters of the Higgs doublets to have values different from m_0. The two additional parameters can be traded for two other parameters at a lower scale, conveniently the μ parameter and the mass M_A of the CP-odd Higgs boson implying that the charged Higgs boson mass can be treated essentially as a free parameter, contrary to the CMSSM. In both models, the flavour-changing effects we wish to study are effectively suppressed by the degeneracy of SUSY-breaking squark mass terms and trilinear couplings at the high scale, which suppresses the gluino (and neutralino) loop contributions. Only charged Higgs and chargino loops then remain, the latter dominating for large $\tan\beta > 30$. In this limit, the scalar penguin amplitudes get the strongest $\tan\beta$ enhancement. We thus expect the SUSY deviations from the SM to be maximised at large $\tan\beta$ for observables involving scalar penguin diagrams with a chargino-up-squark loop, for which the lightest stop mass should be a decisive parameter.

First we study the constraints in the CMSSM. For this purpose, we scanned over $m_0 \in [50, 3000]$ GeV, $m_{1/2} \in [50, 3000]$ GeV, $A_0 \in [-5000, 2000]$ GeV and $\tan\beta \in [1, 60]$. We generated about 500,000 points, and for each point we calculate the spectrum of SUSY particle masses and couplings using `SOFTSUSY` [63] and then compute the Wilson coefficient and flavour observables. The variation of the Wilson coefficients are shown in Fig. 1.6, ignoring existing constraints on SUSY parameters or Wilson coefficients. As can be seen, C_7 and C_8 can have both signs in SUSY and their correlation is visible in the figure: the

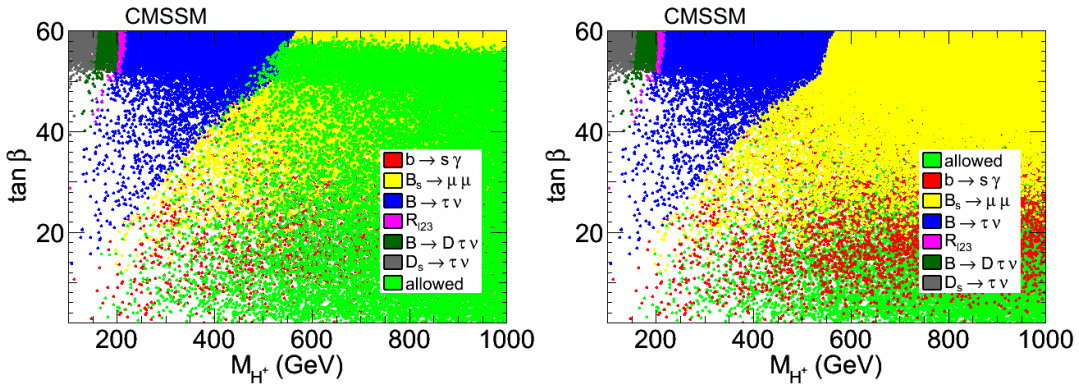

Figure 1.7: Excluded regions of the $(M_{H^+}, \tan\beta)$ parameter space in CMSSM. The constraints are applied in the order they appear in the legend, with the allowed points on top (left) and in the background (right).

same chargino-stop (or charged Higgs-top) loop gives the leading contribution, regardless of whether a photon (C_7) or gluon (C_8) is attached to it. As for C_9, it varies only by very little while C_{10} can have a larger spread. This feature can be understood once we notice that box diagrams are suppressed with respect to scalar- or Z-penguin diagrams, giving $\delta C_9/\delta C_{10} \sim (g_V/g_A)_\mu \sim 1 - 4\sin^2\theta_W$. On the other hand, scalar coefficients can receive very large contributions in SUSY, as already known.

The constraints are shown in Fig. 1.7 in the plane $(M_{H^\pm}, \tan\beta)$. The constraints are applied in the order indicated by the legend, and the first constraint by which a certain point is excluded determines its colour. Points which are not excluded by any constraint are termed allowed and displayed in the foreground in the left panel to indicate the parameter regions still open for $H^\pm$, and in the background in the right panel to see better the constraining power of the observables. Only points with $\mu > 0$ and a neutral LSP are shown. In the CMSSM, the mass scale for the Higgs bosons is not a free parameter, but it is fixed by the universality assumptions at the GUT scale through RGE running. Lower masses for the heavy MSSM Higgs bosons requires the $\tan\beta$ enhanced contribution from y_b to cancel the always large RGE effects from the top Yukawa coupling y_t. The result of this balancing is seen in the figure, where the distribution of points reveals a clear preference for large $M_{H^\pm}$, and where smaller values for M_{H^+} are only obtained in combination with high $\tan\beta \gtrsim 50$.

In the NUHM scenario, the parameters are scanned over in a similar way as in the CMSSM, and in addition $\mu \in [-2000, 2000]$ GeV and $M_A \in [50, 1100]$ GeV. The results are shown in Fig. 1.8. From the figure, we note that the allowed points fall in a distinct region, forming a triangular shape in the lower half plane. The region of allowed points shares a diffuse boundary with that excluded by $B_u \to \tau\nu_\tau$ transitions. This diffuseness is the result of ϵ_0 variations.

The decay $B_s \to \mu^+\mu^-$ also provides tight constraints, however with stronger depen-

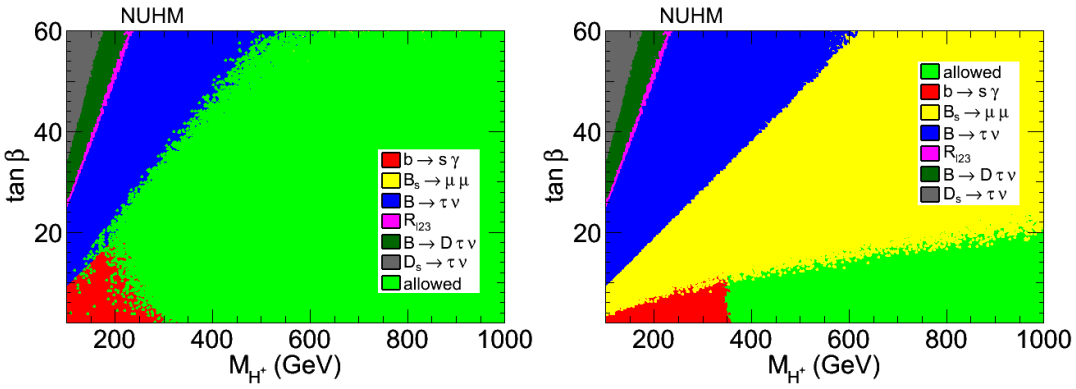

Figure 1.8: Excluded regions of the $(M_{H^+}, \tan\beta)$ parameter space in NUHM. The constraints are applied in the order they appear in the legend, with the allowed points on top (left) and in the background (right).

dence on other SUSY parameters as can be understood from the difference between the left and right-hand plots [64].

The constraints from $B \to K^*\mu^+\mu^-$ observables have been thoroughly studied in [12]. We consider here $\tan\beta$=50 but show also the results for $\tan\beta$=30, and investigate the SUSY spread as a function of the lightest stop mass. In Fig. 1.9, we display the CMSSM results at $\tan\beta$=50 and $\tan\beta$=30 with $A_0 = 0$ for the averaged differential branching ratio at low and high-q^2, the forward-backward asymmetry A_{FB}, the zero-crossing q_0^2 of A_{FB} and F_L. The solid red lines correspond to the LHCb central value, while the dashed and dotted lines represent the 1 and 2σ bounds respectively, including both theoretical and experimental errors (added in quadrature). At low q^2, the branching ratio excludes $M_{\tilde{t}_1}$ below $\sim$ 250 GeV for $\tan\beta$=50 and $\sim$ 150 GeV for $\tan\beta$=30. In the high q^2 region the branching ratio is doing slightly better, as the $M_{\tilde{t}_1}$ below $\sim$ 300 GeV and $\sim$ 200 GeV are excluded for $\tan\beta$=50 and $\tan\beta$=30 respectively. Contrary to the branching ratio, angular distributions, in which the theoretical uncertainties are reduced, can in principle provide more robust constraints on the SUSY parameter space. As can be seen, A_{FB} provides the most stringent constraints among these observables, and excludes $M_{\tilde{t}_1} \lesssim 800$ GeV and 600 GeV at $\tan\beta$=50 and $\tan\beta$=30 respectively. q_0^2 on the other hand excludes $M_{\tilde{t}_1} \lesssim$ 550 GeV (for $\tan\beta$=50) and 400 GeV (for $\tan\beta$=30) while F_L excludes $M_{\tilde{t}_1} \lesssim 200$ GeV (for $\tan\beta$=50) and 150 GeV (for $\tan\beta$=30). The impressive constraining power of A_{FB} is mainly due to the fact that the measured central value is smaller than the SM prediction and in addition the reported experimental errors are more than twice smaller than the previous results. Same observables at high q^2 have less impact on the SUSY parameters and therefore their results are not reproduced here.

A comparison between different flavour observables in the plane $(m_{1/2}, m_0)$ is given in Fig. 1.10, where we can also see the limits from $B \to X_s\gamma$, $B \to \tau\nu$, $R_{l23}(K \to \mu\nu_\mu)$, $B \to D\tau\nu_\tau$, $B \to X_s\mu^+\mu^-$ and $D_s \to \tau\nu_\tau$. In the left hand side, the combined CMS+LHCb

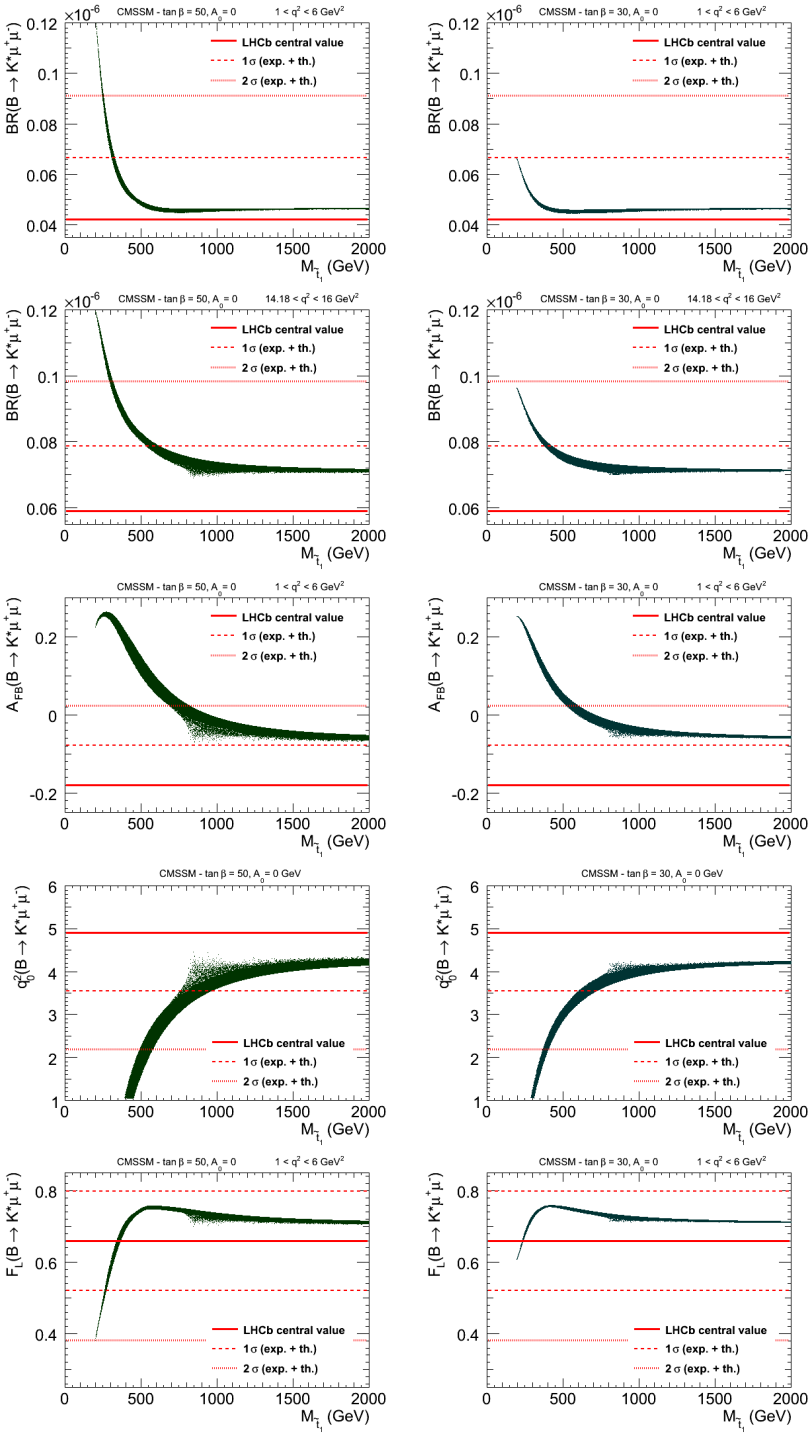

Figure 1.9: SUSY spread of the averaged BR($B \to K^*\mu^+\mu^-$) at low q^2 (first row) and at high q^2 (second row), $A_{FB}(B \to K^*\mu^+\mu^-)$ at low q^2 (third row), the $A_{FB}(B \to K^*\mu^+\mu^-)$ zero–crossing (fourth row) and $F_L(B \to K^*\mu^+\mu^-)$ at low q^2 (fifth row), as a function of the lightest stop mass, in the left for tan β=50 and in the right for tan β=30.

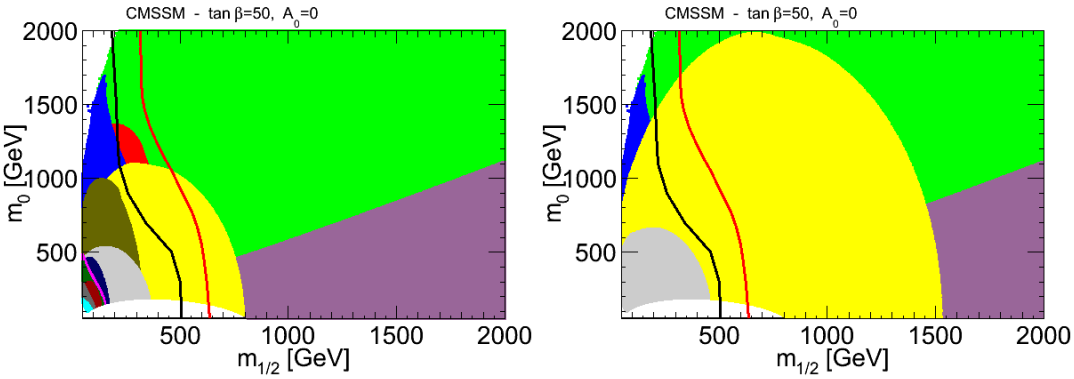

Figure 1.10: Constraints from flavour observables in CMSSM in the plane $(m_{1/2}, m_0)$ for $\tan\beta = 50$ and $A_0 = 0$, in the left with the 2011 results for $\mathrm{BR}(B_s \to \mu^+\mu^-)$, and in the right with the 2012 Moriond results. The black line corresponds to the CMS exclusion limit with 1.1 fb^{-1} of data [65] and the red line to the CMS exclusion limit with 4.4 fb^{-1} of data [66] at 7 TeV. The colour legend is given below.

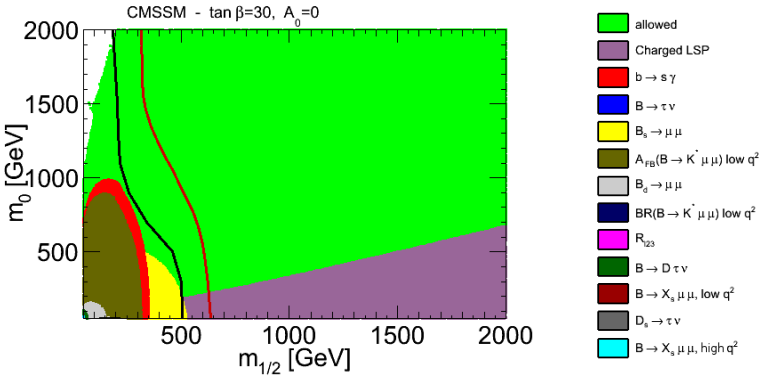

Figure 1.11: Constraints from flavour observables in CMSSM in the plane $(m_{1/2}, m_0)$ for $\tan\beta = 30$ and $A_0 = 0$.

2011 limit (1.1×10^{-8} at 95% C.L. [67]) is applied for $\mathrm{BR}(B_s \to \mu^+\mu^-)$, while this limit is updated to the 2012 Moriond LHCb result (4.5×10^{-9} at 95% C.L. [49]) in the right hand side. As can be seen, the recent LHCb limit strongly constrains the CMSSM with large $\tan\beta$. We also notice that, at large $\tan\beta$, the flavour constraints and in particular $B_s \to \mu^+\mu^-$, are superior to those from direct searches. By lowering the value of $\tan\beta$, $B_s \to \mu^+\mu^-$ significantly loses importance compared to direct searches as can be seen in Fig. 1.11. On the other hand, $B \to X_s\gamma$ and $B \to K^*\mu^+\mu^-$ related observables and in particular the forward-backward asymmetry lose sensitivity in a less drastic manner and they could play a complementary role in the intermediate $\tan\beta$ regime.

Parameter	Range
$\tan\beta$	[1, 60]
M_A	[50, 2000]
M_1	[-2500, 2500]
M_2	[-2500, 2500]
M_3	[50, 2500]
$A_d = A_s = A_b$	[-10000, 10000]
$A_u = A_c = A_t$	[-10000, 10000]
$A_e = A_\mu = A_\tau$	[-10000, 10000]
μ	[-3000, 3000]
$M_{\tilde{e}_L} = M_{\tilde{\mu}_L}$	[50, 2500]
$M_{\tilde{e}_R} = M_{\tilde{\mu}_R}$	[50, 2500]
$M_{\tilde{\tau}_L}$	[50, 2500]
$M_{\tilde{\tau}_R}$	[50, 2500]
$M_{\tilde{q}_{1L}} = M_{\tilde{q}_{2L}}$	[50, 2500]
$M_{\tilde{q}_{3L}}$	[50, 2500]
$M_{\tilde{u}_R} = M_{\tilde{c}_R}$	[50, 2500]
$M_{\tilde{t}_R}$	[50, 2500]
$M_{\tilde{d}_R} = M_{\tilde{s}_R}$	[50, 2500]
$M_{\tilde{b}_R}$	[50, 2500]

Table 1.5: SUSY parameter ranges (in GeV when applicable).

1.5.2 Phenomenological MSSM

Phenomenological MSSM (pMSSM) is the most general R-parity and CP conserving MSSM model with MFV [68], where no universality condition at the GUT scale is assumed. In this scenario, all the soft SUSY breaking parameters are assumed to be real in order to avoid new source of CP violation. The sfermion mass matrices and the trilinear coupling matrices are taken to be diagonal, to suppress FCNCs at tree level. In addition, the first and second sfermion generations are universal at low energy and the trilinear couplings are set to be equal for the three generations. With these assumptions, pMSSM admits 19 free input parameters at the weak scale.

To explore the pMSSM parameter space, we perform flat scans by randomly varying the 19 parameters within the intervals given in Table 1.5. We generated more than 100 million points. In this study, it is imposed that the lightest supersymmetric particle is the neutralino.

The range of branching fractions of $B \to X_s\gamma$ and $B_s \to \mu^+\mu^-$ in the pMSSM parameter space is displayed as a function of the gluino and the A^0 boson mass in Fig. 1.12.

We compared our accepted pMSSM points (more details and definition of "accepted pMSSM points" are given in chapter 3) to the 2011 combined CMS+LHCb limit for $B_s \to \mu^+\mu^-$ (1.1×10^{-8} at 95% C.L. [67]) as well as to the projected constraint in the case of observation of the decay with a SM-like rate of $\mathrm{BR}(B_s \to \mu^+\mu^-) = (3.4 \pm 0.7)\times 10^{-9}$, to which we have attached a 20% total relative uncertainty, by the end of the 2012 run. The results are presented in Fig. 1.13 in the M_A and $(M_A, \tan\beta)$ planes. The current limit affects the low M_A values up to 700 GeV, excluding large $\tan\beta$ values, below $M_A \sim$200 GeV.

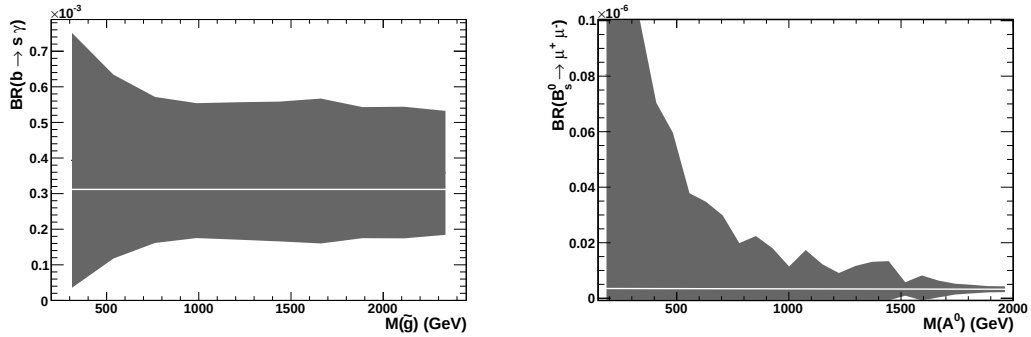

Figure 1.12: Branching fractions of $B \to X_s\gamma$ (left panel) and $B_s \to \mu^+\mu^-$ (right panel) of pMSSM points as a function of the gluino and A^0 boson masses, respectively. The white horizontal lines correspond to the SM values.

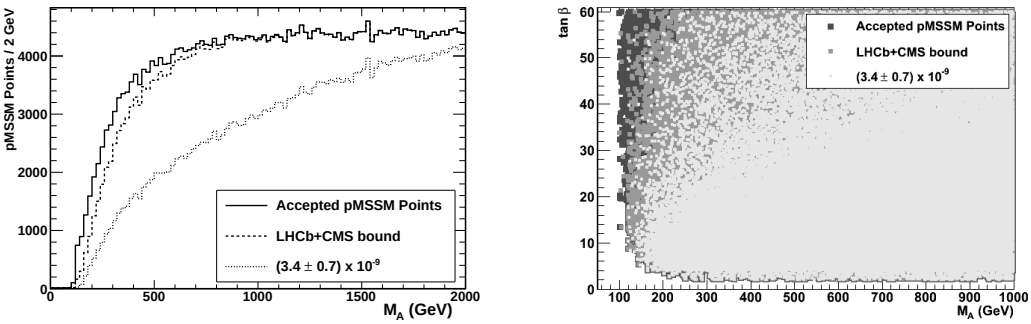

Figure 1.13: Distribution of pMSSM points after the $B_s \to \mu^+\mu^-$ constraint projected on the M_A (left panel) and $(M_A, \tan\beta)$ plane (right panel) for all accepted pMSSM points (medium grey), points not excluded by the 2011 combination of the LHCb and CMS analyses (dark grey) and the projection for the points compatible with a measurement of the SM expected branching fractions with a 20% total uncertainty (light grey).

The projected constraint has a stronger impact, with more than half of the spectrum being excluded for $M_A \lesssim 700$ GeV. However, the low $\tan\beta$ region at $\tan\beta \sim 5$ remains largely unaffected also by this constraint.

In the next chapters we further investigate the pMSSM scenario including in addition constraints from dark matter sector and LHC results from direct searches for SUSY particles and Higgs bosons.

Chapter 2

Dark matter

2.1 Dark matter relic density

The observations of the WMAP satellite [69], combined with other cosmological data, give evidence for the presence of a cosmological matter-like density representing about 27% of the total density of the Universe. The remaining 73% reveal the presence of the so-called dark energy. From the total matter density observed by WMAP [69] and the baryon density indicated by Big-Bang nucleosynthesis (BBN) [70], including theoretical uncertainties, the cold dark matter density range at 99.9% C.L. can be deduced:

$$0.068 < \Omega_{DM} h^2 < 0.155 \, , \tag{2.1}$$

where h is the reduced Hubble constant.

The lightest supersymmetric particle (LSP), provided it is stable and electrically neutral, constitutes the favourite candidate for non-baryonic dark matter. The stability requirement is fulfilled when R-parity is conserved, and MSSM scenarios provide us with a LSP satisfying the WMAP relic density constraints.

The great accuracy of the WMAP data can therefore be used to constrain the supersymmetric parameters, if the relic density is calculated precisely. The computation of the relic density has been realised within the standard model of cosmology [71], and implemented in automatic codes, such as `MicrOMEGAs` [72], `DarkSUSY` [73] and `SuperIso Relic` [74].

2.1.1 Standard calculation

The cosmological standard model is based on an approximately flat Friedmann-Lemaître Universe filled with radiation, baryonic matter and cold dark matter and incorporating a cosmological constant accelerating its expansion. Before recombination, the Universe expansion was dominated by a radiation density, and therefore the expansion rate H of the Universe is determined by the Friedmann equation

$$H^2 = \frac{8\pi G}{3} \rho_{rad} \, , \tag{2.2}$$

where

$$\rho_{rad}(T) = g_{\rm eff}(T)\frac{\pi^2}{30}T^4 \tag{2.3}$$

is the radiation density and $g_{\rm eff}$ is the effective number of degrees of freedom of radiation. The computation of the relic density is based on the solution of the Boltzmann evolution equation [75, 76]

$$dn/dt = -3Hn - \langle\sigma_{\rm eff}v\rangle(n^2 - n_{\rm eq}^2) \ , \tag{2.4}$$

where n is the number density of all supersymmetric particles, $n_{\rm eq}$ their equilibrium density, and $\langle\sigma_{\rm eff}v\rangle$ is the thermal average of the annihilation rate of the supersymmetric particles to the Standard Model particles. By solving this equation, the density number of supersymmetric particles in the present Universe and consequently the relic density can be determined.

The ratio of the number density to the radiation entropy density, $Y(T) = n(T)/s(T)$ can be defined, where

$$s(T) = h_{\rm eff}(T)\frac{2\pi^2}{45}T^3 \ . \tag{2.5}$$

$h_{\rm eff}$ is the effective number of entropic degrees of freedom of radiation. Combining Eqs. (2.2) and (2.4) and defining $x = m_{\rm LSP}/T$, the ratio of the LSP mass over temperature, yield

$$\frac{dY}{dx} = -\sqrt{\frac{\pi}{45G}}\frac{g_*^{1/2}m_{\rm LSP}}{x^2}\langle\sigma_{\rm eff}v\rangle(Y^2 - Y_{\rm eq}^2) \ , \tag{2.6}$$

with

$$g_*^{1/2} = \frac{h_{\rm eff}}{\sqrt{g_{\rm eff}}}\left(1 + \frac{T}{3h_{\rm eff}}\frac{dh_{\rm eff}}{dT}\right) \ , \tag{2.7}$$

and

$$Y_{eq} = \frac{45}{4\pi^4T^2h_{\rm eff}}\frac{1}{(1+\tilde{s}_D)}\sum_i g_i m_i^2 K_2\left(\frac{m_i}{T}\right) \ , \tag{2.8}$$

where i runs over all supersymmetric particles of mass m_i and with g_i degrees of freedom.

The freeze-out temperature T_f is the temperature at which the LSP leaves the initial thermal equilibrium when $Y(T_f) = (1+\delta)Y_{\rm eq}(T_f)$, with $\delta \simeq 1.5$. The relic density is obtained by integrating Eq. (2.6) from $x = 0$ to $m_{\rm LSP}/T_0$, where $T_0 = 2.726$ K is the temperature of the Universe today:

$$\Omega_{\rm LSP}h^2 = \frac{m_{\rm LSP}s(T_0)Y(T_0)h^2}{\rho_c^0} \approx 2.755\times10^8\frac{m_{\rm LSP}}{1\ {\rm GeV}}Y(T_0) \ , \tag{2.9}$$

where ρ_c^0 is the critical density of the Universe, such as

$$H_0^2 = \frac{8\pi G}{3}\rho_c^0 \ , \tag{2.10}$$

H_0 being the Hubble constant.

The computation of the thermally averaged annihilation cross section $\langle\sigma v\rangle$ is the most time consuming part of the relic density computation, as it requires the computation of the

many annihilation and co-annihilation amplitudes. One can define the annihilation rate of supersymmetric particles i and j into SM particles k and l:

$$W_{ij\to kl} = \frac{p_{kl}}{16\pi^2 g_i g_j S_{kl} E_{\rm cm}} \sum_{\text{internal d.o.f.}} \int |\mathcal{M}(ij \to kl)|^2 \, d\Omega \,, \tag{2.11}$$

where $\mathcal{M}$ is the transition amplitude, $E_{\rm cm}$ is the center-of-mass energy, g_i is the number of degrees of freedom of the particle i, p_{kl} is the final center-of-mass momentum such as

$$p_{kl} = \frac{\left[E_{\rm cm}^2 - (m_k + m_l)^2\right]^{1/2} \left[E_{\rm cm}^2 - (m_k - m_l)^2\right]^{1/2}}{2E_{\rm cm}} \,, \tag{2.12}$$

S_{kl} is a symmetry factor equal to 2 for identical final particles and to 1 otherwise, and the integration is over the outgoing directions of one of the final particles. Moreover, an average over initial internal degrees of freedom is performed.

We also define an effective annihilation rate $W_{\rm eff}$ by

$$g_{LSP}^2 p_{\rm eff} W_{\rm eff} \equiv \sum_{ij} g_i g_j p_{ij} W_{ij} \tag{2.13}$$

with

$$p_{\rm eff}(E_{\rm cm}) = \frac{1}{2}\sqrt{E_{\rm cm}^2 - 4m_{LSP}^2} \,, \tag{2.14}$$

and

$$\frac{dW_{\rm eff}}{d\cos\theta} = \sum_{ijkl} \frac{p_{ij} p_{kl}}{8\pi g_{LSP}^2 p_{\rm eff} S_{kl} E_{\rm cm}} \sum_{\text{helicities}} \left| \sum_{\text{diagrams}} \mathcal{M}(ij \to kl) \right|^2 \,, \tag{2.15}$$

where θ is the angle between particles i and k.

2.1.2 Cosmological uncertainties

In the standard model of cosmology, the nature of the dark energy and the evolution of the Universe in the pre-BBN era remain unclear. The BBN era is the oldest period in the cosmological evolution when reliable constraints are derived, for temperatures of about 1 MeV. Successful BBN models predict that radiation was the dominant energy at that time, but no claim is made for much higher temperatures. In fact, in models like quintessence [77], k-essence [78] or dark fluid [79], dark energy could play a role before BBN, since its density could be much higher at such temperatures, as was especially underlined within the quintessence model in [80]. Also, some extra-dimension theories predict negative effective energies in the early Universe, which can modify the relic density [81].

Therefore, the standard model of cosmology could be more complex than what we think in the primordial Universe, and the pre-BBN era could have experienced a slower or faster expansion. Such a modified expansion, even though still compatible with the BBN or the WMAP results, changes the LSP freeze-out time and the amount of relic density.

The modification of the Friedmann equation can be parametrised as:

$$H^2 = \frac{8\pi G}{3}(\rho_{rad} + \rho_D) \,, \tag{2.16}$$

where ρ_{rad} is the radiation energy density, which is considered as dominant before BBN in the standard cosmological model. Following [82, 83], ρ_D can be introduced as an effective dark density which parametrises the expansion rate modification. The entropy evolution can also be modified:

$$\frac{ds}{dt} = -3Hs + \Sigma_D \,, \tag{2.17}$$

where s is the total entropy density. Σ_D parametrises here effective entropy fluctuations due to unknown properties of the early Universe. By separating the radiation entropy density from the total entropy density, *i.e.* setting $s \equiv s_{rad} + s_D$ where s_D is an effective entropy density, the following relation between s_D and Σ_D can be derived:

$$\Sigma_D = \sqrt{\frac{4\pi^3 G}{5}}\sqrt{1+\tilde{\rho}_D}T^2\left[\sqrt{g_{\rm eff}}s_D - \frac{1}{3}\frac{h_{\rm eff}}{g_*^{1/2}}T\frac{ds_D}{dT}\right] \,. \tag{2.18}$$

Following the standard relic density calculation method [75,76], we introduce $Y \equiv n/s$, and Eq. (2.6) becomes

$$\frac{dY}{dx} = -\frac{m_{LSP}}{x^2}\sqrt{\frac{\pi}{45G}}g_*^{1/2}\left(\frac{1+\tilde{s}_D}{\sqrt{1+\tilde{\rho}_D}}\right)\left[\langle\sigma v\rangle(Y^2 - Y_{eq}^2) + \frac{Y\Sigma_D - N_D}{\left(h_{\rm eff}(T)\frac{2\pi^2}{45}T^3\right)^2(1+\tilde{s}_D)^2}\right] \,, \tag{2.19}$$

where $x = m_{LSP}/T$, m_{LSP} being the mass of the relic particle, and

$$\tilde{s}_D = \frac{s_D}{h_{\rm eff}(T)\frac{2\pi^2}{45}T^3} \,, \qquad \tilde{\rho}_D \equiv \frac{\rho_D}{g_{\rm eff}\frac{\pi^2}{30}T^4} \,, \tag{2.20}$$

and

$$Y_{eq} = \frac{45}{4\pi^4 T^2 h_{\rm eff}}\frac{1}{(1+\tilde{s}_D)}\sum_i g_i m_i^2 K_2\left(\frac{m_i}{T}\right) \,, \tag{2.21}$$

where i runs over all supersymmetric particles of mass m_i and with g_i degrees of freedom.

For illustrative purposes, we adopt the parametrisations described in [82,83] for ρ_D and s_D:

$$\rho_D = \kappa_\rho \rho_{rad}(T_{BBN})\big(T/T_{BBN}\big)^{n_\rho} \tag{2.22}$$

and

$$s_D = \kappa_s s_{rad}(T_{BBN})\big(T/T_{BBN}\big)^{n_s} \,, \tag{2.23}$$

where T_{BBN} stands for the BBN temperature. κ_ρ and κ_s are respectively the ratio of effective dark energy/entropy density over radiation energy/entropy density, and n_ρ and n_s are parameters describing the behaviour of the densities.

We now study the effects of our parametrisations while scanning over the NUHM parameter space. About one million random SUSY points in the NUHM parameter plane (μ, M_A)

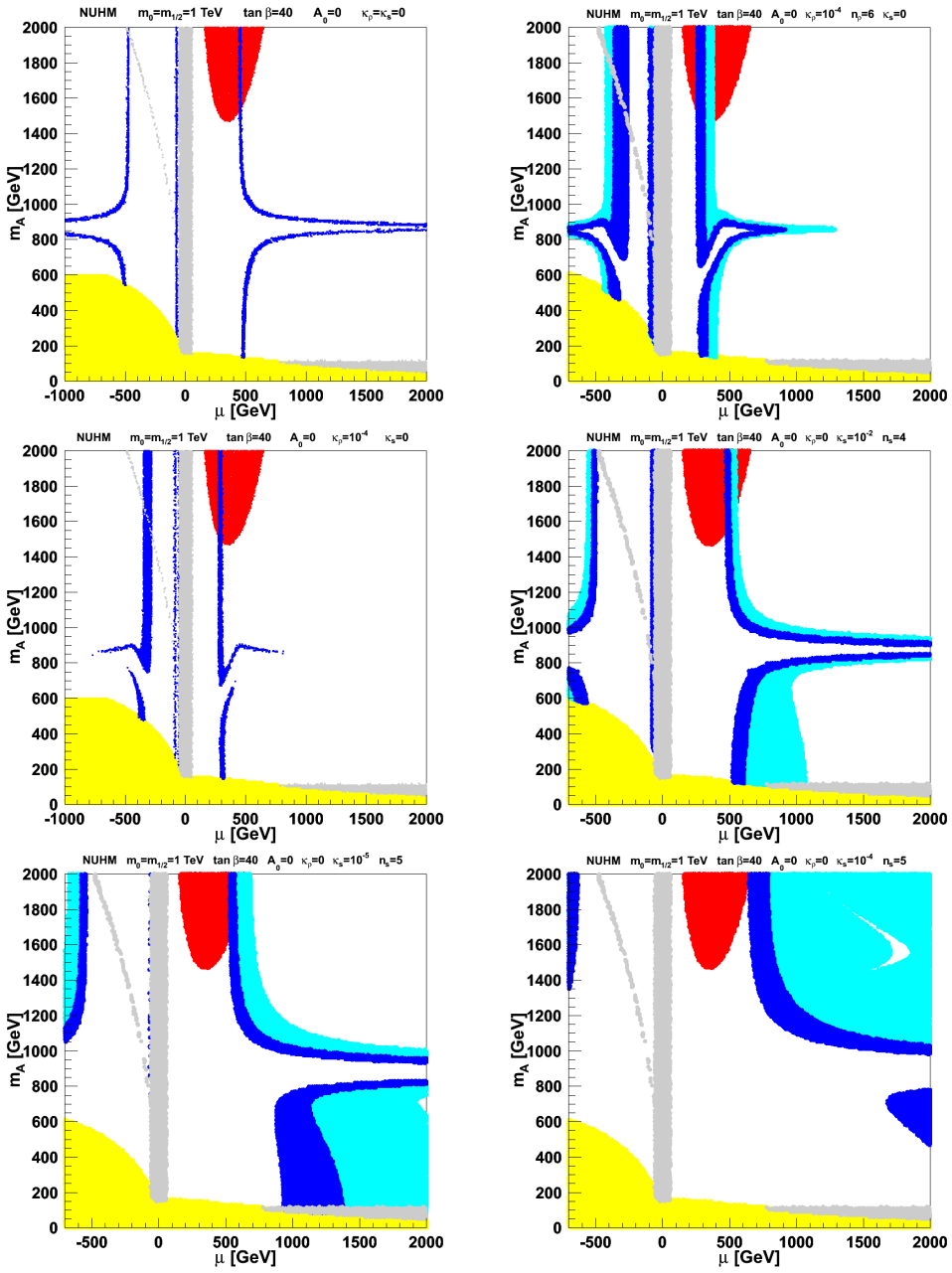

Figure 2.1: Constraints on the NUHM parameter plane (μ, M_A), from left to right and top to bottom, in the standard cosmological model, in presence of a tiny energy overdensity with $\kappa_\rho = 10^{-4}$ and $n_\rho = 6$, in presence of a tiny entropy overdensity with $\kappa_s = 10^{-3}$ and $n_s = 4$, with $\kappa_s = 10^{-2}$ and $n_s = 4$, with $\kappa_s = 10^{-5}$ and $n_s = 5$, and with $\kappa_s = 10^{-4}$ and $n_s = 5$. The red points are excluded by the isospin asymmetry of $B \to K^*\gamma$, the grey area is excluded by direct collider limits, the yellow zone involves tachyonic particles, and the dark and light blue strips are *favoured* by the WMAP constraints and by the interval $0.1 < \Omega_\chi h^2 < 0.3$ respectively.

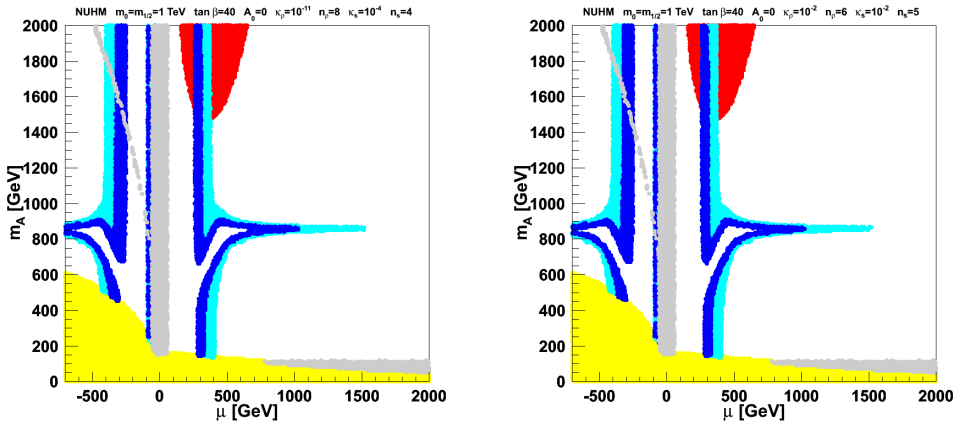

Figure 2.2: Constraints on the NUHM parameter plane (μ, M_A), in presence of a tiny energy overdensity with $\kappa_\rho = 10^{-11}$ and $n_\rho = 8$ associated to a tiny entropy overdensity with $\kappa_s = 10^{-4}$ and $n_s = 4$ on the left, and an energy overdensity with $\kappa_\rho = 10^{-2}$ and $n_\rho = 6$ associated to an entropy overdensity with $\kappa_s = 10^{-2}$ and $n_s = 5$ on the right. The colours are as in Fig. 2.1.

with $m_0 = m_{1/2} = 1$ TeV, $A_0 = 0$, $\tan\beta = 40$ are generated using `SOFTSUSY` [63], and for each point we compute flavour physics observables, direct limits and the relic density with `SuperIso Relic` [74].

In Fig. 2.1, the effects of the cosmological models on the relic density constraints are demonstrated. The first plot is given as a reference for the standard cosmological model, showing the tiny strips corresponding to the regions favoured by the relic density constraint. In the second plot, generated assuming a tiny additional energy density with $\kappa_\rho = 10^{-4}$ and $n_\rho = 6$, the relic density favoured strips are reduced, because the calculated relic densities are decreased as compared to the relic densities computed in the standard scenario. The next plots demonstrate the influence of an additional entropy density compatible with BBN constraints. The favoured strips are this time enlarged and moved towards the outside of the plot. This effect is due to a decrease in the relic density. Note that the different scenarios shown in these plots are equivalently valid from the cosmological observations. However, the SUSY favoured parameters can be drastically different depending on the cosmological assumptions employed.

In Fig. 2.2, we consider two cosmological scenarios in which energy as well as entropy densities are present. The energy and entropy densities have opposite effects and can compensate, and the similarity of the plots reveals the degeneracy between the two cosmological scenarios from the point of view of particle physics. However, using the BBN constraints, the scenario of the right plot can be ruled out.

An important consequence of this example is that if we discover that the particle physics scenario best in agreement with the LHC data (or future colliders) leads to a relic density in disagreement with the cosmological data constraints, important consequences on the cos-

$2.16 \times 10^{-4} < \mathrm{BR}(B \to X_s\gamma) < 4.93 \times 10^{-4}$
$\mathrm{BR}(B_s \to \mu^+\mu^-) < 5.0 \times 10^{-9}$
$0.56 < \mathrm{R}(B \to \tau\nu) < 2.70$
$4.7 \times 10^{-2} < \mathrm{BR}(D_s \to \tau\nu) < 6.1 \times 10^{-2}$
$2.9 \times 10^{-3} < \mathrm{BR}(B \to D^0\tau\nu) < 14.2 \times 10^{-3}$
$0.985 < \mathrm{R}_{\mu 23}(K \to \mu\nu) < 1.013$
$-2.4 \times 10^{-9} < \delta a_\mu < 4.5 \times 10^{-9}$
$10^{-4} < \Omega_\chi h^2 < 0.155$

Table 2.1: Constraints applied in our pMSSM analysis.

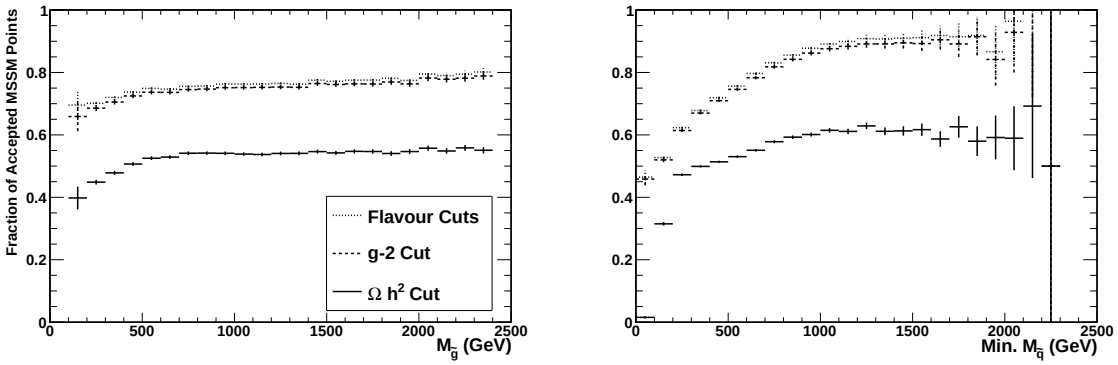

Figure 2.3: Fraction of valid MSSM points selected after the flavour (dotted line), $(g-2)_\mu$ (dashed line) and $\Omega_\chi h^2$ (solid line) subsequent constraints as a function of the masses of strongly-interacting SUSY particles: the gluino (left panel) and the lightest scalar quark (right panel).

mological scenario may be deduced: first, it would imply that the cosmological standard model does not describe satisfyingly the pre-BBN Universe. Second, combining all cosmological data, and in particular those from BBN, it would be possible to determine physical properties of the early Universe and constrain early Universe scenarios. As such, valuable constraints on cosmological models can be obtained from particle colliders.

2.1.3 Relic density constraints on the pMSSM

We return now to the pMSSM analysis presented in Section 1.5.2. The flavour observables, $(g-2)_\mu$ and relic density are computed with `Superiso Relic` [74]. The constraints used for this analysis are given in Table 2.1. For the relic density, we use a loose constraint to take into consideration the uncertainties from cosmology.

The effect of the relic density constraint on the masses of some SUSY particles is shown in Figs. 2.3 and 2.4, where the fraction of valid MSSM points fulfilling the subsequent cuts

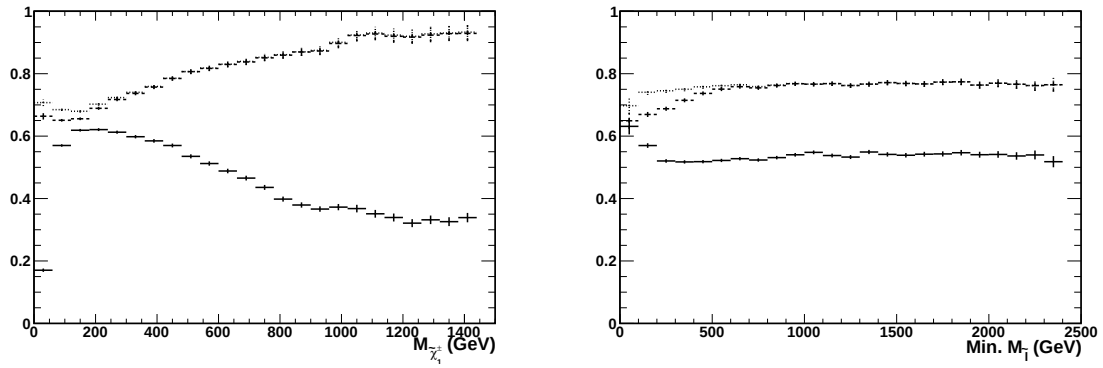

Figure 2.4: Fraction of valid MSSM points selected after the flavour (dotted line), $(g-2)_\mu$ (dashed line) and $\Omega_\chi h^2$ (solid line) subsequent constraints as a function of the masses of two weakly-interacting SUSY particles: the lightest chargino $\tilde{\chi}_1^\pm$ (left panel) and the scalar lepton (right panel).

on flavour, $(g-2)_\mu$ and $\Omega_\chi h^2$ observables is shown as functions of the masses of $\tilde{g}$, lightest $\tilde{q}$, $\tilde{\chi}_1^\pm$ and $\tilde{\ell}$ ($\ell = e,\ \mu$) [84]. We observe that the flavour cuts affect more masses below ∼500 GeV for the gluino and the lightest scalar quark due to the deviations arising from their contributions to heavy flavour loop-mediated decays. Very light, as well as heavy charginos are equally disfavoured by the relic dark matter constraint, which slightly favours light sleptons. However, with the exception of gluinos and lightest $\tilde{q}$ below 250 GeV and lightest charginos of more than 1 TeV, the acceptance of all these cuts appear quite flat with the mass of both strongly and weakly interacting SUSY particles.

2.2 Dark matter direct detection

Dark matter direct detection experiments have made great progress exploring $\tilde{\chi}p$ scattering cross sections in the range predicted by the MSSM [85–87]. In particular, the recent XENON 100 result [87], places a 90% C.L. upper bound on the spin-independent $\tilde{\chi}p$ cross section around 10^{-9} pb for $M_{\rm WIMP} \simeq 100$ GeV. In Fig. 2.5, the sensitivity of different dark matter experiments is presented.

In the following, `MicrOMEGAs` [72] is used to compute the direct detection scattering cross-sections. We apply the 2012 XENON-100 limit to the pMSSM scan described in Section 1.5.2. We show that the 2012 XENON limit excludes ∼28% of the accepted pMSSM points in our scan, as can be seen in Fig. 2.6.

The $\tilde{\chi}p$ spin-independent scattering process has contributions from scalar quark exchange and t-channel Higgs exchange [91]. The latter dominates over vast region of the parameter space with the Higgs coupling to the proton depending on its coupling to gluons, through a heavy quark loop and to non-valence quarks. The scattering cross section retains a strong sensitivity on the CP-odd boson mass as highlighted in Fig. 2.7 which shows the

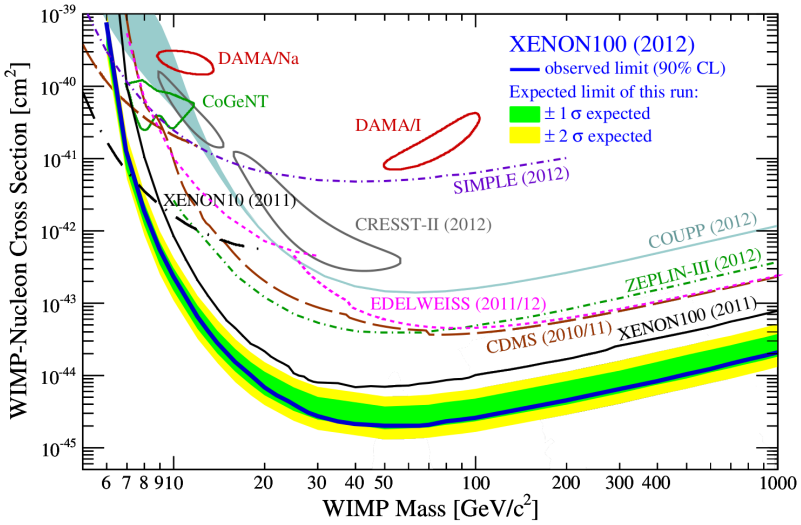

Figure 2.5: New result on spin-independent WIMP-nucleon scattering from XENON-100: the expected sensitivity of this run is shown by the green/yellow band ($1\sigma/2\sigma$) and the resulting exclusion limit (90% C.L.) in blue. For comparison, other experimental results are also shown [85, 88–90].

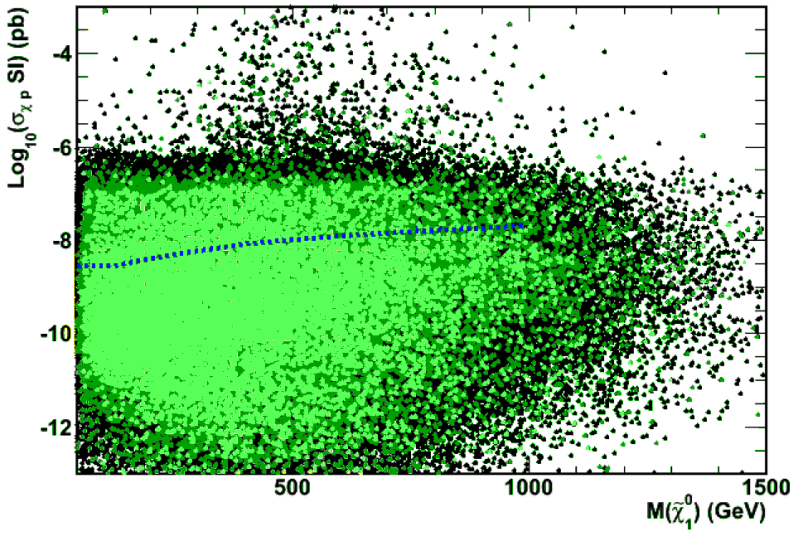

Figure 2.6: $\tilde{\chi}p$ scattering cross section as a function of the LSP mass. The black dots represent accepted pMSSM points, the light (dark) green dots the subset of points compatible with the Higgs search data at 68% (90%) C.L. The dotted line represents the 2012 XENON-100 90% C.L. exclusion contour.

pMSSM points retained after the 2011 and 2012 XENON 100 bounds [92]. The 2012 data exclude all solutions with $M_A \lesssim 200$ GeV, independent on the value of $\tan\beta$.

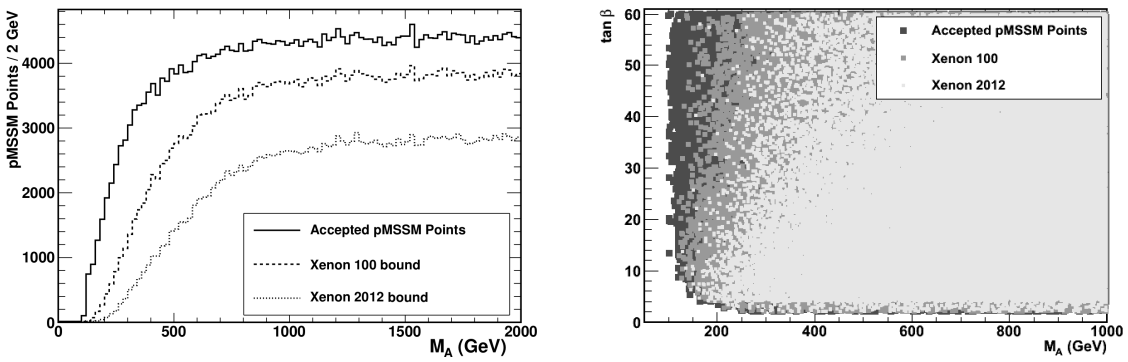

Figure 2.7: Distribution of pMSSM points after the dark matter direct detection constraint projected on the M_A (upper panel) and $(M_A, \tan\beta)$ plane (lower panel) for all accepted pMSSM points (medium grey), points not excluded by the 2011 (dark grey) and 2012 (light grey) XENON-100 data.

2.3 Light neutralino dark matter

The possibility that the LSP mass is much smaller than the electroweak scale is put forward by three dark matter direct detection experiments, which have reported a possible signal of WIMP interaction corresponding to very light particles, $5 < M_{\rm CDM} < 15$ GeV close to the edge of the XENON-100 and CDMS sensitivity (See Fig. 2.5). These are the DAMA experiment [88] at the Laboratory Nazionali del Gran Sasso, Italy, the CoGENT experiment [89] in the Soudan mine and the CRESST experiment [90], also at Gran Sasso. While there is still substantial debate on the interpretation of these data and the compatibility of the reported results with the exclusion bounds established by the other experiments an agreement could only be possible in the low neutralino mass region. Therefore it is interesting to explore the feasibility of light neutralino solutions in generic SUSY models and their compatibility with the results of the LEP and LHC searches.

In [93] we investigated the viability of SUSY scenarios with light neutralino using high statistics scans in the pMSSM. We identified several scenarios which give rise to very light neutralinos with large direct detection scattering cross sections. We applied constraints from dark matter relic density, direct detection, indirect detection, as well as flavour physics, electroweak precision tests, LEP and Tevatron limits, LHC limits on SUSY, Higgs and monojet searches.

For the relic density, we consider the tight interval:

$$0.068 < \Omega_\chi h^2 < 0.155 \,, \tag{2.24}$$

as well as the loose one:

$$10^{-4} < \Omega_\chi h^2 < 0.155 \,, \tag{2.25}$$

to take into consideration the cosmological uncertainties.

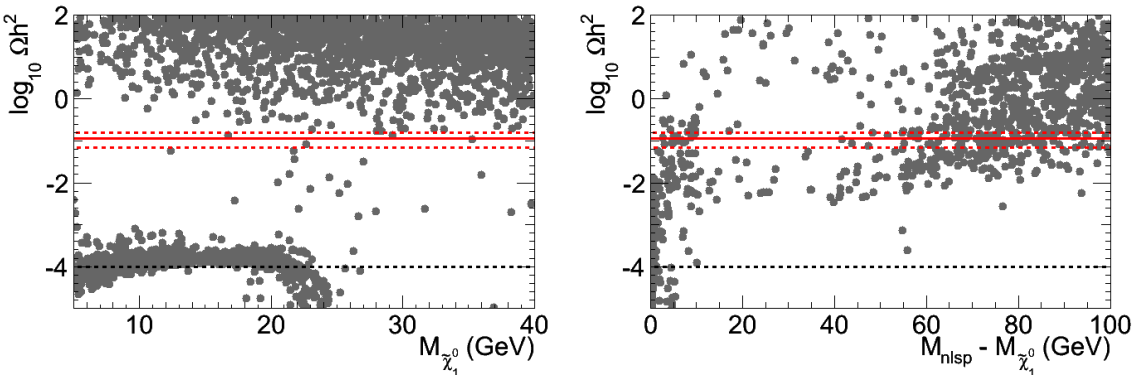

Figure 2.8: Relic density as functions of the $\tilde{\chi}_1^0$ mass (left panel) and NLSP mass (right panel). All the points in these plots pass the constraints from flavour physics, collider constraints and dark matter relic density. The continuous red line corresponds to the WMAP dark matter central values, and the dashed red lines to the upper and lower limits that we impose. The dashed black line corresponds to the lower limit that we use when relaxing the lower WMAP constraint.

We focus here on light neutralino masses in the range $5 < M_{\tilde{\chi}_1^0} < 40$ GeV and spin-independent scattering cross-sections $10^{-7} < \sigma_{\chi p}^{\rm SI} < 10^{-3}$ pb.

In general, for such a light LSP the relic density is larger than the upper relic density constraint, as shown in Fig. 2.8. However, if the mass difference between the next lightest supersymmetric particle (NLSP) and the LSP, ΔM, is small enough, the relic density is strongly decreased by the coannihilations of the two particles in the early Universe and $\Omega_\chi h^2$ can even fall below the lower limit applied for this study. pMSSM points compatible with the relic density constraint have values of the ΔM mass splitting of just a few GeV. The situation for the scattering cross-section is reversed: most of the selected pMSSM points have small scattering cross-sections, as shown in Fig. 2.9. In order to increase it up to the values highlighted by the direct search experiments claiming a light WIMP signal, $\sigma_{\chi p}^{\rm SI} \sim 10^{-6}$ pb, we have to require ΔM values below 1 GeV, which corresponds to a requirements opposite to that found for the relic density. Therefore, we can respect all the constraints imposed on the pMSSM points with light neutralinos only for few, very specific scenarios.

We identify three distinct classes of pMSSM solutions: i) the NLSP is a slepton slightly above the LEP limit, with a neutralino of about 30 GeV ii) the lightest chargino is degenerate with the $\tilde{\chi}_1^0$, often with a compressed gaugino spectrum and light Higgs bosons and iii) a scalar quark is degenerate with the $\tilde{\chi}_1^0$ while other scalar quarks and leptons are relatively heavy. Given the Higgs mass constraints, the possible light squarks for class iii) are those of the first and second generations or the lightest scalar bottom quark, $\tilde{b}_1$.

Scenario i) has only a limited interest because it corresponds to a region which is inside the exclusion contours by the CDMS and XENON experiments. Scenario ii) has first a spin independent χ-p scattering cross-section relatively small, of order $10^{-6} - 10^{-7}$ pb, and

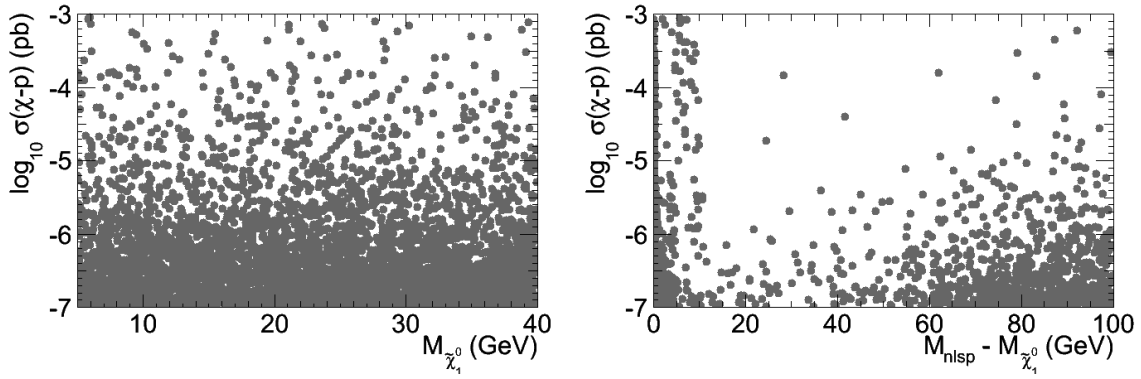

Figure 2.9: Spin independent χ-p scattering cross-section as functions of the $\tilde{\chi}_1^0$ mass (left panel) and NLSP mass (right panel). All the points in these plots pass the constraints from flavour physics, collider constraints and dark matter relic density.

second the production cross-section of $\chi_1^+\chi_1^-$ and $\chi_2^0\chi_1^0$ in this scenario at LEP-2 is large, and excluded by the combination of the data of the LEP-2 experiments [94] and the relic density constraint in this mass region.

Scenario iii) is the most interesting as it can provide us with a large spin independent χ-p scattering cross-section associated to a small neutralino mass (see Fig. 2.10). However, the couplings of the light squark to the Z and h bosons are in general large. In particular, the Z decay width into squarks excludes this scenario, unless the squark decouples from the Z. This happens for specific values of the squark mixing angle. Since the first and second generation squarks do not mix, they are excluded leaving only a degenerate scalar bottom $\tilde{b}_1$ as a viable scenario. The third generation left-handed squarks have a common mass in the pMSSM and a very light $\tilde{b}_1$ is only possible if the right-handed bottom squark is very light. In this case, the mixing angle θ_b is large, close to $\pi/2$ corresponding to a mainly right-handed $\tilde{b}_1$, and the squark naturally decouples from the Z. In addition, we observe that higher order SUSY corrections further decrease the $\tilde{b}_1$ mass, for appropriate values of the other parameters. This "sbottom miracle" makes possible to find pMSSM solutions which reconcile a light neutralino signal at direct detection experiments with the LEP-1 constraints. Considering now this light sbottom and the Higgs boson, we notice that the rate of the decay $h \to \tilde{b}_1\bar{\tilde{b}}_1$ can become important in such scenarios. However, it is possible to find points for which the branching fraction of $h \to \tilde{b}_1\bar{\tilde{b}}_1$ and the Z decay width to $\tilde{b}_1\bar{\tilde{b}}_1$ are simultaneously small. We checked the cosmological constraints by considering the indirect detection constraints by Fermi-LAT [95]. The selected points corresponding to the degenerate $\tilde{b}_1$ scenario have neutralino annihilation cross-sections times relative velocity to $b\bar{b}$ smaller than 5×10^{-27} cm^3/s, which is one order of magnitude below the current Fermi-LAT limits, which makes them compatible also with dark matter indirect detection limits. In summary, after considering the constraint from the LEP data, the only viable scenario with a neutralino mass below 20 GeV corresponds to the light sbottom NLSP case.

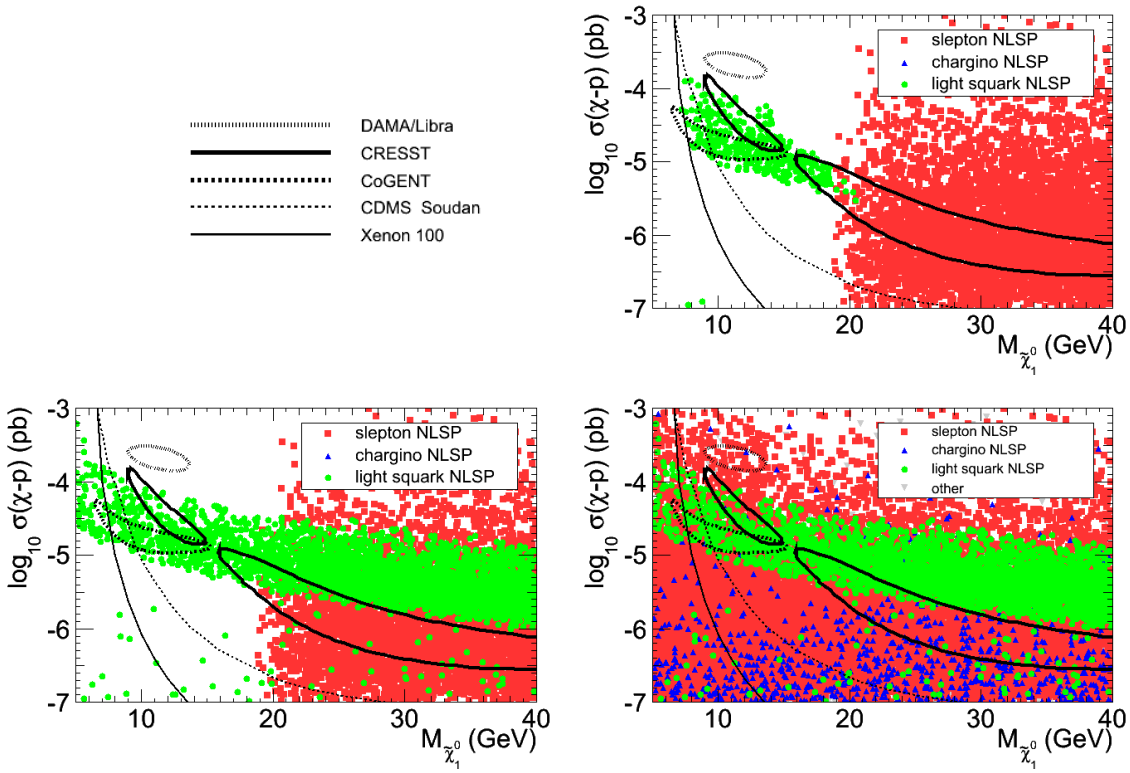

Figure 2.10: Spin independent χ-p scattering cross-section as a function of the $\tilde{\chi}_1^0$ mass. The points presented here pass all the constraints, including the tight relic density bounds (upper right), the loose relic density bounds (lower left) and no relic density constraint (lower right). The red squares correspond to a slepton NLSP with a mass slightly above the LEP limits (class i), the blue triangles to scenarios with a chargino NLSP (class ii), and the green points to cases where a scalar quark is degenerate with the light neutralino (class iii).

In Fig. 2.10, we present distribution of the points passing the tight relic density bound, the loose relic density bound, and without relic density constraint. A comparison of the three plots reveals that the lower bound of the relic density reduces the overall statistics, but also removes points corresponding to scenarios with a scalar quark degenerate with the light neutralino for neutralino masses above 20 GeV. This can be explained by the fact that points with a very small relic density have a small splitting. However, to get a relic density in the WMAP interval, the splitting should not be too small relatively to the neutralino mass. Also, the direct search bounds disfavour large splittings. Therefore, combining the relic density and direct search limits, only a small window remains where points can pass all the constraints.

In summary, we have investigated the compatibility of the DAMA, CoGENT and

CRESST signals with the generic minimal supersymmetric of the Standard Model, taking into account the constraints from the low energy, flavour, LEP and LHC data. Through high statistics flat scans of the pMSSM we have identified several scenarios which give rise to very light neutralinos with large scattering cross section. Once the LEP and LEP-2 limits are taken into account, the only viable scenario has the lightest scalar bottom quark, $\tilde{b}_1$ almost degenerate with the neutralino. This is compatible with the dark matter relic density from WMAP and indirect constraints from Fermi-LAT. A sizeable fraction of these points correspond to interaction cross section values close to the present constraints from CDMS and XENON. Relaxing the constraints from WMAP on the other hand leaves room also for other classes of scenarios such as the chargino or slepton NLSP cases to manifest themselves.

Chapter 3

Collider physics

In this chapter, we first discuss the implications of LHC searches on SUSY particle spectra using flat scans of the 19-parameter pMSSM phase space. We apply constraints from flavour physics and dark matter (as discussed in the previous chapters) and earlier LEP and Tevatron searches. Next we analyse the impact of the discovery of a new light scalar boson at the LHC in the context of several MSSM scenarios.

3.1 Implications of SUSY search results

3.1.1 Tools and constraints

The study of the LHC sensitivity in the pMSSM parameter space requires the use of several programs from the spectrum generation to the computation of flavour and other low energy and dark matter related observables, as well as the simulation and analysis of events in pp collisions [84, 92]. Throughout the analysis we use the SUSY Les Houches Accord (SLHA) format [96,97] to store the SUSY parameters, physical spectra and couplings, the HEPEVT format for simulated events and the `ROOT` format [98] for results of the scans, the physics objects after fast simulation and the analysis results.

SUSY spectra are generated with `SOFTSUSY` [63]. Results have been cross checked with `SUSpect` [99] and found to be compatible with the exception of few regions of the parameter space. The masses, widths and decay channels of Higgs bosons are obtained using `FeynHiggs` [100] and `HDECAY` [101]. The widths and branching fractions of the SUSY particles are computed using `SDECAY` [102]. Flavour observables, the muon anomalous magnetic moment and the dark matter relic density are calculated with `SuperIso Relic` [2,74]. Also, the neutralino-nucleon scattering cross-sections which are needed to evaluate dark matter direct detection constraint are computed with `micrOMEGAs` [72].

We use the `SuperIso` program as the central control program, which provides interfaces with the other above-mentioned programs through SLHA files. For each point giving a valid spectrum with $\tilde{\chi}_1^0$ LSP, we store the pMSSM parameters, SUSY particle spectra, branching fractions, and flavour and low energy observables in `ROOT` format. We then impose the constraints on these observables and on the masses of the supersymmetric particles imposing

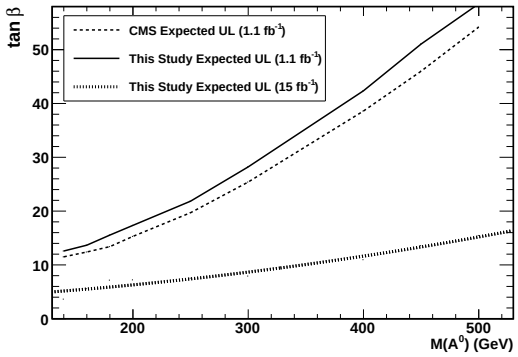

Figure 3.1: 95% C.L. upper limit exclusion contours in the $(M_A, \tan\beta)$ plane. The dashed line shows the expected exclusion from CMS with 1.1 fb^{-1} [107], the solid line the corresponding contour obtained with our simulations and the dotted line the same contour with 15 fb^{-1}.

the exclusion bounds from SUSY searches at LEP and the Tevatron and generate an SLHA file for each accepted point. These SLHA files, extended to include SUSY branching fractions, are used as input to `PYTHIA` [103] for event generation of inclusive SUSY production in pp interactions at 7 TeV and 8 TeV, using CTEQ5L parton distribution functions [104]. Cross sections are rescaled to their NLO values with the k-factors computed for each point by `Prospino` [105]. Generated events are passed through fast detector simulation using `Delphes` [106] tuned for the CMS detector. The output of the `Delphes` simulation is saved in `ROOT` format and followed by a custom implementation of the CMS SUSY analyses. Results are stored in a database which is subsequently read-in in `ROOT` and used to determine the observability of each of the pMSSM scan points.

We apply constraints from flavour physics, the muon anomalous magnetic moment and relic dark matter given in Table 2.1.

Furthermore, we consider the constraints from direct Higgs searches at LEP by preimposing $M_h > 111$ GeV (we discuss the case of a 126 GeV Higgs later). In order to study the scaling of heavy Higgs exclusion in $(M_A, \tan\beta)$ plane we estimate the sensitivity of the CMS analysis in the $\tau\tau$ channel [107]. We calculate the product $\sigma_\phi \mathrm{BR}_{\tau\tau}$ as a function of M_A and $\tan\beta$ in the NUHM model where we also vary m_0, $m_{1/2}$, A_0 and μ. We reconstruct the wedge for the 95% upper bound for 1.1 fb^{-1} on $\tan\beta$ as a function of M_A based on the expected sensitivity of the CMS analysis as given in [107]. We then rescale the 95% upper bound assuming an integrated luminosity of 15 fb^{-1}. The results are shown in Fig. 3.1. Finally we impose the constraints on the SUSY masses summarised in Table 3.1. Here we consider for simplicity a lower limit of 46 GeV for the lightest neutralino mass, even if this limit can be circumvented in specific cases, as discussed in chapter 2.

Particle	Limits	Conditions
$\tilde{\chi}_1^0$	46	
$\tilde{\chi}_2^0$	62.4	$\tan\beta < 40$
$\tilde{\chi}_3^0$	99.9	$\tan\beta < 40$
$\tilde{\chi}_4^0$	116	$\tan\beta < 40$
$\tilde{\chi}_1^\pm$	94	$\tan\beta < 40$, $m_{\tilde{\chi}_1^\pm} - m_{\tilde{\chi}_1^0} > 5$ GeV
$\tilde{e}_R$	73	
$\tilde{e}_L$	107	
$\tilde{\tau}_1$	81.9	$m_{\tilde{\tau}_1} - m_{\tilde{\chi}_1^0} > 15$ GeV
$\tilde{u}_R$	100	$m_{\tilde{u}_R} - m_{\tilde{\chi}_1^0} > 10$ GeV
$\tilde{u}_L$	100	$m_{\tilde{u}_L} - m_{\tilde{\chi}_1^0} > 10$ GeV
$\tilde{t}_1$	95.7	$m_{\tilde{t}_1} - m_{\tilde{\chi}_1^0} > 10$ GeV
$\tilde{d}_R$	100	$m_{\tilde{d}_R} - m_{\tilde{\chi}_1^0} > 10$ GeV
$\tilde{d}_L$	100	$m_{\tilde{d}_L} - m_{\tilde{\chi}_1^0} > 10$ GeV
$\tilde{b}_1$	248	$m_{\tilde{\chi}_1^0} < 70$ GeV, $m_{\tilde{b}_1} - m_{\tilde{\chi}_1^0} > 30$ GeV
	220	$m_{\tilde{\chi}_1^0} < 80$ GeV, $m_{\tilde{b}_1} - m_{\tilde{\chi}_1^0} > 30$ GeV
	210	$m_{\tilde{\chi}_1^0} < 100$ GeV, $m_{\tilde{b}_1} - m_{\tilde{\chi}_1^0} > 30$ GeV
	200	$m_{\tilde{\chi}_1^0} < 105$ GeV, $m_{\tilde{b}_1} - m_{\tilde{\chi}_1^0} > 30$ GeV
	100	$m_{\tilde{b}_1} - m_{\tilde{\chi}_1^0} > 5$ GeV
$\tilde{g}$	195	

Table 3.1: Constraints on the SUSY particle masses (in GeV) from searches at LEP and the Tevatron [58].

3.1.2 LHC analysis simulation

The sensitivity of the LHC SUSY searches with jets, leptons and missing energy for the pMSSM points selected from our scans has been assessed by reproducing on fast simulation the event selection criteria of three analyses of the CMS Collaboration. These analyses are the SUSY searches in all hadronic events with α_T [108], in same-sign isolated dilepton events with jets and missing energy [109] and in opposite-sign dilepton events with missing transverse energy [110]. Since these analyses are cut based, the observation or exclusion of a given model is obtained from the number of events observed in the signal region and the events selected by each analysis and signal regions are fully uncorrelated, they are well suited for a fast simulation and reconstruction study. While we have adopted the CMS analyses for this study, the ATLAS experiment has comparable sensitivity to SUSY.

Events generated with `PYTHIA` are subsequently reconstructed and classified following the procedure of the three CMS analyses from the physics objects obtained from the `Delphes` fast simulation. Jets are reconstructed using the anti-kt algorithm [111], implemented in the `FastJet` package [112]. The hadronic α_T analysis considers events fulfilling the selection requirements of ref. [108] binned according to their H_T value. The four bins:

- $575 < H_T < 675$ GeV,
- $675 < H_T < 775$ GeV,
- $775 < H_T < 875$ GeV,
- $H_T > 875$ GeV,

are used to search for the SUSY signal. The same-sign dilepton analysis considers high-p_T leptons in the four search regions defined by

- $H_T > 400$ GeV and $MET > 120$ GeV,
- $H_T > 400$ GeV and $MET > 50$ GeV,
- $H_T > 200$ GeV and $MET > 120$ GeV,
- $H_T > 80$ GeV and $MET > 100$ GeV.

The opposite-sign dilepton analysis considers the high MET and high H_T search regions defined by

- $MET > 275$ GeV and $H_T > 300$ GeV,
- $MET > 200$ GeV and $H_T > 600$ GeV,

respectively. The expected number of background events from SM processes in each search region is taken from the published CMS results, obtained with full simulation and reconstruction, validated on data, and rescaled to the assumed integrated luminosity. The 95% confidence level exclusion of each SUSY point in presence of background only is determined using the C.L.s method [113]. The number of events in each of the search regions of the CMS analyses described above is computed for the signal plus background and the background only hypotheses, where the signal represents the number of events in the search regions estimated for the SUSY point under test. The number of events in each of the search regions is assumed to be uncorrelated.

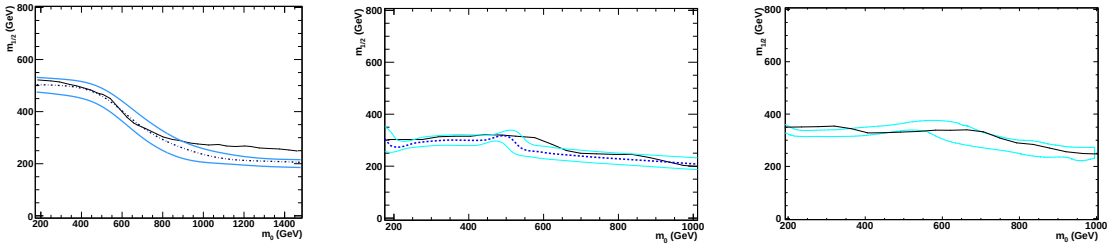

Figure 3.2: 95% C.L. exclusion contours in the (m_0, $m_{1/2}$) plane for CMSSM points with $\tan\beta = 10$, $A_0 = 0$ and sign(μ) = +1 for 1 fb^{-1} of data at 7 TeV. The contours obtained from our fast simulation analysis (black solid line) are compared to the bands of the expected exclusion limit from the CMS full simulation and reconstruction including uncertainties shown by the lighter coloured lines.

Simulation Validation

In order to ensure that the sensitivity to signal events in our fast simulation and reconstruction is representative of that from the analysis of the real CMS data, a validation of this procedure is performed comparing results of the fast simulation used in this analysis to those of signal events fully simulated and reconstructed with the CMS code. These events are chosen from the set of LM benchmark points, defined in the CMSSM model and used by the experiment for studies of the analysis sensitivities [114]. The fast simulation and reconstruction validation is performed in three stages. First, we compare the shape of event variables after event preselection. These are the number of reconstructed jets, the α_T variable used to discriminate against QCD jets and the sum of the jet transverse energies H_T for the hadronic analysis; the p_T of the two leading leptons, the dilepton invariant mass, the event missing transverse energy, MET, and H_T variable for the dilepton channels. The shape of the distributions in the CMS simulation and reconstruction and in the `Delphes` fast simulation are in good agreement. Then, we compare the number of signal events selected in the different signal regions for each LM point. In general, the agreement between CMS full simulation and reconstruction and the `Delphes` fast simulation is good, with differences in the observed signal event rates below 25%. Finally, we compare the exclusion contours obtained using our fast simulation in the (m_0, $m_{1/2}$) plane of the CMSSM model for the three analyses with the expected exclusion regions reported by CMS. Again, the 95% C.L. exclusion contours for the m_0 and $m_{1/2}$ CMSSM parameters obtained with our simulation agree within 20% to those of CMS as shown in Fig. 3.2.

3.1.3 Consequences on the pMSSM

Results are presented for 1 fb^{-1} and 15 fb^{-1} of integrated luminosity, corresponding to the statistics reported by CMS in 2011 and that formerly expected by the end of 2012, respectively. These are based on the analysis of the 835k pMSSM points fulfilling all the selection criteria discussed above and for which events have been successfully simulated, selected out

Selection	pMSSM points	Selection Efficiency	Cumulative Efficiency
Generated Points	24.57M	1	1
Valid Spectra	9.41M	0.383	0.383
$\tilde{\chi}_1^0$ LSP and Mass Limits	2.62M	0.278	0.107
Higgs Limits	1.81M	0.691	0.074
Flavour and $(g-2)_\mu$	1.34M	0.743	0.055
$\Omega_\chi h^2$	897k	0.668	0.037
Successful Simulation	835k	0.931	0.034

Table 3.2: Scan statistics. Points for which a 7 TeV pp inclusive SUSY event sample is successfully simulated and reconstructed are used in the subsequent analysis.

of 24.57M pMSSM generated points. The statistics and efficiency of the subsequent selection steps, from the generated points giving a valid `SOFTSUSY` spectrum through the mass, low energy data and $\Omega_\chi h^2$ constraints to those for which a sample of events for inclusive SUSY production at 7 TeV is successfully simulated with `PYTHIA` are summarised in Table 3.2. We discuss results for strongly interacting SUSY particles ($\tilde{g}$ and $\tilde{q}$), to which the present LHC searches are directly sensitive, and for their weakly interacting companions ($\tilde{\ell}$ and $\tilde{\chi}$), which are more indirectly probed at the LHC and are instead of major interest for the planning of a future high energy lepton collider. We present results in terms of the fraction of pMSSM points compatible with the constraints discussed in Section 3.1.1 (referred to as "accepted pMSSM points" in the following) which are excluded by the LHC searches as a function of the mass of the SUSY particle of interest. We study the scan coverage in terms of the characteristics of the SUSY spectra and particle properties. We observe that in 33.2% of accepted points, the gluino is lighter than the lightest of the squarks of the first two generations. 13.3% of the points have the gluino heavier than any of the squarks. Compressed spectra are particularly challenging for searches at the LHC. We observe that only 1.5% of our accepted points have $M_{\tilde{g}} - M_{\chi_1^0} < 50$ GeV, while 3.7% have $M_{\tilde{q}} - M_{\chi_1^0} < 50$ GeV, where $\tilde{q}$ is lightest squark of the first two generations. Turning to the particle properties, the Higgs boson mass ranges from 80 to 135 GeV. The lightest neutralino is bino-like in 6%, wino-like in 23%, and higgsino-like in 24% of the accepted points.

Further, we study the sensitivity of the three analyses used. We observe that of the points excluded with 1 (15) fb^{-1} of data, 96.2 (96.9)% are excluded by the fully hadronic analysis, 27.6 (30.0)% by the same sign lepton and 10.4 (16.1)% by the opposite sign lepton analysis. 3.8 (3.1)% of the points are excluded by leptonic analyses but not by the hadronic analysis.

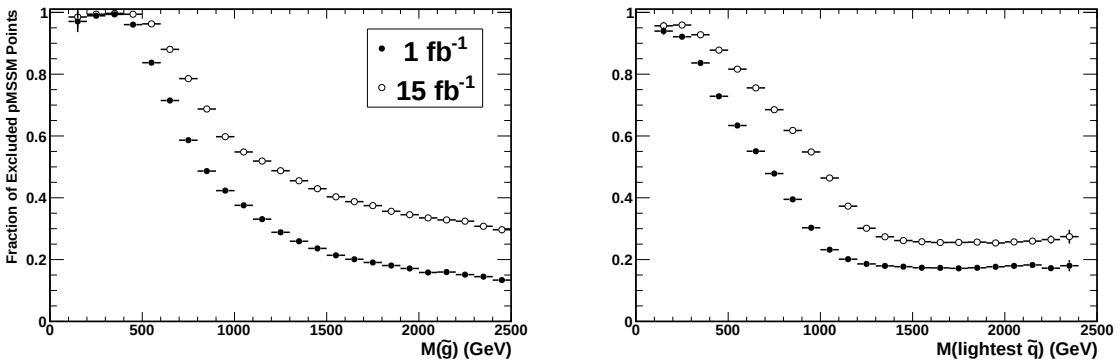

Figure 3.3: Fraction of valid MSSM points excluded at 95% C.L. by 1 fb^{-1} and 15 fb^{-1} of LHC data as a function of the masses of the gluino $\tilde{g}$ (left panel) and the lightest scalar quark of the first two generations (right panel).

Strongly Interacting Sparticle Spectra of Allowed pMSSM Points

We consider the masses of the gluino, $\tilde{g}$ and of the lightest scalar quark of the first two generations. Fig. 3.3 shows the fractions of accepted pMSSM points, which can be excluded by the results of the CMS analyses on 1 fb^{-1} and 15 fb^{-1} of data. We observe that in the case of the gluino the LHC data can exclude more than 85% of the pMSSM points up to a mass of ∼520 GeV and 700 GeV for 1 fb^{-1} and 15 fb^{-1}, respectively. The small fraction of points escaping exclusion below these mass limits have either small production cross section or small mass difference between the gluino and the LSP, resulting in compressed SUSY spectra yielding a lower transverse energy for the final state, as already pointed out in [115]. Above these masses, the sensitivity of the LHC data decreases rather sharply and disappears for $M_{\tilde{g}} \gtrsim 1.5$ TeV. For the case of the lightest scalar quark of the first two generations, the points which can be excluded by the LHC data account for more than 85% of the accepted pMSSM points up to mass values of 320 GeV and 510 GeV for 1 fb^{-1} and 15 fb^{-1} of data, respectively, while the effect of the LHC data disappears above 1.0 TeV and 1.3 TeV. These curves provide us with generic mass limits for strongly interacting SUSY particles which extend the results obtained on specific models, such as the CMSSM. As a comparison, in the CMSSM the limit on the gluino mass for 1 fb^{-1} of 7 TeV data is between 500 GeV and 1.1 TeV depending on m_0. In general, there are set of pMSSM parameters corresponding to spectra which are not detectable with the CMS analyses discussed above. Fig. 3.4 shows the fraction of valid MSSM points excluded at 95% C.L. by 1 fb^{-1} and 15 fb^{-1} of LHC data as a function of the inclusive SUSY cross section for 7 TeV pp collisions. Even at values of the SUSY cross section in excess of 5 pb which accounts for 19% of accepted points, approximately 20% of the pMSSM points are not observables because of the low transverse energy in the SUSY decay products. These points deserve a special attention in future LHC studies. pMSSM points with very compressed spectra having a mass difference between the gluino or the lightest of the scalar quarks of the first two generations and the LSP below

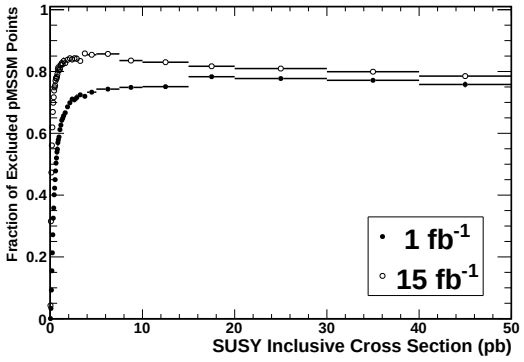

Figure 3.4: Fraction of valid MSSM points excluded at 95% C.L. by 1 fb^{-1} and 15 fb^{-1} of LHC data as a function of the inclusive SUSY cross section.

the jet p_T cut used in the analyses account for 5% of the total accepted points and 6% of those not excluded but having a SUSY inclusive cross section larger than 5 pb.

We assess the sensitivity of our results on the adopted range for the input SUSY parameters and the constraints by studying the change of the fractions of accepted pMSSM points excluded with 1 fb^{-1} of data and $M_{\tilde{g}} < 500$ and $M_{\tilde{q}} < 400$ GeV on a dedicated scan of 1M generated points. These fractions are 97.8% and 89.9% for our standard ranges and become 95.3% and 83.4% if we increase the SUSY parameter range by a factor 1.5. This shows that the results of these analyses in the range of sensitivity of the LHC data are only moderately sensitive to the chosen range of SUSY parameters. If we make looser cuts corresponding to 3.5 σ ranges the fraction of points passing this cut increases from 76% to 85%, and the fractions above become 95.6% and 83.3% for gluinos and squarks respectively. Finally, we apply tighter relic dark matter density cut corresponding to the 95% C.L. of the seven year WMAP result ($0.0924 < \Omega_\chi h^2 < 0.1316$). This reduces the fraction of accepted points from 66.8% to 0.7% and the fractions of excluded points in the selected gluino and squark mass range become 99.8% and 95.0%.

Weakly Interacting Sparticle Spectra of Allowed pMSSM Points

Likelihood analyses of constrained SUSY models have indicated that, as a result of the LHC searches, which have excluded the region of parameters favoured by data before the start of the LHC, the masses of SUSY particles over the allowed portion of the parameter space have shifted to larger values [116]. Instead, the impact of the LHC searches for gluinos and scalar quarks on weakly interacting supersymmetric particles in the general MSSM is only indirect. In the absence of the mass relations between particles of the strongly- and weakly-interacting sectors, typical of constrained models such as the CMSSM or the NUHM, the masses of gauginos and sleptons in the MSSM are *a priori* uncorrelated to those of the gluino and the squarks, since their mass parameters are free and independent.

Correlations are introduced either by the constraints applied from flavour physics and

relic dark matter density or by the signatures in the LHC analyses. A correlation between the $\tilde{\chi}_1^{\pm}$ and the $\tilde{q}$ masses is observed in this study and originates through the dark matter relic density constraint. Correlations between the masses of the $\tilde{q}$ and those of $\tilde{\chi}^{\pm}$, $\tilde{\chi}^0$, $\tilde{\ell}^{\pm}$ arise from searches in final states with leptons and missing energy. These topologies result from cascade decays involving gauginos and sleptons, such as $\tilde{q} \to q\tilde{\chi}$, $\tilde{\chi} \to \ell\tilde{\ell}$, $\tilde{\ell} \to \ell\tilde{\chi}_1^0$. The negative result in searches with these topologies suppresses pMSSM points with $\tilde{\chi}$ and $\tilde{\ell}$ with large enough mass splittings from the $\tilde{q}$ to give large transverse energies to the leptons searched in the analyses. As a result of these correlations, the negative result in the search for strongly interacting supersymmetric particles may allow us to make an inference on the masses of gauginos and sleptons in the allowed region of the parameter space. Results are again presented as the fractions of accepted pMSSM points, which can be excluded by the results of the CMS analyses on 1 fb^{-1} and 15 fb^{-1} of data as functions of SUSY particle masses in Fig. 3.5. As expected, the CMS analyses preferentially reduce the solutions with smaller masses for the sleptons and lighter gaugino states. However, $\sim$50% of the accepted pMSSM points with masses below 400 GeV are not excluded within our scans. We also observe that the domain of SUSY weakly-interacting particle masses above 500 GeV is virtually unaffected by the present LHC data. This result contrasts the indications obtained in highly constrained SUSY models. These observations are important both for motivating searches of direct gaugino production at the LHC and for interpreting the LHC data to guide the choice of the energy scale of a future lepton collider.

Similarly to what was done for strongly interacting sparticles, we assess the sensitivity of these results on the adopted range for the input SUSY parameters and the constraints. Here we study the change of the fractions of accepted pMSSM points, excluded with $M_{\tilde{\chi}_2^0} <$ 400 GeV and $M_{\tilde{l}} <$ 400 GeV on a dedicated scan. These fractions are 55.9% and 57.1% for our standard ranges with 1 fb^{-1} of data. They become 37.8% and 38.2% if we increase the SUSY parameter range by a factor 1.5, 38.1% and 37.9% if we loosen the constraints to 3.5 σ ranges, and 66.4% and 68.9% for a relic dark matter density cut corresponding to the 95% C.L. of the seven year WMAP result. The large change with the range of SUSY parameters is expected since the LHC data has little or no sensitivity on the mass of these particles and the fractions change with the broadening of the parameter space.

3.2 Implications of the Higgs search results

Results of the search for the Higgs bosons at the LHC with the 10 fb^{-1} data collected in 2011 at 7 TeV and 2012 at 8 TeV have been presented in July 2012 by the ATLAS [117] and CMS [118] collaborations, and a 5σ evidence for a new particle with a mass of $\approx$ 126 GeV has been revealed by each of the experiments. Complementary evidence was also provided by the updated combination of the Higgs searches performed by the CDF and D0 collaborations at the Tevatron [119]. As we have entered a new era of Higgs studies, these results have deep implications for the MSSM. The implications of a Higgs boson with a mass value around 126 GeV in the context of Supersymmetry have been already widely discussed [92,120–123] since the first evidence of a signal at the LHC was presented at the end of 2011. In particular, we have discussed the consequences of the value of M_h for the pMSSM with 19 free parameters,

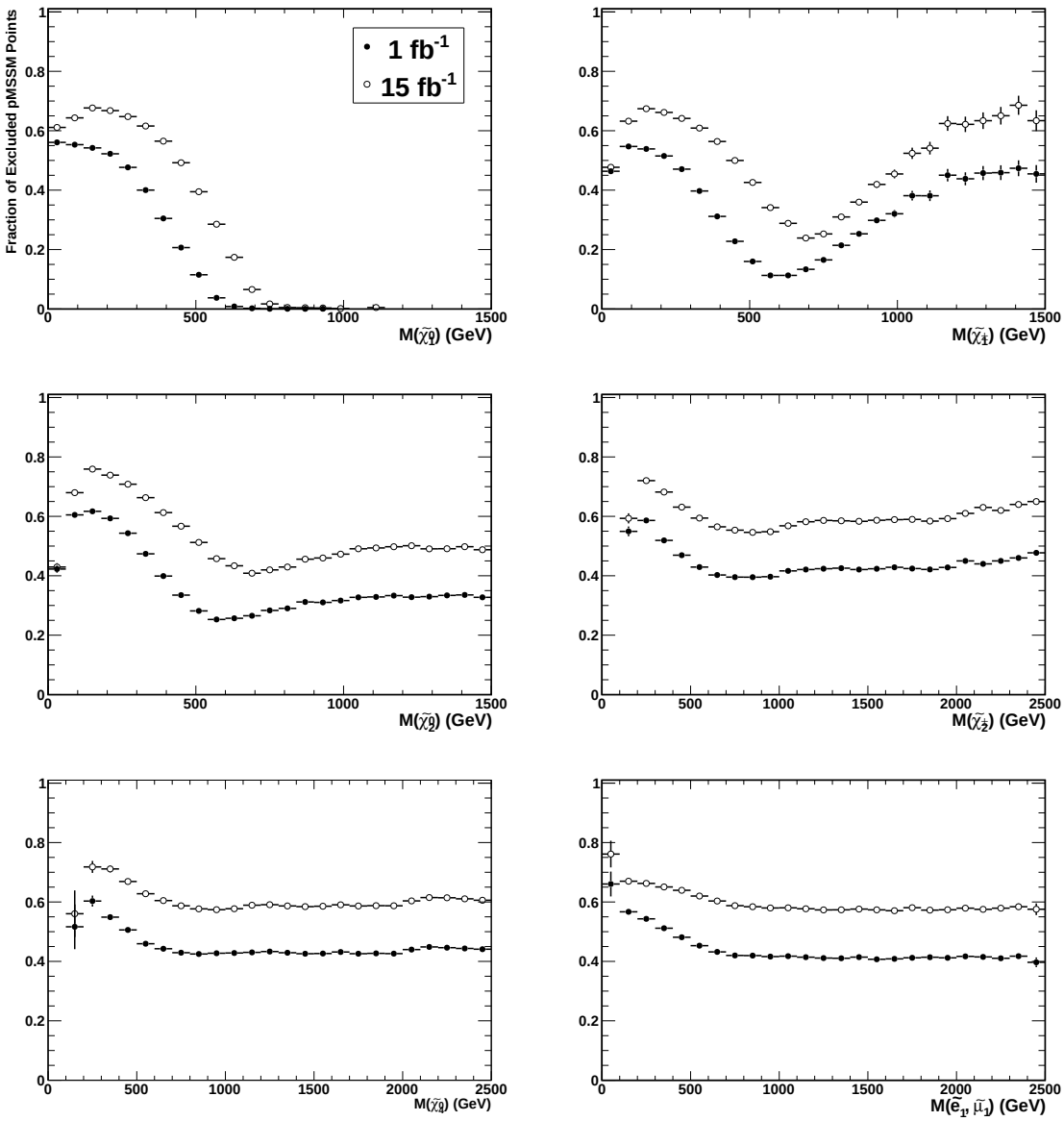

Figure 3.5: Fraction of valid MSSM points excluded at 95% C.L. by 1 fb^{-1} and 15 fb^{-1} of LHC data as a function of the masses of $\tilde{\chi}_1^0$ (upper left), $\tilde{\chi}_1^\pm$ (upper right), $\tilde{\chi}_2^0$ (mid left), $\tilde{\chi}_2^\pm$ (mid right), $\tilde{\chi}_4^0$ (lower left) and the lightest slepton of the first two generations $\tilde{\ell}^\pm$ (lower right).

for constrained MSSM scenarios such as the minimal gravity, gauge and anomaly mediated SUSY breaking models, and in scenarios in which the supersymmetric spectrum is extremely heavy [120]. We have shown that only when the SUSY breaking scale is very large or the

Parameter	Value	Experiment
M_H	125.9±2.1 GeV	ATLAS [117] + CMS [118]
$\mu_{\gamma\gamma}$	1.71±0.33	ATLAS [127] + CMS [128]
μ_{ZZ}	0.95±0.40	ATLAS [129] + CMS [130]
$\mu_{b\bar{b}}$	<1.64 (95% C.L.)	CMS [131]
$\mu_{\tau\tau}$	<1.06 (95% C.L.)	CMS [132]

Table 3.3: Combined values of the Higgs mass and signal strengths measured by ATLAS and CMS experiments.

mixing in the stop sector is significant the observed M_h value can be accommodated in these models. This disfavours many constrained scenarios such as the minimal anomaly and gauge mediated SUSY breaking models and some (even more constrained) versions of the minimal super-gravity model.

Searches for the MSSM Higgs bosons in the channels $h/H/A \to \tau^+\tau^-$ [124, 125] have already excluded a significant fraction of the $(M_A, \tan\beta)$ plane at low M_A values, $M_A \lesssim 200$ GeV and $\tan\beta \lesssim 10$, and larger values of $\tan\beta$ for $M_A \gtrsim 200$ GeV. These constraints on the pMSSM parameter space are already important. It is supplemented by the search of light charged Higgs bosons in top decays, $t \to bH^+ \to b\tau\nu$, performed by the ATLAS collaboration [126] which is effective at low M_A values, $M_A \lesssim 140$ GeV, corresponding to $M_{H^\pm} \lesssim 160$ GeV.

Assuming that the newly discovered particle at the LHC is the lightest Higgs boson, in our analysis we restrict the Higgs mass in the range allowed by the results reported by ATLAS and CMS:

$$123 \text{ GeV} \leq M_h \leq 129 \text{ GeV} \tag{3.1}$$

where the range is centred around the value corresponding to the average of the Higgs mass values reported by ATLAS and CMS, $M_h \simeq 126$ GeV, with the lower and upper limits accounting for the parametric uncertainties from the SM inputs, in particular the top quark mass, and the theoretical uncertainties in the determination of the h boson mass. It is also consistent with the experimental exclusion bounds.

We consider the two decay channels giving the Higgs boson evidence at the LHC, $\gamma\gamma$ and ZZ and include also the $b\bar{b}$ and $\tau\tau$ channels [121]. In the following, we use the notation R_{XX} to indicate the Higgs decay branching fraction to the final state XX, $\text{BR}(h \to XX)$, normalised to its SM value. We also compute the ratios of the product of production cross sections times branching ratios for the pMSSM points to the SM values, denoted by μ_{XX} for a given $h \to XX$ final state, $\mu_{XX} = \frac{\sigma(h)\times\text{BR}(h\to XX)}{\sigma(H_{\text{SM}})\times\text{BR}(H_{\text{SM}}\to XX)}$. These are compared to the experimental values. For the $\gamma\gamma$, and ZZ channels we take a weighted average of the results just reported by the experiments, as given in Table 3.3 with their estimated uncertainties.

While the results are compatible with the SM expectations within the present accuracy, they highlight a possible enhancement in the observed rates for the $\gamma\gamma$ channel, where ATLAS and CMS obtain $\mu_{\gamma\gamma} = 1.9\pm0.5$ and 1.56 ± 0.43, respectively. In the following, we do not take into account the theoretical uncertainties in the production cross section, which

are estimated significant for the main production channel, $gg \to h$ [133, 134].

Both the Higgs production cross section in gluon–gluon fusion and the Higgs decay rates can be affected by the contributions of SUSY particles. This makes a detailed study of the pMSSM parameter space in relation to the first results reported by the ATLAS and CMS collaborations especially interesting for its sensitivity to specific regions of the pMSSM parameter space.

3.2.1 Consequences of the Higgs mass measurement

Anatomy of Higgs-Boson Mass

In the decoupling limit of the MSSM, *i.e.*, $M_A^2 \gg M_Z^2$, the lightest CP-even Higgs boson acquires the squared tree-level mass

$$M_h^2 \approx M_Z^2 \cos^2(2\beta) \left(1 - \frac{M_Z^2}{M_A^2} \sin^2(2\beta)\right) . \tag{3.2}$$

Because $\cos^2(2\beta) \propto 1$ in the large $\tan\beta$ limit and given the minus sign of the decoupling correction proportional to M_Z^2/M_A^2, it follows that $M_h^2 \leq M_Z^2$. Yet, the scalar field h has SM-like couplings when the pseudoscalar Higgs boson mass M_A is large, so that this state should have been discovered at LEP, if it were not for the radiative corrections which push its mass upward from the tree-level upper bound of M_Z to $M_h > 114.4\,\text{GeV}$ [136].

In fact, these higher-order corrections can be very large, since the scalar sector of the MSSM involves strong couplings, such as those to the top quark and its scalar partners the stops. In the limits $M_A, \tan\beta \to \infty$, that are the relevant ones for the upper bound on M_h, these corrections are simple to evaluate. The dominant one-loop contribution to Eq. (3.2) arises from an incomplete cancellation of top-quark and top-squark loops, and can be approximated by [137–141]

$$(\Delta M_h^2)_{\tilde{t}} \approx \frac{3G_F}{\sqrt{2}\pi^2} m_t^4 \left[-L_{t\tilde{t}} + \frac{X_t^2}{M_S^2}\left(1 - \frac{X_t^2}{12M_S^2}\right)\right] , \tag{3.3}$$

where $L_{t\tilde{t}} = \ln\left(m_t^2/M_S^2\right)$ with $M_S^2 = m_{\tilde{t}_1} m_{\tilde{t}_2}$, while $X_t = A_t - \mu/\tan\beta$ denotes the stop-mixing parameter, which depends on the trilinear stop-Higgs boson coupling A_t and the higgsino mass parameter μ. We infer that for fixed stop spectrum scale M_S, the Higgs boson mass correction from top/stop loops is maximised for $|X_t| = \sqrt{6}\, M_S \approx 2.4\, M_S$, which is referred to as "maximal mixing" scenario. The manifest symmetry of Eq. (3.3) under the sign flip $X_t \to -X_t$ is broken by finite two-loop threshold corrections, which induce a term $4\alpha_s/\pi X_t/M_S$ [142, 143] that leads to slightly larger values of the Higgs boson mass for $X_t M_3 \approx A_t M_3 > 0$.

For large $\tan\beta$ there are further contributions to Eq. (3.2) that can be relevant [139–141]. These corrections arise from the sbottom and stau sector and take the form ($\tilde{f} = \tilde{b}, \tilde{\tau}$):

$$(\Delta M_h^2)_{\tilde{f}} \approx -\frac{N_c^{\tilde{f}}}{\sqrt{2}G_F} \frac{y_{\tilde{f}}^4}{96\pi^2} \frac{\mu^4}{m_{\tilde{f}}^4} , \tag{3.4}$$

where $N_c^{\tilde{b}} = 3$, $N_c^{\tilde{\tau}} = 1$, $m_{\tilde{f}}^2 = m_{\tilde{f}_1} m_{\tilde{f}_2}$, and we have ignored logarithmic terms for simplicity. In the limit of interest, the bottom (tau) Yukawa coupling receives important one-loop correction whose dominant contribution depends on sign (μM_3) (sign (μM_2)) [41–43,144]. The choice $\mu M_3 > 0$ ($\mu M_2 > 0$) tends to reduce the tree-level Yukawa coupling $y_b = \sqrt{2} m_b/(v \cos\beta)$ ($y_\tau = \sqrt{2} m_\tau/(v \cos\beta)$), and as a result decreases the strictly negative sbottom (stau) effect (3.4) on the Higgs boson mass.

The relations (3.2) to (3.4) allow to draw some general conclusions concerning the impact of the observation of a Higgs boson with $M_h \approx 126\,\text{GeV}$ on the MSSM parameter space. First, from the expression M_h^2, we deduce that large values of $\tan\beta$ and M_A are crucial to raise the tree-level Higgs boson mass as much as possible. In order to achieve a shift of $\Delta M_h^2 \approx (85.5\,\text{GeV})^2$, the top/stop effects in Eq. (3.3) have to be very large, which typically requires $M_S \gtrsim 1\,\text{TeV}$ (heavy stop spectrum) and/or $|A_t| \gtrsim 2\,\text{TeV}$ (large stop mixing). Since Eq. (3.4) scales with the fourth power of μ, the value of the higgsino mass parameter should not be too large. Finally, for sign $(A_t M_3)$, sign (μM_3), and sign (μM_2) equal to $+1$, subleading negative corrections to M_h^2 are minimised. We will see below that (some of) the mentioned MSSM parameters also play an important role in the production and the decay of the Higgs boson. This fact leads to interesting correlations.

SUSY constrained scenarios

In constrained MSSM scenarios (cMSSM), the various soft SUSY breaking parameters obey a number of universal boundary conditions at a high energy scale such as the GUT scale, thus reducing the number of basic input parameters to a handful. These inputs are evolved via the MSSM renormalisation group equations down to the low energy scale M_S where the conditions of proper electroweak symmetry breaking (EWSB) are imposed. The Higgs and superparticle spectrum is calculated, including the important radiative corrections. Three classes of such models have been widely discussed in the literature:

– The minimal supergravity (mSUGRA) model [145], in which SUSY breaking is assumed to occur in a hidden sector which communicates with the visible sector only via flavour-blind gravitational interactions, leading to universal soft breaking terms. Besides the scale M_{GUT} which is derived from the unification of the three gauge coupling constants, mSUGRA has only four free parameters plus the sign of μ: $\tan\beta$ defined at the EWSB scale and $m_0, m_{1/2}, A_0$ which are respectively, the common soft terms of all scalar masses, gaugino masses and trilinear scalar interactions, all defined at M_{GUT}.

– The gauge mediated SUSY breaking (GMSB) model [146] in which SUSY breaking is communicated to the visible sector via gauge interactions. The basic parameters of the minimal model are, besides $\tan\beta$ and sign(μ), the messenger field mass scale M_{mess}, the number of SU(5) representations of the messenger fields N_{mess} and the SUSY breaking scale in the visible sector Λ. To that, one adds the mass of the LSP gravitino which does not play any role here.

– The anomaly mediated SUSY breaking (AMSB) model [147] in which SUSY breaking is communicated to the visible sector via a super-Weyl anomaly. In the minimal AMSB version, there are three basic parameters in addition to sign(μ): $\tan\beta$, a universal parameter m_0 that contributes to the scalar masses at the GUT scale and the gravitino mass $m_{3/2}$.

In the case of the mSUGRA scenario, we will in fact study four special cases:

– The no-scale scenario with the requirement $m_0 \approx A_0 \approx 0$ [148]. This model leads to a viable spectrum compatible with all present experimental constraints and with light staus for moderate $m_{1/2}$ and sufficiently high $\tan\beta$ values; the mass of the gravitino (the lightest SUSY particle) is a free parameter and can be adjusted to provide the right amount of dark matter.

– A model with $m_0 \approx 0$ and $A_0 \approx -\frac{1}{4} m_{1/2}$ which, approximately, corresponds to the constrained next-to–MSSM (cNMSSM) [149] in which a singlet Higgs superfield is added to the two doublet superfields of the MSSM, whose components however mostly decouple from the rest of the spectrum. In this model, the requirement of a good singlino dark matter candidate imposes $\tan\beta \gg 1$ and the only relevant free parameter is thus $m_{1/2}$ [149].

– A model with $A_0 \approx -m_0$ which corresponds to a very constrained MSSM (VCMSSM) similar to the one discussed in Ref. [150] for input values of the B_0 parameter close to zero.

– The non–universal Higgs mass model (NUHM) in which the universal soft SUSY breaking scalar mass terms are different for the sfermions and for the two Higgs doublet fields [151]. We will work in the general case in which, besides the four mSUGRA basic continuous inputs, there are two additional parameters which can be taken to be M_A and μ.

The various parameters which enter the radiative corrections to the MSSM Higgs sector are not all independent in constrained scenarios as a consequence of the relations between SUSY breaking parameters that are set at the high energy scale and the requirement that electroweak symmetry breaking is triggered radiatively for each set of input parameters which leads to additional constraints. Hence, it is not possible to freely tune the relevant weak scale parameters to obtain the maximal value of M_h given previously. In order to obtain a reliable determination of $M_h^{\rm max}$ in a given constrained SUSY scenario, it is necessary to scan through the allowed range of values for all relevant SUSY parameters.

We adopt the ranges for the input parameters of the considered mSUGRA, GMSB and AMSB scenarios:

$$\begin{array}{rlll}
\text{mSUGRA:} & 50\ \text{GeV} \leq m_0 \leq 3\ \text{TeV}, & 50\ \text{GeV} \leq m_{1/2} \leq 3\ \text{TeV}, & |A_0| \leq 9\ \text{TeV}; \\
\text{GMSB:} & 10\ \text{TeV} \leq \Lambda \leq 1000\ \text{TeV}, & 1 \leq M_{\rm mess}/\Lambda \leq 10^{11}, & N_{\rm mess} = 1-5; \\
\text{AMSB:} & 1\ \text{TeV} \leq m_{3/2} \leq 100\ \text{TeV}, & 50\ \text{GeV} \leq m_0 \leq 3\ \text{TeV}. &
\end{array}$$

Moreover, in the three cases we allow for both signs of μ, require $1 \leq \tan\beta \leq 60$ and, to avoid the need for excessive fine–tuning in the EWSB conditions, impose an additional bound on the weak scale parameters, *i.e.* $M_S = M_{\rm EWSB} = \sqrt{m_{\tilde{t}_1} m_{\tilde{t}_2}} < 3$ TeV.

Using the programs `SOFTSUSY` and `SUSpect`, we have performed a full scan of the GMSB, AMSB and mSUGRA scenarios, including the four options "no-scale", "cNMSSM", "VCMSSM" and "NUHM" in the later case. Varying the basic SUSY parameters of the models in the ranges described above, we have determined the maximal M_h value in each scenario. The results for $M_h^{\rm max}$ are shown in Fig. 3.6 as a function of $\tan\beta$, the input parameter that is common to all models. The highest M_h values, defined as that which have 99% of the scan points below it, for any $\tan\beta$ value, are summarised in Table 3.4; one needs to add ≈ 1 GeV to take into account the uncertainties in the SM inputs.

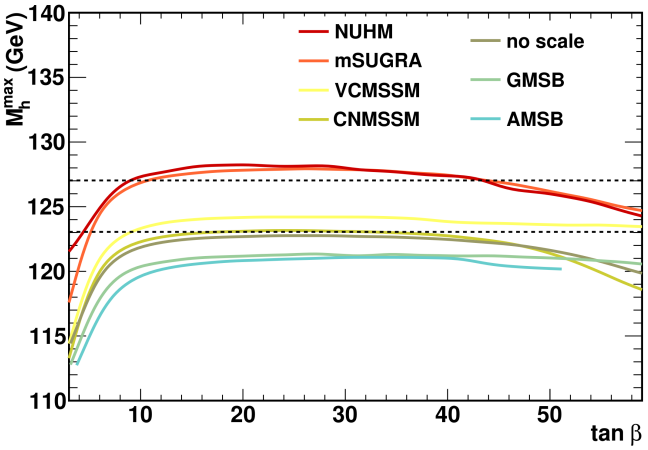

Figure 3.6: The maximal value of the h mass defined as the value for which 99% of the scan points have a mass smaller than it, shown as a function of $\tan\beta$ for the various constrained MSSM models.

model	AMSB	GMSB	mSUGRA	no-scale	cNMSSM	VCMSSM	NUHM
$M_h^{\max}$	121.0	121.5	128.0	123.0	123.5	124.5	128.5

Table 3.4: Maximal h boson mass (in GeV) in the various constrained MSSM scenarios when scanning over all the input parameters in the ranges described in the text.

In all cases, the maximal M_h value is obtained for $\tan\beta$ around 20. We observe that in the adopted parameter space of the models and with the central values of the SM inputs, the upper h mass value (rounded to the upper half GeV) is $M_h^{\max} = 121$ GeV in AMSB, *i.e.* much less than 125 GeV, while in the GMSB scenario one has $M_h^{\max} = 121.5$ GeV. Thus, clearly, the minimal version of these two scenarios are disfavoured if the lightest CP–even Higgs particle has indeed a mass in the range $123 < M_h < 127$ GeV. In the case of mSUGRA, we obtain a maximal value $M_h^{\max} = 128$ GeV and, thus, some parameter space of the model would still survive the M_h constraint.

The upper bound on M_h in these scenarios can be qualitatively understood by considering in each model the allowed values of the trilinear coupling A_t, which essentially determines the stop mixing parameter X_t and thus the value of M_h for a given scale M_S. In GMSB, one has $A_t \approx 0$ at relatively low scales and its magnitude does not significantly increase in the evolution down to the scale M_S. In AMSB, one has a non-zero A_t that is fully predicted at any renormalisation scale in terms of the Yukawa and gauge couplings; however, the ratio A_t/M_S with M_S determined from the overall SUSY breaking scale $m_{3/2}$ turns out to be rather small. Finally, in the mSUGRA model, since we have allowed A_t to vary in a wide range as $|A_0| \leq 9$ TeV, one can get a large A_t/M_S ratio which leads to a heavier Higgs particle. However, one cannot easily reach A_t values such that $X_t/M_S \approx \sqrt{6}$ so that we are not in the maximal–mixing scenario and the higher upper bound on M_h in the pMSSM is not reached.

In turn, in two particular cases of mSUGRA that we have discussed in addition, the "no–

scale" and the "approximate cNMSSM" scenarios, the upper bound on M_h is much lower than in the more general mSUGRA case and, in fact, barely reaches the value $M_h \approx 123$ GeV. The main reason is that these scenarios involve small values of A_0 at the GUT scale, $A_0 \approx 0$ for no–scale and $A_0 \approx -\frac{1}{4} m_{1/2}$ for the cNMSSM. One then obtains A_t values at the weak scale that are too low to generate a significant stop mixing. Thus, only a very small fraction of the parameter space of these two sub–classes of the mSUGRA model survive if we impose $123 < M_h < 127$ GeV. These models hence should have a very heavy spectrum as a value $M_S \gtrsim 3$ TeV is required to increase $M_h^{\rm max}$. In the VCMSSM, $M_h \simeq 124.5$ GeV can be reached as $|A_0|$ can be large for large m_0, $A_0 \approx -m_0$, allowing at least for intermediate stop mixing.

Finally, since the NUHM is more general than mSUGRA as we have two more free parameters, the $(\tan\beta, M_h)$ area is larger than in the mSUGRA case. However, since we are in the decoupling regime and the value of M_A does not matter much (as long as it a larger than a few hundred GeV) and the key weak scale parameters entering the determination of M_h, *i.e.* $\tan\beta, M_S$ and A_t are approximately the same in both models, one obtains a bound $M_h^{\rm max}$ that is only slightly higher in NUHM compared to mSUGRA. Thus, the same discussion above on the mSUGRA scenario, holds also true in the NUHM case.

Benchmark mixing scenarios

As we just discussed, we defined the SUSY breaking scale M_S to be the geometric average of the two stop masses (that we take $\lesssim 3$ TeV not to introduce excessive fine-tuning)

$$M_S = \sqrt{m_{\tilde{t}_1} m_{\tilde{t}_2}} \tag{3.5}$$

and introduced the mixing parameter X_t in the stop sector (that we assume $\lesssim 3M_S$),

$$X_t = A_t - \mu \cot\beta. \tag{3.6}$$

The radiative corrections have a much larger impact and maximise the h boson mass in the so–called "maximal mixing" scenario, where the trilinear stop coupling in the $\overline{\rm DR}$ scheme is

$$\text{maximal mixing scenario} \; : \quad X_t = \sqrt{6}\, M_S \; . \tag{3.7}$$

In turn, the radiative corrections are much smaller for small values of X_t, *i.e.* in the

$$\text{no mixing scenario} : \quad X_t = 0 \; . \tag{3.8}$$

An intermediate scenario is when X_t is of the same order as M_S which is sometimes called the

$$\text{typical mixing scenario} : \quad X_t = M_S \; . \tag{3.9}$$

These mixing scenarios have been very often used as benchmarks for the analysis of MSSM Higgs phenomenology [152]. The maximal mixing scenario has been particularly privileged since it gives a reasonable estimate of the upper bound on the h boson mass, $M_h^{\rm max}$. We adopt the following values for the parameters entering the pMSSM Higgs sector,

$$A_t = A_b \, , \; M_2 \simeq 2\, M_1 = |\mu| = \frac{1}{5} M_S \, , \; M_3 = 0.8\, M_S \; , \tag{3.10}$$

and vary the basic inputs $\tan\beta$ and M_A. For the values $\tan\beta = 60$ and $M_A = M_S = 3$ TeV and a top quark pole mass of $m_t = 173$ GeV, we would obtain a maximal Higgs mass value $M_h^{\rm max} \approx 135$ GeV for maximal mixing once the full set of known radiative corrections up to two loops is implemented [153]. In the no–mixing and typical mixing scenarios, one obtains much smaller values, $M_h^{\rm max} \approx 120$ GeV and $M_h^{\rm max} \approx 125$ GeV, respectively. Scanning over the soft SUSY breaking parameters, one may increase these $M_h^{\rm max}$ values by up to a few GeV.

In Fig. 3.7, we show the $(M_A, \tan\beta)$ plane for different SUSY breaking scales, $M_S = 1, 2$ and 3 TeV and for the zero, typical and maximal mixing scenarios. As can be seen, the situation changes dramatically depending on the chosen scenario. Still, in the maximal mixing scenario with $M_S = 3$ TeV the size of the M_h band is reduced from above, as in this case, already values $\tan\beta \gtrsim 5$ lead to a too heavy h boson, $M_h \gtrsim 129$ GeV. In turn, for $M_S = 1$ TeV, the entire space left by the LEP2 and CMS Higgs constraints is covered with many points at $\tan\beta \gtrsim 20$ excluded by the flavor constraint. Nevertheless, the possibility with $M_S \approx 1$ TeV will start to be challenged by the search for squarks at the LHC when 30 fb^{-1} of data will be collected by the experiments. In the no–mixing scenario, it is extremely hard to obtain a Higgs mass of $M_h \geq 123$ GeV and all parameters need to be maximised: $M_S = 3$ TeV and $\tan\beta \gtrsim 20$; a small triangle is thus left over, the top of which is challenged by the flavor constraints. The typical mixing scenario resembles to the no–mixing scenario, with the notable difference that for $M_S = 3$ TeV, the entire space not excluded by the LEP2 and CMS constraints allow for an acceptable value of M_h.

Higgs mass constraints on the pMSSM

Most of the pMSSM parameters have only a marginal impact on the MSSM Higgs masses. The maximal value of the h mass, $M_h^{\rm max}$ is then obtained for the following choice of parameters:

i) a decoupling regime with a heavy pseudoscalar Higgs boson, $M_A \sim \mathcal{O}$(TeV);
ii) large values of the parameter $\tan\beta$, $\tan\beta \gtrsim 10$;
iii heavy stops, *i.e.* large M_S and we choose $M_S = 3$ TeV as a maximal value;
iv) a stop trilinear coupling $X_t = \sqrt{6} M_S$.

To obtain a precise determination of $M_h^{\rm max}$ in the pMSSM, we have again used the programs `SOFTSUSY` and `SUSpect` to perform a flat scan of the pMSSM parameter space by allowing its 19 input parameters to vary in an uncorrelated way in the following domains:

$$1 \leq \tan\beta \leq 60\,,\ 50\ {\rm GeV} \leq M_A \leq 3\ {\rm TeV}\,,\ -9\ {\rm TeV} \leq A_f \leq 9\ {\rm TeV}\,,$$
$$50\ {\rm GeV} \leq m_{\tilde{f}_L}, m_{\tilde{f}_R}, M_3 \leq 3\ {\rm TeV}\,,\ 50\ {\rm GeV} \leq M_1, M_2, |\mu| \leq 1.5\ {\rm TeV}. \qquad (3.11)$$

We have discarded points in the parameter space that lead to a non–viable spectrum (such as charge and colour breaking minima which imposes the constraint $A_t/M_s \lesssim 3$) or to unrealistic Higgs masses (such as large $\log(m_{\tilde{g}}/m_{\tilde{t}_{1,2}})$ terms that spoil the radiative corrections to M_h [153]). We select the Higgs mass for which 99% of the scan points give a value smaller than it. The results are shown in Fig. 3.8 where, in the left–hand side, the obtained maximal value of the h boson mass $M_h^{\rm max}$ is displayed as a function of the ratio

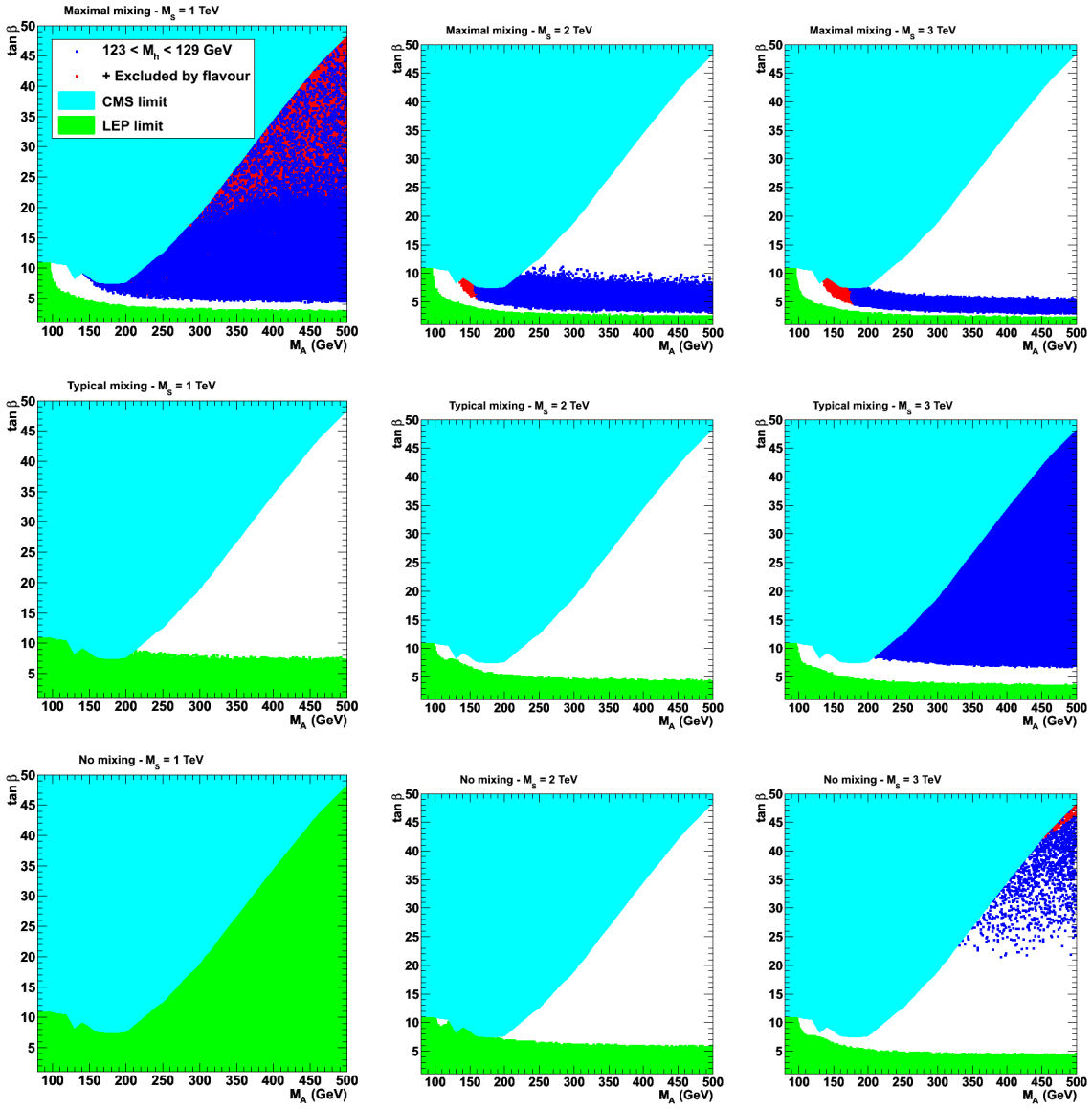

Figure 3.7: The $(M_A, \tan\beta)$ plane for $M_S = 1$, 2 and 3 TeV and for zero, typical and maximal mixing, with the individual constraints from LEP2 (green), CMS $\tau^+\tau^-$ searches (cyan) and flavor physics (red) displayed. The area in which $123 \leq M_H \leq 129$ GeV is also shown (dark blue).

of parameters X_t/M_S. The resulting values are confronted to the mass range

$$123 \text{ GeV} \leq M_h \leq 127 \text{ GeV} . \tag{3.12}$$

Hence, only the scenarios with large X_t/M_S values and, in particular, those close to the maximal mixing scenario $A_t/M_S \approx \sqrt{6}$ survive. The no–mixing scenario is ruled out for

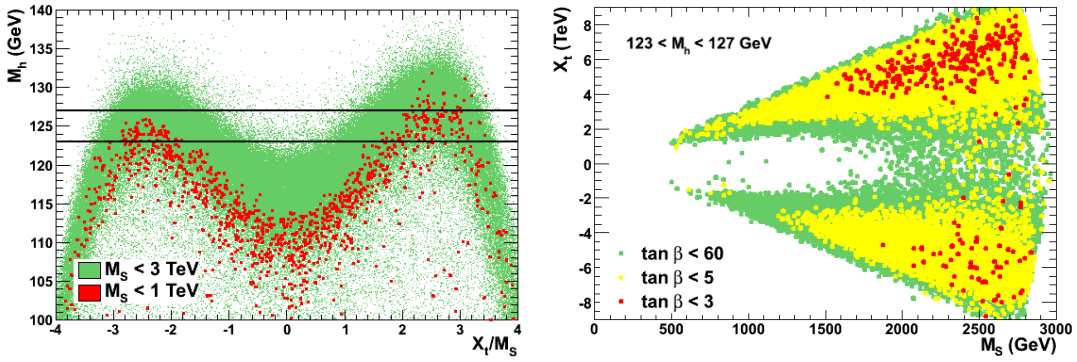

Figure 3.8: The maximal value of the h boson mass as a function of X_t/M_S in the pMSSM when all other soft SUSY breaking parameters and $\tan\beta$ are scanned in the range Eq. (3.11) (left) and the contours for 123< M_h <127 GeV in the (M_S, X_t) plane for some selected range of $\tan\beta$ values (right).

$M_S < 3$ TeV, while the typical mixing scenario needs large M_S and moderate to large $\tan\beta$ values. We obtain $M_h^{\rm max}$=136, 123 and 126 GeV in, the maximal, zero and typical mixing scenarios, respectively.

The right–hand side of Fig. 3.8 shows the contours in the (M_S, X_t) plane where we obtain the mass range 123 GeV $< M_h <$ 127 GeV from our pMSSM scan with $X_t/M_S \lesssim 3$; the regions in which $\tan\beta \lesssim 3, 5$ and 60 are highlighted. One sees again that a large part of the parameter space is excluded if the Higgs mass constraint is imposed.

3.2.2 The various regimes of the pMSSM

The spectrum in the various regimes of the pMSSM Higgs sector depends on the values of M_A and also on $\tan\beta$.

We start from the decoupling regime [154] that has been already mentioned and which in principle occurs for large values of M_A but is reached in practice at $M_A \gtrsim 300$ GeV for low $\tan\beta$ values and already at $M_A \gtrsim M_h^{\rm max}$ for $\tan\beta \gtrsim 10$. In this case, the CP–even h boson reaches its maximal mass value $M_h^{\rm max}$ and its couplings to fermions and gauge bosons (as well as its self–coupling) become SM–like. The heavier H boson has approximately the same mass as the A boson and its interactions are similar, *i.e.* its couplings to gauge bosons almost vanish and the couplings to bottom (top) quarks and τ leptons fermions are (inversely) proportional to $\tan\beta$. Hence, one will have a SM–like Higgs boson $h \equiv H_{\rm SM}$ and two pseudoscalar (like) Higgs particles, $\Phi = H, A$. The $H^\pm$ boson is also degenerate in mass with the A boson and the intensity of its couplings to fermions is similar. Hence, in the decoupling limit, the heavier $H/A/H^\pm$ bosons almost decouple and the MSSM Higgs sector reduces effectively to the SM Higgs sector, but with a light h boson.

The anti–decoupling regime [155] occurs for a light pseudoscalar Higgs boson, $M_A \lesssim M_h^{\rm max}$, and is exactly opposite to the decoupling regime. The roles of the h and H bosons are reversed and at large $\tan\beta$ values, the h boson is degenerate in mass with the pseudoscalar

A, $M_h \simeq M_A$, while the H boson has a mass close to its minimum which is in fact $M_h^{\rm max}$. Because of the upper bound on M_h, all Higgs particles are light. Here, it is the h boson which has couplings close to those of A, $\Phi = h, A$, while the H boson couplings are SM–like, $H \equiv H_{\rm SM}$.

The intense–coupling regime [156] occurs when the mass of the pseudoscalar A boson is close to $M_h^{\rm max}$. In this case, the three neutral Higgs bosons h, H and A (as well as the charged Higgs particles) have comparable masses, $M_h \sim M_H \sim M_A \sim M_h^{\rm max}$. The mass degeneracy is more effective when $\tan\beta$ is large. Here, both the h and H bosons have still enhanced couplings to b–quarks and τ leptons and suppressed couplings to gauge bosons and top quarks, as is the pseudoscalar A. Hence, one approximately has three pseudoscalar like Higgs particles, $\Phi \equiv h, H, A$ with mass differences of the order of 10–20 GeV.

The intermediate–coupling regime occurs for low values of $\tan\beta$, $\tan\beta \lesssim 5$–10, and a not too heavy pseudoscalar Higgs boson, $M_A \lesssim 300$–500 GeV [135]. Hence, we are not yet in the decoupling regime and both CP–even Higgs bosons have non–zero couplings to gauge bosons and their couplings to down–type (up–type) fermions (as is the case for the pseudoscalar A boson) are not strongly enhanced (suppressed) since $\tan\beta$ is not too large. This scenario is already challenged by LEP2 data which call for moderately large values of $\tan\beta$.

The vanishing–coupling regime occurs for relatively large values of $\tan\beta$ and intermediate to large M_A values, as well as for specific values of the other MSSM parameters. The latter parameters, when entering the radiative corrections, could lead to a strong suppression of the couplings of one of the CP–even Higgs bosons to fermions or gauge bosons, as a result of the cancellation between tree–level terms and radiative corrections [157]. An example of such a situation is the small $\alpha_{\rm eff}$ scenario which has been used as a benchmark [152] and in which the Higgs to $b\bar{b}$ coupling is strongly suppressed.

Within the plane $(M_A, \tan\beta)$, the parameter space in which the above regimes of the pMSSM Higgs sector occur are displayed in Fig. 3.9. We have chosen the usual maximal mixing scenario with $M_S = 2$ TeV and the other SUSY parameters as in Eq. (3.10), except for the vanishing coupling scenario, where we have scanned over the SUSY parameters, and only $\approx 5 \times 10^{-4}$ of the scanned points fulfil its requirements. The following conditions have been imposed:

$$\begin{aligned}
\text{decoupling regime} &: \cos^2(\beta-\alpha) \leq 0.05 \\
\text{anti}-\text{decoupling regime} &: \cos^2(\beta-\alpha) \geq 0.95 \\
\text{intermediate}-\text{coupling regime} &: 0.05 \leq \cos^2(\beta-\alpha) \leq 0.7, \quad \tan\beta \leq 10 \\
\text{intense}-\text{coupling regime} &: M_A \lesssim 140 \text{ GeV}, \; g^2_{hbb} \text{ and } g^2_{Hbb} \geq 50 \\
\text{vanishing}-\text{coupling regime} &: M_A \gtrsim 200 \text{ GeV}, \; g^2_{hbb} \text{ or } g^2_{hVV} \leq 0.05. \qquad (3.13)
\end{aligned}$$

In addition, in the SUSY regime, some SUSY particles such as the charginos, neutralinos as well as the third generation sleptons and squarks, could be light enough to significantly affect the phenomenology of the MSSM Higgs bosons. For instance, light sparticles could substantially contribute to the loop induced production and decay modes of the lighter h boson [160, 161] and could even appear (in the case of the lightest neutralino) in its decay product.

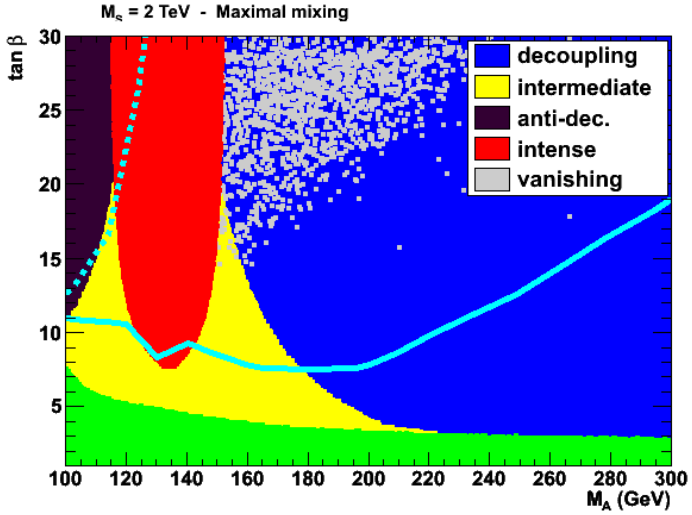

Figure 3.9: Parameter space for the various regimes of the MSSM Higgs sector as defined in the text and in Eq. (3.13) in the $(M_A, \tan\beta)$ plane, in the maximal mixing scenario with $M_S = 2$ TeV. The upper limit constraints from $\Phi \to \tau\tau$ [125] (continuous light blue line) and $t \to H^+ b$ [158] (dashed blue line) searches at the LHC are shown together with the LEP2 excluded region [159] (green area).

3.2.3 Consequences of the Higgs coupling measurements

We consider here the Higgs coupling measurements summarised in Table 3.3.

Anatomy of Higgs-Boson Production and Decay

For illustration, here we provide simple analytic expressions [162], however we use the most advanced calculations including all relevant contributions for our numerical analysis.

An elegant way of obtaining the interactions of a light Higgs boson, is to construct an effective Lagrangian by integrating out heavy degrees of freedom. The resulting effective Higgs boson couplings can be found most easily by utilising low energy theorems, which relate amplitudes with different numbers of zero-momentum Higgs boson fields [163, 164]. Here we will apply this general framework to illustrate the main features of Higgs boson production and decay in the MSSM. In order to present transparent formulas, we will again focus on the leading corrections in the decoupling limit.

In the SM, Higgs boson production via gluon-gluon fusion receives its dominant contribution from triangle diagrams involving top quarks. In the limit of a light Higgs boson, in which we are interested in, the corresponding form factor can be replaced by its asymptotic value

$$F_{1/2}(\tau_t) \approx \lim_{\tau_i \to \infty} F_{1/2}(\tau_i) = 1\,, \tag{3.14}$$

where $\tau_i = 4m_i^2/M_h^2$. In the infinite mass limit, one has furthermore [135]

$$\lim_{\tau_i \to \infty} \frac{F_0(\tau_i)}{F_{1/2}(\tau_i)} = \frac{1}{4}\,. \tag{3.15}$$

with $F_0(\tau_i)$ encoding the effects of scalar loops.

In the MSSM, the modification of the Higgs boson production cross section in $gg \to h$, can be approximated by

$$R_h = \frac{\sigma(gg \to h)_{\rm MSSM}}{\sigma(gg \to h)_{\rm SM}} = (1+\kappa_g)^2 \approx \left(1 + \sum_{i=\tilde{t},\tilde{b}} \kappa_i\right)^2, \tag{3.16}$$

where $\kappa_{\tilde{t}}$ and $\kappa_{\tilde{b}}$ represent the effects of top-squark and bottom-squark triangles, respectively. Notice that Eq. (3.16) ignores the fact that the top-quark and bottom-quark Yukawa couplings in the MSSM differ from those in the SM. As will become clear later on, this mismatch is subleading in the M_Z^2/M_A^2 expansion, and hence can be neglected for our purposes.

The power of the Higgs low energy theorems arises from the fact that in the decoupling limit the corrections $\kappa_{\tilde{t},\tilde{b}}$ can be simply obtained by differentiating the mass-squared matrices $\mathcal{M}^2_{\tilde{t},\tilde{b}}$ with respect to the mass of the corresponding SM quark. For the top squarks, one has

$$\mathcal{M}^2_{\tilde{t}} = \begin{pmatrix} \tilde{m}^2_{Q_3} + m_t^2 + D_{Q_3} & m_t X_t \\ m_t X_t & \tilde{m}^2_{u_3} + m_t^2 + D_{u_3} \end{pmatrix}, \tag{3.17}$$

where $\tilde{m}^2_{Q_3,u_3}$ are soft SUSY breaking masses and $D_{Q_3,u_3} = \mathcal{O}(M_Z^2)$. A similar expression holds in the case of the bottom-squark sector. Ignoring the contributions from the D-terms, which are numerically subleading, the master formula for the top-squark contribution to Eq. (3.16) reads

$$\kappa_{\tilde{t}} \approx \frac{1}{4}\, m_t^2\, \frac{\partial}{\partial m_t^2}\, \ln\left[\det\left(\mathcal{M}^2_{\tilde{t}}\right)\right] \approx \frac{m_t^2}{4}\left(\frac{1}{m^2_{\tilde{t}_1}} + \frac{1}{m^2_{\tilde{t}_2}} - \frac{X_t^2}{m^2_{\tilde{t}_1}\, m^2_{\tilde{t}_2}}\right), \tag{3.18}$$

where the multiplicative factor 1/4 in the first line stems from the normalisation (3.15) of the scalar form factor, and the final result agrees with the expression given in [165, 166]. From Eq. (3.18) one infers that the amount of mixing in the stop sector, parametrised by X_t, determines whether the ratio (3.16) is smaller or larger than 1. For no mixing, one has $R_h \geq 1$, so that Higgs boson production in $gg \to h$ is enhanced with respect to the SM. On the other hand, if X_t is parametrically larger than the mass eigenvalues $m_{\tilde{t}_{1,2}}$ (with $m_{\tilde{t}_1} \leq m_{\tilde{t}_2}$) of Eq. (3.17), then $R_h \leq 1$, meaning that the Higgs boson is less likely to be produced. The fact that in the MSSM, in order to make the Higgs boson sufficiently heavy, one needs large/maximal mixing, *i.e.*, $|X_t| \approx \sqrt{6\, m_{\tilde{t}_1} m_{\tilde{t}_2}}$, then tells us that for a random MSSM parameter point that gives $M_h \approx 126\,\text{GeV}$ one should find a suppression of $\sigma(gg \to h)$. In fact, this is precisely what happens. As a final remark, we add that the sign of the new physics corrections to Higgs boson production in gluon-gluon fusion is in many models closely related to the (non-)cancellation of the quadratic divergence in the Higgs

boson mass [167]. From Eqs. (3.3) and (3.18), we see that in the MSSM there is a strong anti-correlation between M_h and R_h, driven by X_t.

The calculation of the sbottom contribution to R_h proceeds along the lines of Eq. (3.18). Since $m_b^2 \ll m_t^2$, notable effects can only arise if the mixing in the sbottom sector is very large. In this limit, one has approximately

$$\kappa_{\tilde{b}} \approx -\frac{m_b^2 X_b^2}{4 m_{\tilde{b}_1}^2 m_{\tilde{b}_2}^2}\,, \tag{3.19}$$

where $X_b = A_b - \mu \tan\beta$. Obviously, this correction is strictly destructive and can only be important if either the trilinear term A_b and/or the combination $\mu \tan\beta$ is sufficiently larger than the sbottom masses $m_{\tilde{b}_{1,2}}$.

In order to describe the decays of the Higgs boson, we define the corrections factors

$$\frac{\Gamma(h \to VV)_{\rm MSSM}}{\Gamma(h \to VV)_{\rm SM}} = (1+\kappa_V)^2\,, \qquad \frac{\Gamma(h \to f\bar{f})_{\rm MSSM}}{\Gamma(h \to f\bar{f})_{\rm SM}} = (1+\kappa_f)^2\,, \tag{3.20}$$

for $V = W, Z, \gamma$ and $f = b, \tau, t$.

With respect to Eq. (3.18), the derivation of the leading non-decoupling corrections to $\kappa_{V,f}$ is complicated [163, 164, 166] by the fact that in the MSSM one has not a single, but two neutral scalar fields which develop a vacuum expectation value (VEV),

$$H_u = \frac{1}{\sqrt{2}}\left(v_u + \cos\alpha h + \sin\alpha H\right)\,, \qquad H_d = \frac{1}{\sqrt{2}}\left(v_d - \sin\alpha h + \cos\alpha H\right)\,. \tag{3.21}$$

Here $(-\pi/2 \le \alpha \le 0)$

$$\alpha = \frac{1}{2}\arctan\left(\tan(2\beta)\,\frac{M_A^2 + M_Z^2}{M_A^2 - M_Z^2}\right)\,. \tag{3.22}$$

Furthermore, $v_u/v_d = \tan\beta$ and $\sqrt{v_u^2 + v_d^2} = v \approx 246\,\text{GeV}$, so that $v = v_u/\sin\beta = v_d/\cos\beta$.

In the case of κ_W, which encodes the modification of the Higgs boson coupling to a pair of W bosons, the presence of the mixing angle α in Eq. (3.21) leads to

$$\kappa_W = -1 + \frac{v}{M_W}\left(\cos\alpha\,\frac{\partial}{\partial v_u} - \sin\alpha\,\frac{\partial}{\partial v_d}\right) M_W = -1 - \sin(\alpha-\beta) \approx -\frac{M_Z^4}{8M_A^4}\,\sin^2(4\beta)\,, \tag{3.23}$$

where we have used that $M_W = g/2\,\sqrt{v_u^2 + v_d^2}$ and in the last step expanded Eq. (3.22) in powers of M_Z^2/M_A^2, retaining only the first non-zero term in the Taylor series. An analogue formula applies to κ_Z, which implies that the Higgs boson couplings to massive gauge-boson pairs are affected in a universal way, $\kappa_V = \kappa_W = \kappa_Z$. This universal correction of Eq. (3.23) is strictly destructive, but of order M_Z^4/M_A^4, and thus numerically insignificant as long as one sticks to the decoupling limit. Since $\sin^2(4\beta) \propto 1/\tan^2\beta$, it is further reduced in the large-$\tan\beta$ limit.

In the case of the Higgs boson couplings to tau leptons only the second term of the differential operator in Eq. (3.23) contributes because $m_\tau = v_d/\sqrt{2}\,y_\tau$. One obtains

$$\kappa_\tau = -1 - \frac{\sin\alpha}{\cos\beta} \approx -\frac{2M_Z^2}{M_A^2}\,\sin^2\beta\,\cos(2\beta)\,. \tag{3.24}$$

The correction κ_t is obtained from Eq. (3.24) by the replacements $-\sin\alpha \to \cos\alpha$, $\cos\beta \to \sin\beta$, and $\sin^2\beta \to -\cos^2\beta$. Since $m_t = v_u/\sqrt{2}\, y_t$ only the first term in the bracket of Eq. (3.23) results in a correction to κ_t. We see that the shifts in the tree-level couplings of the Higgs boson to fermion pairs fall off quadratically in the limit $M_A^2 \gg M_Z^2$, and that $\kappa_\tau \geq 0$ whereas $\kappa_t \leq 0$. In the large-$\tan\beta$ limit $\kappa_\tau \propto 1$ and $\kappa_t \propto 1/\tan^2\beta$.

The coupling of the Higgs boson to bottom quarks receives important $\tan\beta$-enhanced loop corrections involving charginos and gluinos [43, 168]. In the limit $\tan\beta \gg 1$, we find including the leading terms

$$\kappa_b \approx \frac{1}{1+\epsilon_b \tan\beta} \frac{M_h^2 + (\Delta M_h^2)_{\tilde{t}} + M_Z^2}{M_A^2}\,, \tag{3.25}$$

where the expression for the tree-level Higgs boson mass and the dominant one-loop correction are given in Eqs. (3.2) and (3.3), respectively. Furthermore,

$$\epsilon_b = \frac{\mu A_t}{16\pi^2} \frac{y_t^2}{M_S^2}\, f(x_{\tilde{t}\mu}) + \frac{2\alpha_s}{3\pi} \frac{\mu M_3}{m_{\tilde{b}}^2}\, f(x_{\tilde{b}3}) \tag{3.26}$$

with $x_{\tilde{t}\mu} = M_S^2/\mu^2$, $x_{\tilde{b}3} = m_{\tilde{b}}^2/M_3^2$, and

$$f(x) = -\frac{x}{1-x} - \frac{x}{(1-x)^2}\, \ln x\,. \tag{3.27}$$

Notice that $f(x)$ is positive definite with $f(0) = 0$, $f(1) = 1/2$, and $f(\infty) = 1$. This feature together with the appearance of the combinations μA_t and μM_3 in Eq. (3.26) makes the correction κ_b introduced in Eq. (3.25) quite sensitive to the choice of MSSM parameters. While the modifications $\kappa_{b,t}$ have only a minor impact on Higgs boson production, as already anticipated in Eq. (3.16), we will see below, that the decoupling corrections to κ_b can play an important role for the decays of a light Higgs boson.

In order to give an explicit result for κ_γ, we recall that within the SM, the process $h \to \gamma\gamma$ is dominated by the virtual loop-exchange of W bosons. These contributions interfere destructively with the top-quark amplitude. One has

$$F_W = -\lim_{\tau_i \to \infty} \frac{F_1(\tau_W)}{F_{1/2}(\tau_i)} \approx 6.24\,, \tag{3.28}$$

where $F_1(\tau_i)$ is the form factor associated with vector-boson loops [135] and the numerical result corresponds to our reference value $M_h = 125\,\text{GeV}$ for the Higgs boson mass. With the help of F_W, we write the modification of the Higgs boson coupling to two photons as

$$\kappa_\gamma \approx \frac{1}{F_W - \frac{4}{3}} \left[-\frac{4}{3}\,\kappa_{\tilde{t}} - \frac{1}{3}\,\kappa_{\tilde{b}} - \kappa_{\tilde{\tau}} + \kappa_{H^\pm} + \kappa_{\chi^\pm} \right], \tag{3.29}$$

where the stop and sbottom contributions, *i.e.*, $\kappa_{\tilde{t}}$ and $\kappa_{\tilde{b}}$, have already been given in Eqs. (3.18) and (3.19). Notice that compared to Eq. (3.16) they appear here with opposite signs, signalling that constructive interference in $gg \to h$ goes along with destructive interference in $h \to \gamma\gamma$ and *vice versa*. This correlation between the loop-induced effective hgg

and $h\gamma\gamma$ couplings is a general feature in new physics models with coloured fermionic/scalar partners.

The diphoton channel also receives contributions from stau, charged Higgs boson, and chargino loops. The stau corrections takes the form

$$\kappa_{\tilde{\tau}} \approx -\frac{m_\tau^2 X_\tau^2}{4 m_{\tilde{\tau}_1}^2 m_{\tilde{\tau}_2}^2}\,, \tag{3.30}$$

with $X_\tau = A_\tau - \mu \tan\beta$. Like $\kappa_{\tilde{b}}$ the correction of Eq. (3.30) is only important if the stau-mixing parameter satisfies $X_\tau \gg m_{\tilde{\tau}_{1,2}}$ and the lighter stau mass eigenstate is not too heavy. The former requirement demands both $\tan\beta$ and μ to be large, and in this region of parameter space, stau loops necessarily lead to an enhancement of $\Gamma(h \to \gamma\gamma)$.

The charged Higgs boson effects are, on the other hand, strictly destructive in the MSSM. In the decoupling limit, we find

$$\kappa_{H^\pm} \approx -\frac{1}{4}\left(M_W^2 - \frac{1}{2} M_Z^2 \cos^2(2\beta)\right) \frac{\partial}{\partial M_W^2} \ln\left(M_{H^\pm}^2\right) = -\frac{2M_W^2 - M_Z^2 \cos^2(2\beta)}{8 M_{H^\pm}^2}\,, \tag{3.31}$$

where $M_{H^\pm}^2 = M_A^2 + M_W^2$. Because the spin-zero amplitude $F_0(\tau_i)$ is suppressed by a factor of $1/4$ relative to $F_{1/2}(\tau_i)$ (see Eq. (3.15)), and $M_{H^\pm}^2 \approx M_A^2$ in the decoupling limit, the correction (3.31) has only a very minor effect on the diphoton decay. Note that $\cos^2(2\beta) \to 1$ for $\tan\beta \to \infty$.

The last ingredient in Eq. (3.29) is provided by triangle graphs with internal chargino exchange. In terms of the chargino mass matrix

$$\mathcal{M}_{\chi^\pm} = \begin{pmatrix} M_2 & \sqrt{2} M_W \sin\beta \\ \sqrt{2} M_W \cos\beta & \mu \end{pmatrix}\,, \tag{3.32}$$

the corresponding coefficient can be written as

$$\kappa_{\chi^\pm} \approx -M_W^2 \frac{\partial}{\partial M_W^2} \ln\left[\det\left(\mathcal{M}_{\chi^\pm}^T \mathcal{M}_{\chi^\pm}\right)\right] \approx \text{sign}\left[\det\left(\mathcal{M}_{\chi^\pm}\right)\right] \frac{2M_W^2}{m_{\chi_1^\pm}\, m_{\chi_2^\pm}} \sin(2\beta)\,. \tag{3.33}$$

Since for sufficiently large values of M_2 and μ, one has $\det\left(\mathcal{M}_{\chi^\pm}\right) \approx \mu M_2$, the overall sign of $\kappa_{\chi^\pm}$ is determined by the one of the product of the higgsino and wino mass parameters. It follows that for $\mu M_2 > 0$ ($\mu M_2 < 0$), charginos enhance (suppress) the $h \to \gamma\gamma$ rate. Since $\sin(2\beta) \propto 1/\tan\beta$ the effects are largest for low $\tan\beta$, and numerically very important if the chargino spectrum is light.

When converting the above results into branching ratios, one must bear in mind that the total decay rate $\Gamma(h)$ of a light SM-like Higgs boson is dominated by its decay into bottom quarks. For $M_h = 125\,\text{GeV}$, one has $\text{BR}(h \to b\bar{b}) \approx 60\%$, $\text{BR}(h \to WW) \approx 21\%$, $\text{BR}(h \to gg) \approx 7\%$, $\text{BR}(h \to \tau^+\tau^-) \approx 6\%$, and $\text{BR}(h \to ZZ) \approx 3\%$. It then follows from Eq. (3.20) that

$$R_\Gamma = \frac{\Gamma(h)_{\text{MSSM}}}{\Gamma(h)_{\text{SM}}} \approx 0.60\,(1+\kappa_b)^2 + 0.07\,(1+\kappa_g)^2 + 0.33\,. \tag{3.34}$$

Note that only the shift κ_b has been included here, while the tree-level corrections κ_τ and $\kappa_{W,Z}$ have been neglected. This is a very good approximation, since $\mathrm{BR}(h \to b\bar{b}) \gg \mathrm{BR}(h \to \tau^+\tau^-)$ and Eq. (3.23) is relative to Eq. (3.25) suppressed by an additional power of M_Z^2/M_A^2.

At this point we are ready to work out the products of the production cross section times branching ratios for the various Higgs boson decay channels. These are the key observables that will be affected by the different MSSM contributions. Defining

$$\begin{aligned} \mu_{XX} &= \frac{\big[\sigma(pp \to h)\,\mathrm{BR}(h \to XX)\big]_{\mathrm{MSSM}}}{\big[\sigma(pp \to h)\,\mathrm{BR}(h \to XX)\big]_{\mathrm{SM}}} \\ &\approx \frac{1}{R_\Gamma} \prod_{i=g,X} (1+\kappa_i)^2 \approx 1 + 1.86\,\kappa_g - 1.20\,\kappa_b + 2\,\kappa_X\,, \end{aligned} \tag{3.35}$$

we find the following semi-analytic results for the most interesting final states XX containing either massive vector bosons

$$\mu_{VV} \approx 1 + 0.47 \left(\frac{m_t^2}{m_{\tilde{t}_1}^2} + \frac{m_t^2}{m_{\tilde{t}_2}^2} - \frac{m_t^2 X_t^2}{m_{\tilde{t}_1}^2 m_{\tilde{t}_2}^2} - \frac{m_b^2 X_b^2}{m_{\tilde{b}_1}^2 m_{\tilde{b}_2}^2} \right) - 1.20\,\frac{1}{1+\epsilon_b \tan\beta}\,\frac{M_h^2 + (\Delta M_h^2)_{\tilde{t}} + M_Z^2}{M_A^2}\,, \tag{3.36}$$

where $V = W, Z$ or diphotons

$$\begin{aligned} \mu_{\gamma\gamma} \approx{}& 1 + 0.33 \left(\frac{m_t^2}{m_{\tilde{t}_1}^2} + \frac{m_t^2}{m_{\tilde{t}_2}^2} - \frac{m_t^2 X_t^2}{m_{\tilde{t}_1}^2 m_{\tilde{t}_2}^2} \right) - 0.43\,\frac{m_b^2 X_b^2}{m_{\tilde{b}_1}^2 m_{\tilde{b}_2}^2} + 0.10\,\frac{m_\tau^2 X_\tau^2}{m_{\tilde{\tau}_1}^2 m_{\tilde{\tau}_2}^2} \\ &+ 1.63\,\mathrm{sign}\,(\mu M_2)\,\frac{M_W^2}{m_{\chi_1^\pm}\, m_{\chi_2^\pm}}\,\frac{1}{\tan\beta} - 1.20\,\frac{1}{1+\epsilon_b\tan\beta}\,\frac{M_h^2 + (\Delta M_h^2)_{\tilde{t}} + M_Z^2}{M_A^2}\,. \end{aligned} \tag{3.37}$$

The result for the relative signal strength μ_{bb} of the $b\bar{b}$ channel is obtained from Eq. (3.36) by simply replacing -1.20 by 0.80. In order to obtain the above expressions we have included all non-decoupling corrections, *i.e.*, Eqs. (3.18), (3.19), (3.30), and Eq. (3.33), but apart from Eq. (3.25) neglected all contributions that vanish in the limit $M_A^2 \gg M_Z^2$. We furthermore took the limit $\tan\beta \to \infty$, keeping only the leading corrections, and for simplicity replaced $\mathrm{sign}\left[\det\left(\mathcal{M}_{\chi^\pm}\right)\right]$ by $\mathrm{sign}\,(\mu M_2)$. We also remark that measurements of the double ratio $\mu_{\gamma\gamma}/\mu_{WW,ZZ} \approx 1 + 2\,\kappa_\gamma$ would allow for a clean extraction of the $h \to \gamma\gamma$ amplitude, since it is independent of $\kappa_{\tau,b}$ (see [169] for a recent detailed study).

The formulas (3.36) and (3.37) are the main results. They exhibit interesting correlations with the expressions presented in Section 3.2.1. Focusing first on the correction $(\Delta M_h^2)_{\tilde{t}}$ introduced in Eq. (3.3), we see that in the limit of maximal stop mixing the ratios $\mu_{WW,ZZ}$ and $\mu_{\gamma\gamma}$ are necessarily reduced. In terms of $M_S^2 = m_{\tilde{t}_1} m_{\tilde{t}_2}$, the shift in $\mu_{WW,ZZ}$ ($\mu_{\gamma\gamma}$) is given approximately by $-1.9\,m_t^2/M_S^2$ ($-1.3\,m_t^2/M_S^2$), which amounts to a correction of around -5% (-4%) for $M_S = 1\,\mathrm{TeV}$. Large mixing in the bottom-squark sector will further suppress the latter ratios. The decoupling corrections affecting the Higgs boson couplings to the bottom and tau go in the same direction. Numerically, one finds a universal shift of -2% for $M_A = 1\,\mathrm{TeV}$. Positive corrections to $\mu_{\gamma\gamma}$ can arise from chargino loops if $\mathrm{sign}\,(\mu M_2) = +1$, which helps also to diminish the negative correction $(\Delta M_h^2)_{\tilde{\tau}}$ to the Higgs

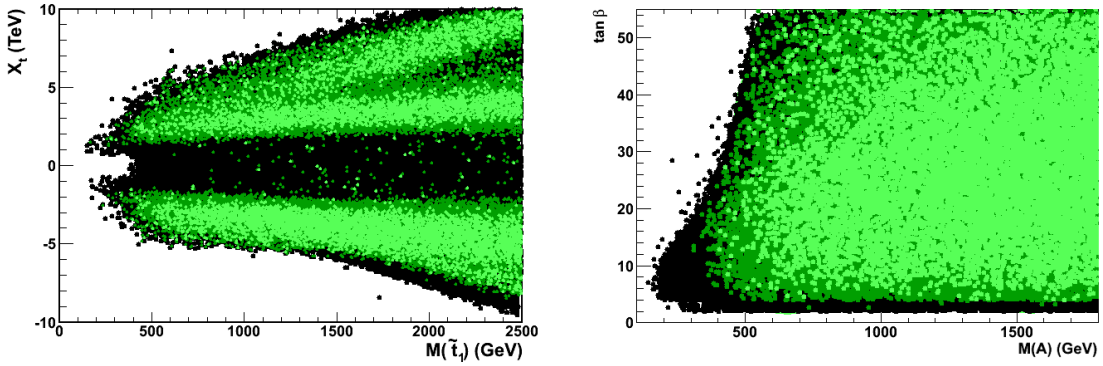

Figure 3.10: Distributions of the pMSSM points in the $(m_{\tilde{t}_1}, X_t)$ (left) and $(M_A, \tan\beta)$ (right) parameter space. The black dots show the selected pMSSM points, those in light (dark) green the same points compatible at 68% (90%) C.L. with the Higgs constraints of Table 3.3.

boson mass. Since Eq. (3.33) is $\tan\beta$-suppressed, there is however a generic tension between large chargino effects in $\mu_{\gamma\gamma}$ and saturating the upper limit on the tree-level Higgs boson mass following from Eq. (3.2). A way to enhance $\mu_{\gamma\gamma}$ without running into immediate problems at the tree level, is provided by a light stau with large mixing $X_\tau \approx \mu \tan\beta$, which requires that both $\tan\beta$ and μ are large. To give an example, employing $m^2_{\tilde{\tau}} = m_{\tilde{\tau}_1} m_{\tilde{\tau}_2} = (200\,\text{GeV})^2$, $\tan\beta = 50$, and $\mu = 1\,\text{TeV}$ in Eq. (3.37), one finds that $\mu_{\gamma\gamma}$ is changed by +50%. Since the correction $(\Delta M_h^2)_{\tilde{b},\tilde{\tau}}$ in Eq. (3.4) is proportional to $-\mu^4/m^2_{\tilde{b},\tilde{\tau}}$, one expects however an anti-correlation between the size of the stau contribution to $\mu_{\gamma\gamma}$ and the loop-corrected Higgs boson mass.

Consequences on the pMSSM

It is interesting to perform an assessment of the compatibility of the LHC and Tevatron data with the MSSM and analyse the region of parameter favoured by the observed boson mass and rate pattern [92,121]. Despite the preliminary character of the results reported by the LHC collaborations and the limited statistical accuracy of these first results, the study is a template for future analyses.

In this analysis, we compute the χ^2 probability on the observable of Table 3.3 for each accepted pMSSM points. For the $b\bar{b}$ and $\tau^+\tau^-$ channels, in which no evidence has been obtained at the LHC, we add the channel contribution to the total χ^2 only when their respective μ value exceeded 1.5 and the pMSSM point becomes increasingly less consistent to the limits reported by CMS. In order to investigate the sensitivity to the inputs, we also compare the results by including or not the $b\bar{b}$, for which a tension exists between the CMS limit and Tevatron results, and the $\tau^+\tau^-$ rate. Fig. 3.10 shows the region of the $(m_{\tilde{t}_1}, X_t)$ and $(M_A, \tan\beta)$ parameter space where pMSSM points are compatible with the input h boson mass and observed yields.

The distributions for some individual parameters which manifest a sensitivity are pre-

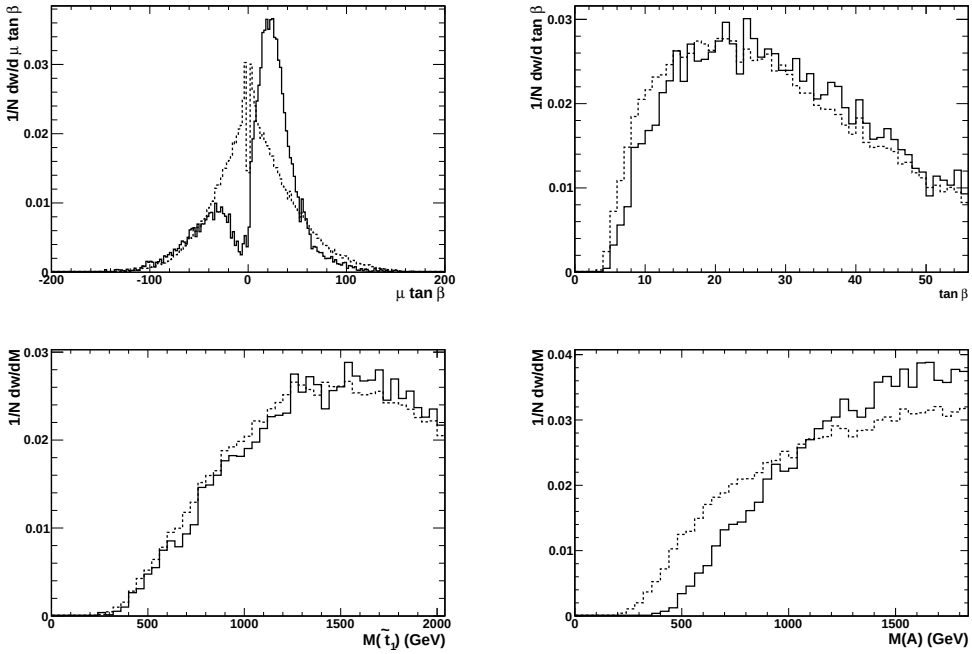

Figure 3.11: The normalised distribution of the values of the $\mu \tan\beta$ (upper left), $\tan\beta$ (upper right), $m_{\tilde{t}_1}$ (lower left) and M_A (lower right) variables for the selected pMSSM points (dashed line) compared to the probability density function for the same variables obtained from the χ^2 probability using M_h, $R_{\gamma\gamma}$ and R_{ZZ} (continuous line). The normalised distributions reflect the biases induced by the Higgs constraints.

sented in Fig. 3.11, where each pMSSM point enters with a weight equal to its χ^2 probability. Points having a probability below 0.15 are not included. The probability weighted distributions obtained from this analysis are compared to the normalised frequency distribution for the same observables obtained for accepted points within the allowed mass region 122.5 $< M_H <$127.5 GeV. We observe that some variables are significantly affected by the constraints applied. Not surprisingly, the observable which exhibits the largest effect is the product $\mu \tan\beta$, for which the data favours large positive values, where the $\gamma\gamma$ branching fraction increases as discussed below. On the contrary, it appears difficult to reconcile an enhancement of both $\mu_{\gamma\gamma}$ and $\mu_{b\bar{b}}$, as would be suggested by the central large value of $\mu_{b\bar{b}} = 1.97 \pm 0.72$ recently reported by the Tevatron experiments [119]. Such an enhancement is not observed by the CMS collaboration and the issue is awaiting the first significant evidence of a boson signal in the $b\bar{b}$ final state at the LHC and the subsequent rate determination. The $\tan\beta$ distribution is also shifted towards larger value as an effect of the Higgs mass and rate values. We also observe a significant suppression of pMSSM points with the pseudoscalar A boson mass below $\sim$450 GeV. This is due to the combined effect of the $A \to \tau^+\tau^-$ direct searches and $B_s \to \mu^+\mu^-$ rate, which constrain the $(M_A, \tan\beta)$ plane to low $\tan\beta$ value

for light A masses, by the shift to $\mu \tan\beta$ from the Higgs rates disfavouring the low $\tan\beta$ region and by the suppression of the non-decoupling regime.

In quantitative terms, we observe that 0.06 (0.50) of the selected pMSSM points are compatible with the constraints given in Table 3.3 at the 68% (90%) confidence level. If we remove the constraint on the upper limit constraint on the $b\bar{b}$ and $\tau^+\tau^-$ rates, the fraction of points accepted at the 90% C.L. does not change significantly, at 0.56, but that at the 68% C.L. doubles to 0.12. On the contrary, if we replace the CMS upper limit for μ_{bb} with the μ_{bb} result of the Tevatron experiments for $M_H = 125$ GeV [119], the fraction of accepted points at 68% C.L. drops below 0.005. This highlights the tension which will be created in the pMSSM by a simultaneous excess in the $\gamma\gamma$ and $b\bar{b}$ channels (see Fig. 3.13).

Sparticle effects on μ_{bb} and $\mu_{\gamma\gamma}$

SUSY particles contribute to the $hb\bar{b}$ coupling as there are additional one–loop vertex corrections that modify the tree–level Lagrangian that incorporates them [157]. These corrections involve bottom squarks and gluinos in the loops, but there are also possibly large corrections from stop and chargino loops. Both can be large since they grow as $\mu \tan\beta$ or $A_t \mu \tan\beta$:

$$\Delta_b \approx \frac{2\alpha_s}{3\pi} \frac{m_{\tilde{g}} \mu \tan\beta}{\max(m^2_{\tilde{g}}, m^2_{\tilde{b}_1}, m^2_{\tilde{b}_2})} + \frac{m_t^2}{8\pi^2 v^2 in^2\beta} \frac{A_t \mu \tan\beta}{\max(\mu^2, m^2_{\tilde{t}_1}, m^2_{\tilde{t}_2})}. \tag{3.38}$$

Outside the decoupling limit, the reduced $b\bar{b}$ couplings of the h state are given in this case by

$$g_{hbb} \approx g_{Abb} \approx \tan\beta(1 - \Delta_b) \tag{3.39}$$

and can be thus significantly reduced or enhanced depending on the sign of μ and, possibly, also A_t. This is exemplified in the left panel of Fig. 3.12, where the ratio $R_{bb} \equiv \text{BR}(h \to b\bar{b})/\text{BR}(H_{\text{SM}} \to b\bar{b})$ is shown as a function of the parameter $\mu \tan\beta$ before the constraints of Table 3.3. The two branches in the histogram are due to the sbottom and stop contributions in which R_{bb} is increased or decreased depending on the sign of μ.

A deviation of the partial $h \to b\bar{b}$ width will enter the total Higgs width, which is dominated by the $b\bar{b}$ channel, and change the R values for the different Higgs decay channels. A reduction of R_{bb} would thus lead to an enhancement of the $\gamma\gamma$ and the WW/ZZ branching fractions. Fig. 3.13 shows the correlation between the bb and $\gamma\gamma$ decays. The values of R_{bb} and $R_{\gamma\gamma}$ shown in the left panel, where we observe a highly anti-correlated variation of the two ratios of branching fraction, R, with the exception of the cases where the opening of the decay $h \to \chi\chi$ suppresses the rates in both channels. These features are still present when considering the μ products with the relevant production cross sections, $gg \to h$ for $\gamma\gamma$ and VH for $b\bar{b}$, as shown in the right panel of Fig. 3.13, with the preliminary results from LHC and the Tevatron overlayed for comparison.

In the case of the $h\gamma\gamma$ decay amplitude, there is the additional SM contribution of the W boson, which is in fact the dominant. Also, it has the opposite sign to that from the top quark and, hence, when stops are light and have a strong mixing, they will tend to increase the $h\gamma\gamma$ amplitude. However, because the W contribution is by far the largest, the stop impact will be much more limited compared to the ggh case and we can expect to have only a

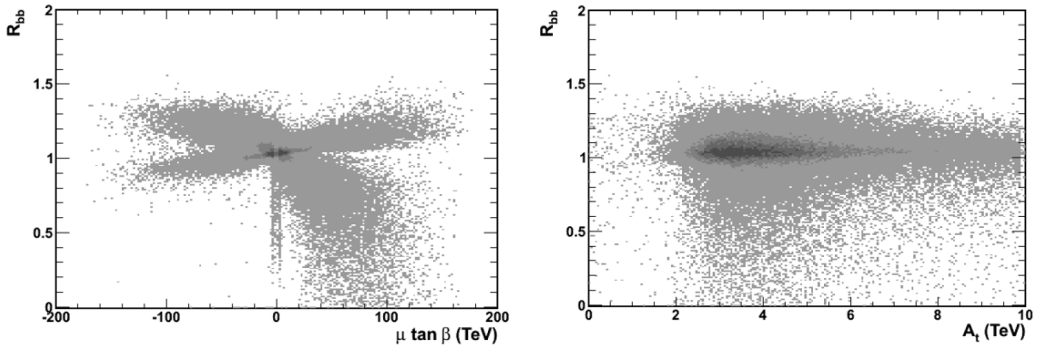

Figure 3.12: R_{bb} values for a sample of pMSSM points as a function of the product of the $\mu \tan\beta$ (left panel) showing the reduction at large values of $\mu \tan\beta$. The reduction in a narrow strip at small values of μ is due to decays into $\chi\chi$. The same as a function of A_t is shown in the right panel.

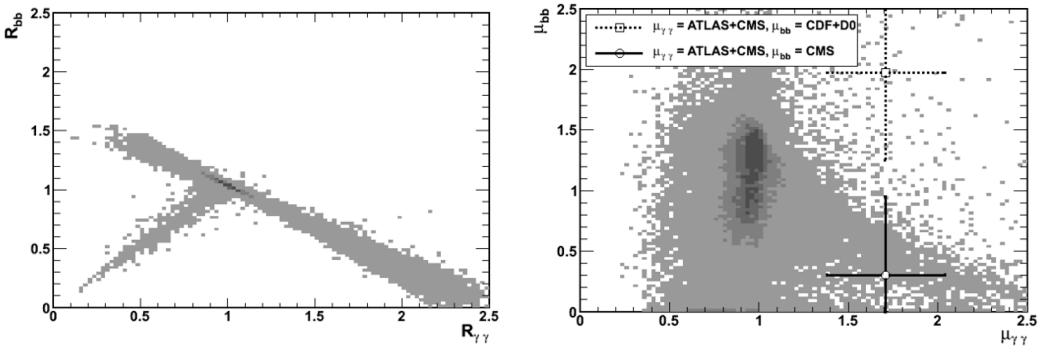

Figure 3.13: R_{bb} as a function of $R_{\gamma\gamma}$ (left panel), showing their anti-correlated variation; the points corresponding to a decrease of both ratios are due to an enhancement of invisible decays to light neutralinos. μ_{bb} as a function of $\mu_{\gamma\gamma}$ (right panel), the anti-correlation is still visible in the region of large $\gamma\gamma$ rate. The values of $\mu_{\gamma\gamma}$ obtained by ATLAS+CMS and μ_{bb} corresponding to the CMS and CDF+D0 searches are overlayed for comparison.

$\approx 10\%$ increase of the $h \to \gamma\gamma$ decay rate for $m_{\tilde{t}_1} \approx 200$ GeV and $X_t \approx 1$ TeV [160,161,170]. Therefore, for light and strongly mixed stops, the cross section times branching ratio $\mu_{\gamma\gamma}$ is always smaller than unity and relatively light stops do not entail an enhancement of the $\gamma\gamma$ yield. The sbottom contribution to the $h\gamma\gamma$ vertex is also very small, for the same reasons discussed above in the case of the hgg amplitude, and also because of its electric charge, $-\frac{1}{3}$ compared to $+\frac{2}{3}$ for stops. Other charged particles can also contribute to the $h \to \gamma\gamma$ rate. The charged Higgs bosons have negligible contributions for $m_{H^\pm} \gtrsim 200$ GeV. Charginos contribute to the $h\gamma\gamma$ vertex and, because of their spin $\frac{1}{2}$ nature, they contribution is only damped by powers of $M_h/m_{\chi^\pm}$. However, the $h\chi^\pm_{1,2}\chi^\mp_{1,2}$ couplings are similar in nature to

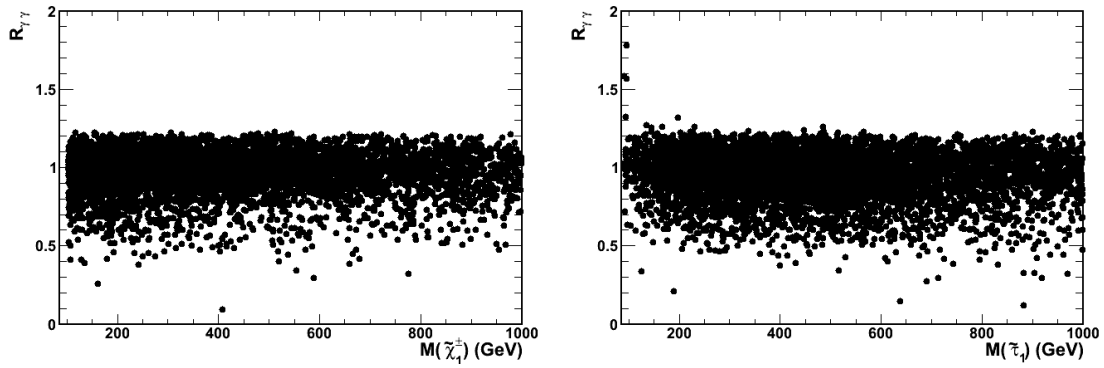

Figure 3.14: $R_{\gamma\gamma}$ values for a sample of pMSSM points as a function of $m_{\chi_1^\pm}$ (left) and ($m_{\tau_1^\pm}$) (right). We impose $R_{bb} > 0.9$, to remove the effects due to the changes of the total width through the bb channel.

those of the LSP given in Eq. (3.40) and cannot be strongly enhanced. As a result we expect contributions at most of the order of 10% even for mass values $m_{\chi_1^\pm} \approx 100$ GeV (see Fig. 3.14). Charged sleptons have in general also little effect on the $h\gamma\gamma$ vertex, with the exception of staus [122, 162]. These behave like the bottom squarks. At very large $\mu \tan\beta$ values, the splitting between the two $\tilde{\tau}$ states becomes significant and their couplings to the h boson large. Since $\tilde{\tau}_1$ can have a mass of the order of a few 100 GeV, without affecting the value of M_h, its contribution to the $h\gamma\gamma$ amplitude may be significant for large values of X_τ as shown in Fig. 3.14.

Invisible Higgs decays

Despite the fact that the discovered particle has a sufficient event rate in visible channels to achieve its observation, it is interesting to consider the regions of parameter space in which invisible Higgs decays occur. This scenario has recently been re-considered in [92, 171]. Besides the value of M_h, the invisible branching ratio BR($h \to \chi_1^0\chi_1^0$) is controlled by four parameters: the gaugino masses M_1 and M_2, the higgsino parameter μ and $\tan\beta$. They enter the 4×4 matrix Z which diagonalises the neutralino mass matrix. They also enter the Higgs coupling to neutralinos which, in the case of the LSP, is

$$g_{h\chi_1^0\chi 10} \propto (Z_{12} - \tan\theta_W Z_{11})\,(\sin\beta Z_{13} + \cos\beta Z_{14}) \tag{3.40}$$

if we assume the decoupling limit not to enhance the $h \to b\bar{b}$ channel which would significantly reduce the invisible decay. In this coupling, Z_{11}, Z_{12} are the gaugino components and Z_{13}, Z_{14} the higgsino components. Thus, the coupling vanishes if the LSP is a pure gaugino, $|\mu| \gg M_1$ leading to $m_{\chi_1^0} \approx M_1$, or a pure higgsino, $M_1 \gg |\mu|$ with $m_{\chi_1^0} \approx |\mu|$.

For the invisible decay to occur, a light LSP, $m_{\chi_1^0} \leq \frac{1}{2} M_h$ is required. Since in the pMSSM, the gaugino mass universality $M_2 \approx 2M_1$ is relaxed, one can thus have a light neutralino without being in conflict with data. The constraint from the Z invisible decay width measured at LEP restricts the parameter space to points where the $\tilde{\chi}_1^0$ is bino-like, if

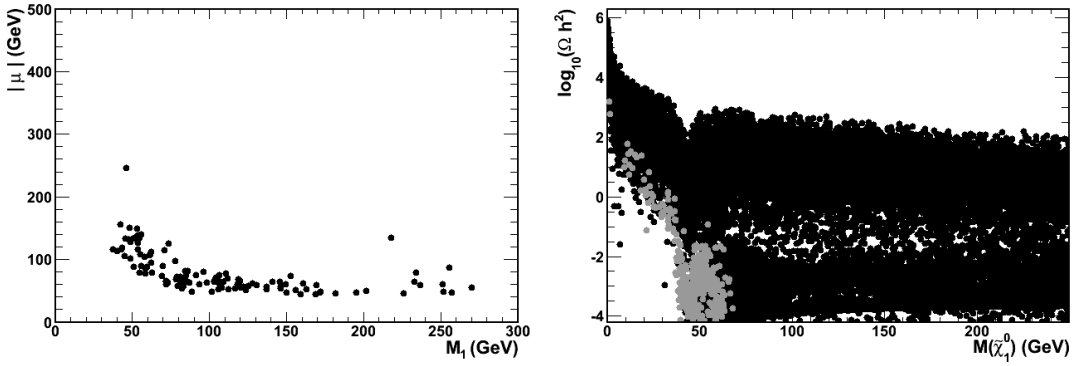

Figure 3.15: Left: Points in the (M_1, μ) parameter space where the invisible branching fraction BR$(h \to \chi_1^0\chi_1^0) \geq 0.15$ from a pMSSM scan where we impose the LEP constraint on the Z invisible width and neutralino relic density $\Omega_\chi h^2$. Right: $\Omega_\chi h^2$ as a function of $m_{\chi_1^0}$ with all the selected pMSSM points in black and those giving a BR$(h \to \chi_1^0\chi_1^0) \geq 0.15$ in grey.

its mass is below 45 GeV, and thus to relatively large values of the higgsino mass parameter $|\mu|$. Since a large decay width into $\tilde{\chi}_1^0\tilde{\chi}_1^0$ corresponds to small values of $|\mu|$, this removes a large part of the parameter space where the invisible Higgs decay width is sizeable. Still, we observe invisible decays for 45 GeV$< M_{\tilde{\chi}^0} < M_h/2$ and $|\mu| < 150$, corresponding to a combination of parameters where the $\tilde{\chi}_1^0$ is a mixed higgsino-gaugino state. These pMSSM points are shown in the (M_1, μ) plane in the left panel of Fig. 3.15.

If the LSP at such a low mass were to be the dark-matter particle, with the relic density given in Eq. (2.25), it should have an efficient annihilation rate into SM particles. The only possible way for that to occur would be $\chi_1^0\chi_1^0$ annihilation through the s–channel light h pole [172] which implies that $m_{\chi_1^0} \lesssim \frac{1}{2}M_h$ to still have a non–zero invisible branching ratio, as shown in the right panel of Fig. 3.15, where the pMSSM points satisfying BR$(h \to \chi_1^0\chi_1^0) \geq 5\%$ are shown in the plane $(m_{\chi_1^0}, \log_{10}(\Omega h^2))$. However, because the partial decay width $\Gamma(h \to \chi_1^0\chi_1^0)$ is suppressed by a factor γ^3 near the $M_h \approx 2m_{\chi_1^0}$ threshold, with the velocity $\gamma = (1 - 4m_{\chi_1^0}^2/M_h^2)^{1/2}$, the invisible branching fraction is rather small if the WMAP dark matter constraint is to hold. MSSM light neutralinos compatible with claims of direct detection dark matter signals are also consistent with collider bounds [93].

We have outlined in this chapter the implications of SUSY searches and the new boson observation by the ATLAS and CMS collaborations for the various MSSM scenarios, including also constraints from flavour physics and dark matter.

Perspectives

This report is a summary of selected parts of my recent work on the MSSM. We have considered the combination of the data from different sectors, namely dark matter searches, LHC Higgs and SUSY searches and flavour physics, which provides important and interesting constraints on SUSY. We have shown that the 19-parameter pMSSM is a very interesting scenario for physics beyond the SM, which is consistent with all the present data from the different sectors.

Our study of the pMSSM will be further developed and we will continue to investigate the properties of the pMSSM parameter space. New data from LHC will be released during the next months, and we will study their impact in the context of the pMSSM. A necessary ingredient to accomplish this task will be to constantly update and improve our machinery, in order to determine the compatibility between the pMSSM and the experimental results from many different sectors. Also, we will analyse in detail the pMSSM scenarios that escape the current LHC searches.

With the discovery of the new particle consistent with the SM Higgs boson, valuable information on new physics has become available. In the next months, my work will be mainly focussed on the consequences of this discovery and of the measurements of its couplings, in order to try to determine whether this discovery could draw a path to new physics.

Scenarios beyond the neutralino dark matter hypothesis are also worth studying. We are currently considering the case of gravitino dark matter in the pMSSM: in this scenario, the LSP, *i.e.* the dark matter particle, is not the neutralino anymore, but the gravitino. The phenomenology at the LHC can be very different in the case of a gravitino LSP, because the NLSP, which is generally not the neutralino and is long-lived, appears at the end of the decay chains. This would result in the production of charged or coloured new particles at the LHC.

Also, the phenomenology of models beyond the MSSM has to be considered. In particular, the NMSSM can be of interest, and extending our analysis machinery in this direction is a complex yet feasible task. A part of my time in the near future will be devoted to this extension. Another possible extension would be to consider CP-violating, NMFV or R-parity violating scenarios.

Depending on the future LHC results, it may be useful to study alternative models beyond the SM, such as extra-dimension scenarios. I already have projects to study the Randall-Sundrum model in light of the recent LHC data.

On the other hand, some part of my work can be devoted to model building and quest for fundamental explanations. This would help suggesting and implementing new experimental

tests on existing and future data. Indeed the enormous amount of data coming from collider physics may contain interesting physics which is not searched for at present.

Concerning software development, both `SuperIso` and `SuperIso Relic` will continue being updated and upgraded. In particular, new observables, such as $B - \bar{B}$ mixings will be soon implemented. Regarding `SuperIso Relic`, we would like to implement the calculation of direct and indirect dark matter detection observables, including several astrophysical and cosmological models, in order to evaluate the influence of astrophysical assumptions. We also intend to extend `SuperIso` to other-than-SUSY models, with automatic calculation of Wilson coefficients and co-annihilation cross-sections, based on `FeynRules`.

Of course, we are in a very special period, where discovery of new physics can be announced at any time. For example new data from the direct and indirect dark matter detection are expected and can give hints about the nature of dark matter. Flavour physics results, and in particular the discovery of the $B_s \to \mu^+\mu^-$ decay, are awaited. From the LHC high-p_T searches, answers to many questions are still hoped for: is the new boson really the SM Higgs? Will the LHC soon find signals for other new particles? All these questions, and the answers that can come from the data, will shape tomorrow's fundamental physics research, and the unexpected is to be expected.

Appendix A

SuperIso

SuperIso [2] is a public program, which offers the possibility to evaluate the most important indirect observables and constraints.

SuperIso was in its first versions devoted to the calculation of the isospin symmetry breaking in $B \to K^*\gamma$ decays in the minimal supersymmetric extension of the Standard Model (MSSM) with minimal flavour violation. This observable imposes stringent constraints on supersymmetric models [173], which justifies a dedicated program. The calculation of the $b \to s\gamma$ branching ratio was also included in the first version and has been improved by adding NNLO contributions since version 2. Also, a broader set of flavour physics observables has been implemented. This includes the branching ratios of $B_{s,d} \to \mu^+\mu^-$, the branching ratio of $B_u \to \tau\nu_\tau$, the branching ratios of $B \to D^0\tau\nu_\tau$ and $B \to D^0 e\nu_e$, the branching ratio of $K \to \mu\nu_\mu$, the branching ratio of $D \to \mu\nu_\mu$, and the branching ratios of $D_s \to \tau\nu_\tau$ and $D_s \to \mu\nu_\mu$, and several observables from the $B \to X_s\ell^+\ell^-$ and $B \to K^*\mu^+\mu^-$ decays. The calculation of the anomalous magnetic moment of the muon is also implemented in the program.

SuperIso has been extended to the general two-Higgs-doublet model since version 2.6 and to the next to minimal supersymmetric extension of the Standard Model (NMSSM) since version 3.0. Also, since version 2.8 an interface with the code HiggsBounds [174] is available[1] in order to obtain direct Higgs search constraints automatically in the output of SuperIso.

SuperIso uses a SUSY Les Houches Accord file (SLHA) [175, 176] as input, which can be either generated automatically by the program via a call to SOFTSUSY [63], ISAJET [177], SPheno [178], SUSpect [99] and NMSSMTools [179], or provided by the user. SuperIso can also use the LHA inspired format for the 2HDM generated by 2HDMC [180]. The program is able to perform the calculations automatically for different types of 2HDM (I–IV), for different supersymmetric scenarios, such as the Constrained MSSM (CMSSM), the Non-Universal Higgs Mass model (NUHM), the Anomaly Mediated Supersymmetry Breaking scenario (AMSB), the Hypercharge Anomaly Mediated Supersymmetry Breaking scenario (HCAMSB), the Mixed Modulus Anomaly Mediated Supersymmetry Breaking scenario (MMAMSB) and the Gauge Mediated Supersymmetry Breaking scenario (GMSB), and

[1] FeynHiggs [100] is necessary to use HiggsBounds with SuperIso.

for the NMSSM scenarios namely CNMSSM, NGMSB and NNUHM. SuperIso is able to generate output files in the Flavour Les Houches Accord (FLHA) format [181].

A.1 Description

SuperIso is a C program respecting the C99 standard, devoted to the calculation of the most constraining flavour physics observables. Several main programs are provided in the package, but the users are also invited to write their own main programs. slha.c can scan files written following the SUSY Les Houches Accord formats, and calculates the corresponding observables. sm.c provides the values of the observables in the Standard Model while thdm.c computes the observables in 2HDM types I–IV and requires 2HDMC [180] for the generation of the input file containing the Higgs masses and couplings. The main programs cmssm.c, amsb.c, hcamsb.c, mmamsb.c, gmsb.c, and nuhm.c have to be linked to at least one of the SOFTSUSY [63], ISASUGRA/ISAJET [177], SPheno [178] and/or SUSpect [99] packages, in order to compute supersymmetric mass spectra and couplings within respectively the CMSSM, AMSB, HCAMSB, MMAMSB, GMSB or NUHM scenarios. The programs cnmssm.c, ngmsb.c, and nnuhm.c have to be linked to the NMSSMTools [179] program to compute supersymmetric mass spectra and couplings within respectively the CNMSSM, NGMSB or NNUHM scenarios. For the general MSSM (or other supersymmetric scenarios) the user has to provide SLHA files containing all the needed masses and couplings.

The computation of the different observables in SuperIso proceeds following three main steps:

- Generation of the SLHA file with ISAJET, SOFTSUSY, SPheno, SuSpect or NMSSMTools (or supply of the SLHA file by the user),
- Scan of the SLHA file,
- Calculation of the observables.

The last point incorporates a complex procedure: to compute the inclusive branching ratio of $b \to s\gamma$ for example, SuperIso needs first to compute the Wilson coefficients at matching scale, and then to evolve them using the Renormalisation Group Equations (RGE) to a lower scale, before using them to compute the branching ratio.

A.2 Main routines

We review the main routines of the code. The complete list of implemented routines can be found in src/include.h, and a precise description of the calculations can be found in the appendices of the SuperIso manual [2].

- `void Init_param(struct parameters* param)`

  This function initialises the param structure, setting all the parameters to 0, apart from the SM masses and couplings, which receive the values given in the PDG [58].

- `int Les_Houches_Reader(char name[], struct parameters* param)`

  This routine reads the SLHA file whose name is contained in `name`, and put all the read parameters in the structure `param`. This function has been updated to the SLHA2 format. This routine can also read the LHA inspired format for the 2HDM described in [2]. A negative value for `param->model` indicates a problem in reading the SLHA file, or a model not yet included in `SuperIso` (such as R-parity breaking models). In this case, `Les_Houches_Reader` returns 0, otherwise 1.

- `int test_slha(char name[])`

  This routine checks if the SLHA file whose name is contained in `name` is valid, and if so return 1. If not, -1 means that in the SLHA generator the computation did not succeed (*e.g.* because of tachyonic particles), -2 means that the considered model is not currently implemented in `SuperIso`, and -3 that the file provided is either not in the SLHA format, or some important elements are missing.

- `int isajet_cmssm(double m0, double m12, double tanb, double A0, double sgnmu, double mtop, char name[])`

- `int isajet_gmsb(double Lambda, double Mmess, double tanb, int N5, double cGrav, double sgnmu, double mtop, char name[])`

- `int isajet_amsb(double m0, double m32, double tanb, double sgnmu, double mtop, char name[])`

- `int isajet_mmamsb(double alpha, double m32, double tanb, double sgnmu, double mtop, char name[])`

- `int isajet_hcamsb(double alpha, double m32, double tanb, double sgnmu, double mtop, char name[])`

- `int isajet_nuhm(double m0, double m12, double tanb, double A0, double mu, double mA, double mtop, char name[])`

  The above routines call `ISAJET` to compute the mass spectrum corresponding to the input parameters, and return an SLHA file whose name has to be specified in the string `name`. It should however be noted `isajet_gmsb`, `isajet_amsb`, `isajet_mmamsb`, `isajet_hcamsb` and `isajet_nuhm` only work with `ISAJET v7.80` or later versions.

- `int softsusy_cmssm(double m0, double m12, double tanb, double A0, double sgnmu, double mtop, double mbot, double alphas_mz, char name[])`

- `int softsusy_gmsb(double Lambda, double Mmess, double tanb, int N5, double cGrav, double sgnmu, double mtop, double mbot, double alphas_mz, char name[])`

- `int softsusy_amsb(double m0, double m32, double tanb, double sgnmu, double mtop, double mbot, double alphas_mz, char name[])`

- `int softsusy_nuhm(double m0, double m12, double tanb, double A0, double mu, double mA, double mtop, double mbot, double alphas_mz, char name[])`
- `int softsusy_mssm(double m1, double m2, double m3, double tanb, double mA, double at, double ab, double atau, double mu, double mer, double mel, double mstaul, double mstaur, double mql, double mq3l, double mqur, double mqtr, double mqdr, double mqbr, double Q, double mtop, double mbot, double alphas_mz, char name[])`

  The above routines call `SOFTSUSY` to compute the mass spectrum corresponding to the input parameters, and return an SLHA file whose name has to be specified in the string `name`.

- `int spheno_cmssm(double m0, double m12, double tanb, double A0, double sgnmu, double mtop, double mbot, double alphas_mz, char name[])`
- `int spheno_gmsb(double Lambda, double Mmess, double tanb, int N5, double sgnmu, double mtop, double mbot, double alphas_mz, char name[])`
- `int spheno_amsb(double m0, double m32, double tanb, double sgnmu, double mtop, double mbot, double alphas_mz, char name[])`

  The above routines call `SPheno` to compute the mass spectrum corresponding to the input parameters, and return an SLHA file whose name has to be specified in the string `name`.

- `int suspect_cmssm(double m0, double m12, double tanb, double A0, double sgnmu, double mtop, double mbot, double alphas_mz, char name[])`
- `int suspect_gmsb(double Lambda, double Mmess, double tanb, int N5, double sgnmu, double mtop, double mbot, double alphas_mz, char name[])`
- `int suspect_amsb(double m0, double m32, double tanb, double sgnmu, double mtop, double mbot, double alphas_mz, char name[])`
- `int suspect_nuhm(double m0, double m12, double tanb, double A0, double mu, double mA, double mtop, double mbot, double alphas_mz, char name[])`
- `int suspect_mssm(double m1, double m2, double m3, double tanb, double mA, double at, double ab, double atau, double mu, double mer, double mel, double mstaul, double mstaur, double mql, double mq3l, double mqur, double mqtr, double mqdr, double mqbr, double Q, double mtop, double mbot, double alphas_mz, char name[])`

  The above routines call `SUSpect` to compute the mass spectrum corresponding to the input parameters, and return an SLHA file whose name has to be specified in the string `name`.

- `int thdmc_types(double l1, double l2, double l3, double l4, double l5, double l6, double l7, double m12_2, double tanb, int type, char name[])`

  This routine calls `2HDMC` to compute the masses and couplings corresponding to the

2HDM input parameters, and returns a LHA inspired file whose name has to be specified in the string `name`.

- `int nmssmtools_cnmssm(double m0, double m12, double tanb, double A0, double lambda, double AK, double sgnmu, double mtop, double mbot, double alphas_mz, char name[])`
- `int nmssmtools_nnuhm(double m0, double m12, double tanb, double A0, double MHDGUT, double MHUGUT, double lambda, double AK, double sgnmu, double mtop, double mbot, double alphas_mz, char name[])`
- `int nmssmtools_ngmsb(double Lambda, double Mmess, double tanb, int N5, double lambda, double AK, double Del_h, double sgnmu, double mtop, double mbot, double alphas_mz, char name[])`

  The above routines call `NMSSMTools` to compute the mass spectrum corresponding to the input parameters and return the SLHA2 file `name`.

- `alphas_running(double Q, double mtop, double mbot, struct parameters* param)`

  This function computes the strong coupling constant at the energy scale `Q` using the parameters in `param`, provided the top quark mass `mtop` and bottom quark mass `mbot` used for the matching between the scales corresponding to different flavour numbers are specified.

- `double running_mass(double quark_mass, double Qinit, double Qfin, double mtop, double mbot, struct parameters* param)`

  This function calculates the running quark mass at the scale `Qfin`, for a quark of mass `quark_mass` at the scale `Qinit` using the structure `param`, knowing the matching scales `mtop` and `mbot`.

- `void CW_calculator(double C0w[], double C1w[], double C2w[], double mu_W, struct parameters* param)`
- `void C_calculator_base1(double C0w[], double C1w[], double C2w[], double mu_W, double C0b[], double C1b[], double C2b[], double mu, struct parameters* param)`
- `void C_calculator_base2(double C0w[], double C1w[], double mu_W, double C0b[], double C1b[], double mu, struct parameters* param)`

  These three routines compute the Wilson coefficients $C_1 \cdots C_{10}$.
  The procedure `CW_calculator` computes the LO contributions to the Wilson coefficients `C0w[]`, the NLO contributions `C1w[]` and the NNLO contributions `C2w[]` at the matching scale `mu_W`, using the parameters of `param`.

  `C_calculator_base1` evolves the LO, NLO and NNLO Wilson coefficients `C0w[]`, `C1w[]`, `C2w[]` initially at scale `mu_W` to `C0b[]`, `C1b[]`, `C2b[]` at scale `mu`, in the standard operator basis.

`C_calculator_base2` evolves the LO and NLO Wilson coefficients `C0w[]`, `C1w[]` initially at scale `mu_W` to `C0b[]`, `C1b[]` at scale `mu`, in the traditional operator basis (see `SuperIso` manual for the definitions).

- `void CQ_calculator(double complex CQ0b[], double complex CQ1b[], double mu_W, double mu, struct parameters* param)`

  This routine computes the Wilson coefficients corresponding to the scalar operators Q_1 and Q_2.

- `void Cprime_calculator(double Cpb[], double complex CQpb[], double mu_W, double mu, struct parameters* param)`

  This routine computes the primed Wilson coefficients (with flipped chirality).

- `int excluded_mass_calculator(char name[])`

  This routine, with the name of the SLHA file in the argument, checks whether the parameter space point is excluded by the collider constraints on the particle masses and if so returns 1. The implemented mass limits are given in Table 3.1, and can be updated by the users in `src/excluded_masses.c` . These limits are valid only in the MSSM.

- `int NMSSM_collider_excluded(char name[])`

- `int NMSSM_theory_excluded(char name[])`

  These two routines only apply to the SLHA file `name` generated by `NMSSMTools`, as they need `NMSSMTools` specific outputs. They respectively check if a parameter space point is excluded by collider constraints [182] or by theoretical constraints (such as unphysical global minimum). The output 1 means that the point is excluded.

- `double higgsbounds_calculator(char name[])`

  The `higgsbounds_calculator` routine, with the name of the SLHA file in the argument, calls `HiggsBounds` to check the direct search constraints on the Higgs masses. If for a given point the result is larger than 1, the point is excluded.

- `int charged_LSP_calculator(char name[])`

  This routine, with the name of the SLHA file in the argument, checks whether the LSP is charged or not. It returns 0 if the LSP is a neutralino, 1 if it is charged, 2 if the LSP is a sneutrino, and 3 if it is a gluino.

- `void flha_generator(char name[], char name_output[])`

  This routine generates an output FLHA file using the input SLHA file. The first argument is the name of the SLHA file and the second of the FLHA file..

The following routines encode the implemented observables:

- `double bsgamma(double C0[], double C1[], double C2[], double mu, double mu_W, struct parameters* param)`

  This function has replaced the calculation of $b \to s\gamma$ in the first version, which was performed at NLO accuracy. Here, knowing the LO, NLO and NNLO Wilson coefficients `C0[]`, `C1[]`, `C2[]` at scale `mu`, and given the matching scale `mu_W` this procedure computes the inclusive branching ratio of $b \to s\gamma$ at NNLO.
  The container routine `bsgamma_calculator`, in which `name` contains the name of the SLHA file, automatises the whole calculation, as it first calls `Init_param` and `Les_Houches_Reader`, then `CW_calculator` and `C_calculator_base1`, and finally `bsgamma`.

- `double delta0(double C0[],double C0_spec[],double C1[],double C1_spec[], struct parameters* param,double mub,double muspec, double lambda_h)`

  This function computes the isospin asymmetry in $B \to K^*\gamma$, using both the LO and NLO parts of the Wilson coefficients at scale `mub` (`C0[]` and `C1[]`), and at the spectator scale `muspec` (`C0_spec[]` and `C1_spec[]`), with the additional input Λ_h in GeV. Compared to the first version, the calculation has been improved, and all the involved integrals have been coded in separate routines. Again, an automatic container routine which only needs the name of the SLHA file is provided: `delta0_calculator`.

- `double Bsmumu(double C0b[], double C1b[], double complex CQ0b[], double complex CQ1b[], double Cpb[], double complex CQpb[],struct parameters* param, double mu_b)`

  `double Bdmumu(double C0b[], double C1b[], double complex CQ0b[], double complex CQ1b[], struct parameters* param, double mu_b)`

  These functions compute the CP-averaged branching ratios of the rare decays $B_s \to \mu^+\mu^-$ and $B_d \to \mu^+\mu^-$ using two loop corrections. The container routines `Bsmumu_calculator (char name[])` and `Bdmumu_calculator (char name[])`, in which `name` contains the name of the SLHA file, automatise the whole calculation, and first call `Init_param` and `Les_Houches_Reader`, then `CW_calculator`, `C_calculator_base1`, `Cprime_calculator`, `CQ_calculator`, and finally `Bsmumu` and `Bdmumu`.

- `double Bsmumu_untag(double C0b[], double C1b[], double complex CQ0b[], double complex CQ1b[], double Cpb[], double complex CQpb[], struct parameters* param, double mu_b)`

  This functions compute the untagged branching ratio of the rare decay $B_s \to \mu^+\mu^-$. The container routine `Bsmumu_untag_calculator` automatises the calculation. The resulting value can be directly compared to the experimental limits.

- `dBR_BXsmumu_dshat(double shat, double C0b[], double C1b[], double C2b[], double complex CQ0b[], double complex CQ1b[], struct parameters* param, double mu_b)`

  `double A_BXsmumu(double shat, double C0b[], double C1b[], double C2b[], double complex CQ0b[], double complex CQ1b[], struct parameters* param, double mu_b)`

These functions compute the differential branching fraction and forward-backward asymmetry of $B \to X_s\mu^+\mu^-$ for $\hat{s}$ =shat using the LO, NLO and NNLO Wilson coefficients C0b/CQ0b, C1b/CQ1b, C2b at scale mu_b. They are called for the calculation of all the $B \to X_s\mu^+\mu^-$ observables.

- BRBXsmumu_lowq2(double C0b[], double C1b[], double C2b[], double complex CQ0b[], double complex CQ1b[], struct parameters* param, double mu_b)

  BRBXsmumu_highq2(double C0b[], double C1b[], double C2b[], double complex CQ0b[], double complex CQ1b[], struct parameters* param, double mu_b)

  double A_BXsmumu_zero(double C0b[], double C1b[], double C2b[], double complex CQ0b[], double complex CQ1b[], struct parameters* param, double mu_b)

  These functions compute the branching fractions in the low q^2 region ($1 < q^2 < 6$ GeV^2), in the high q^2 region ($q^2 > 14.4$ GeV^2), and the zero-crossing of the forward-backward asymmetry of $B \to X_s\mu^+\mu^-$ using the LO, NLO and NNLO Wilson coefficients C0b/CQ0b, C1b/CQ1b, C2b at scale mu_b. Automatic container routines which only need the name of the SLHA file are provided: BRBXsmumu_lowq2_calculator, BRBXsmumu_highq2_calculator and A_BXsmumu_zero_calculator.

- BRBXstautau_highq2(double C0b[], double C1b[], double C2b[], double complex CQ0b[], double complex CQ1b[], struct parameters* param, double mu_b)

  This function computes the branching fraction in the high q^2 region ($q^2 > 14.4$ GeV^2) of $B \to X_s\tau^+\tau^-$ using the LO, NLO and NNLO Wilson coefficients C0b/CQ0b, C1b/CQ1b, C2b at scale mu_b. An automatic container routine which only needs the name of the SLHA file is provided: BRBXstautau_highq2_calculator.

- double dGamma_BKstarmumu_dq2(double q2, double obs[][3], double C0b[], double C1b[], double C2b[], double complex CQ0b[], double complex CQ1b[], double Cpb[], double complex CQpb[], struct parameters* param, double mu_b)

  double dAI_BKstarmumu_dq2(double q2, double C0b[], double C1b[], double C2b[], struct parameters* param, double mu_b)

  These functions compute the differential decay rate and isospin asymmetry of $B \to K^*\mu^+\mu^-$ for q^2 =q2 using the LO, NLO and NNLO Wilson coefficients C0b/CQ0b, C1b/CQ1b, C2b and the primed Wilson coefficients Cpb and CQpb at scale mu_b. They are called for the calculation of all the $B \to K^*\mu^+\mu^-$ observables. The array obs contains the values of the observables given in Table A.1.

- double BRBKstarmumu_lowq2(double obs[], double C0b[], double C1b[], double C2b[], double complex CQ0b[], double complex CQ1b[], double Cpb[], double complex CQpb[], struct parameters* param, double mu_b)

  double BRBKstarmumu_highq2(double obs[], double C0b[], double C1b[], double C2b[], double complex CQ0b[], double complex CQ1b[], double Cpb[], double complex CQpb[], struct parameters* param, double mu_b)

	Observable		Observable
`obs[0]`	$q_0^2(A_{FB})$	`obs[9]`	$H_T^{(1)} = P_4$
`obs[1]`	A_{FB}	`obs[10]`	$H_T^{(2)} = P_5$
`obs[2]`	F_L	`obs[11]`	$H_T^{(3)}$
`obs[3]`	F_T	`obs[12]`	α_{K^*}
`obs[4]`	$A_T^{(1)}$	`obs[13]`	A_{Im}
`obs[5]`	$A_T^{(2)} = P_1$	`obs[14]`	P_2
`obs[6]`	$A_T^{(3)}$	`obs[15]`	P_3
`obs[7]`	$A_T^{(4)}$	`obs[16]`	P_6
`obs[8]`	$A_T^{(5)}$		

Table A.1: $B \to K^*\mu^+\mu^-$ observables contained in the array `obs[]`.

These functions compute branching fraction of $B \to K^*\mu^+\mu^-$ as well of all the observables given in Table A.1, in the low q^2 ($1 < q^2 < 6$ GeV^2) and high q^2 ($14.18 < q^2 < 16$ GeV^2) regions respectively, using the LO, NLO and NNLO Wilson coefficients `C0b`/`CQ0b`, `C1b`/`CQ1b`, `C2b` and the primed Wilson coefficients `Cpb` and `CQpb` at scale `mu_b`. The array `obs` contains the values of the observables in the corresponding q^2 region.

The minimum and maximum q^2 values for the averages can be modified using the function:
`double BRBKstarmumu(double smin, double smax, double obs[], double C0b[], double C1b[], double C2b[], double complex CQ0b[], double complex CQ1b[], double Cpb[], double complex CQpb[], struct parameters* param, double mu_b)`

Automatic container routines which need the name of the SLHA file and an array `obs[]` to get the other functions are provided:
`BRobs_BKstarmumu_lowq2_calculator` and `BRobs_BKstarmumu_highq2_calculator`

Specific functions for the observables of Table A.1 can be found in `src/include.h`.

- `double AI_BKstarmumu_lowq2(double C0b[], double C1b[], double C2b[], struct parameters* param, double mu_b)`

  `double AI_BKstarmumu_highq2(double C0b[], double C1b[], double C2b[], struct parameters* param, double mu_b)`

  `double AI_BKstarmumu_zero(double C0b[], double C1b[], double C2b[], struct parameters* param, double mu_b)`

  These functions compute the averaged isospin asymmetries in the low q^2 ($1 < q^2 < 6$ GeV^2) and high q^2 ($14.18 < q^2 < 16$ GeV^2) regions and the isospin asymmetry zero-crossing of $B \to K^*\mu^+\mu^-$ respectively, using the LO, NLO and NNLO Wilson coefficients `C0b`, `C1b`, `C2b` at scale `mu_b`. Automatic container routines which need the name of the SLHA file are provided: `AI_BKstarmumu_lowq2_calculator`,

`AI_BKstarmumu_highq2_calculator` and `AI_BKstarmumu_zero_calculator`

- `double Btaunu(struct parameters* param)`
  `double RBtaunu(struct parameters* param)`
  `double Btaunu_calculator(char name[])`
  `double RBtaunu_calculator(char name[])`

  These routines compute the branching ratio of the leptonic decay $B_u \to \tau\nu_\tau$ and the ratio $\mathrm{BR}(B_u \to \tau\nu_\tau)/\mathrm{BR}(B_u \to \tau\nu_\tau)^{\mathrm{SM}}$. These leptonic decays occur at tree level, and we consider also higher order SUSY corrections to the Yukawa coupling.

- `double BDtaunu(struct parameters* param)`
  `double BDtaunu_BDenu(struct parameters* param)`
  `double BDtaunu_calculator(char name[])`
  `double BDtaunu_BDenu_calculator(char name[])`

  These routines compute the branching ratio of the semileptonic decay $B \to D^0\tau\nu_\tau$ and the ratio $\mathrm{BR}(B \to D^0\tau\nu_\tau)/\mathrm{BR}(B \to D^0 e\nu_e)$. These semileptonic decays occur at tree level, and we consider also higher order SUSY corrections to the Yukawa coupling.

- `double Kmunu_pimunu(struct parameters* param)`
  `double Rmu23(struct parameters* param)`
  `double Kmunu_pimunu_calculator(char name[])`
  `double Rmu23_calculator(char name[])`

  These functions compute the ratio $\mathrm{BR}(K \to \mu\nu_\mu)/\mathrm{BR}(\pi \to \mu\nu_\mu)$ and the observable $R_{\mu 23}$. These leptonic decays occur at tree level, and we consider also higher order SUSY corrections to the Yukawa coupling.

- `double Dstaunu(struct parameters* param)`
  `double Dsmunu(struct parameters* param)`
  `double Dstaunu_pimunu_calculator(char name[])`
  `double Dsmunu_calculator(char name[])`

  These routines compute the branching ratios of the leptonic decays $D_s \to \tau\nu_\tau$ and $D_s \to \mu\nu_\mu$. These leptonic decays occur at tree level, and we consider also higher order SUSY corrections to the Yukawa coupling.

- `double Dmunu(struct parameters* param)`
  `double Dmunu_calculator(char name[])`

  These routines compute the branching ratio of the leptonic decay $D \to \mu\nu_\mu$.

- `double muon_gm2(struct parameters* param)`
  `double muon_gm2_calculator(char name[])`

  These routines compute the muon anomalous magnetic moment (δa_μ) at two loop.

A.3 Results

We briefly illustrate in this section the constraints on the SUSY parameter space that can be obtained using observables calculated with `SuperIso`. In Figs. A.1 and A.2, two examples of the obtained constraints in the CMSSM and NUHM scenarios using `SuperIso v2.3` are displayed. The different areas in the figures correspond to the following observables:

- red region: excluded by the isospin asymmetry,
- blue region: excluded by the inclusive branching ratio of $b \to s\gamma$,
- black hatched region: excluded by the LEP and Tevatron mass limits,
- violet region: excluded by the branching ratio of $B_s \to \mu^+\mu^-$,
- grey hatched region: **favoured** by the anomalous magnetic moment of the muon,
- yellow hatched region: the LSP is charged, therefore disfavoured by cosmology,
- green region: excluded by the branching ratio of $B_u \to \tau\nu_\tau$,
- orange region: excluded by the branching ratio of $B \to D^0\tau\nu_\tau$,
- cyan region: excluded by the branching ratio of $K \to \mu\nu_\mu$.

The allowed interval for each observable is given in [2].

In Fig. A.1, the exclusion regions in the CMSSM parameter plane $(m_{1/2}, m_0)$ for $\tan\beta = 50$, $A_0 = 0$ and $\mu > 0$ are displayed. One can notice that small values of m_0 and $m_{1/2}$ are disfavoured by the observables. The unfilled region in the bottom left corner corresponds to points with tachyonic particles.
In Fig. A.2, the exclusion zones are displayed in the NUHM parameter plane $(M_A, \tan\beta)$ for $m_0 = 500$ GeV, $m_{1/2} = 500$ GeV, $A_0 = 0$ and $\mu = 500$ GeV. Most observables tend to disfavour the high $\tan\beta$ region in this plane. The white top right triangle corresponds to a region where tachyonic particles are encountered.

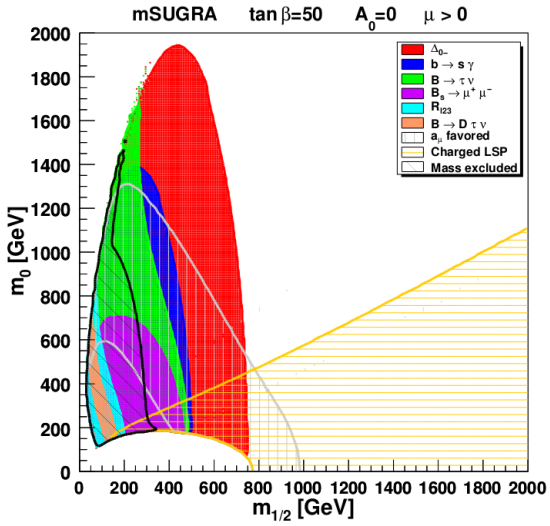

Figure A.1: Constraints in CMSSM $(m_{1/2}, m_0)$ parameter plane. For the description of the various coloured zones see the text. The contours are superimposed in the order given in the legend.

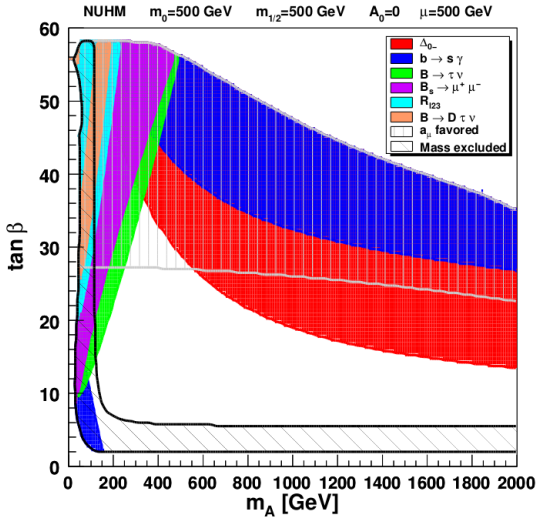

Figure A.2: Constraints in NUHM $(M_A, \tan\beta)$ parameter plane. For the description of the various coloured zones see the text. The contours are superimposed in the order given in the legend.

Appendix B

SuperIso Relic

`SuperIso Relic` [74] is an extension of the `SuperIso` program [2] to the calculation of the relic density. The program calculates the relic density as well as the flavour physics observables using a SUSY Les Houches Accord file (SLHA1 [175] or SLHA2 [176]) as input, either generated automatically via a call to `SOFTSUSY` [63], `ISAJET` [177], `SPheno` [178], `SUSpect` [99] or `NMSSMTools` [179], or provided by the user. The calculation can be performed automatically for different supersymmetry breaking scenarios in the MSSM and in the NMSSM.

One of the most important features of `SuperIso Relic` in comparison to the other public relic density calculation codes, `DarkSUSY` [73], `IsaRed` [183] and `Micromegas` [72], is that it provides the possibility to alter the underlying cosmological model, by modifying for example the radiation equation-of-state, the expansion rate or the thermal properties of the Universe in the period before Big-Bang nucleosynthesis (BBN), which is experimentally inaccessible and remains theoretically obscure, and is interfaced with `AlterBBN` [184] for estimating the BBN constraints on the altered cosmological model. In [82, 83, 185], we studied the effects of different parametrisations of modification of the expansion rate or of the entropy content of the Universe before BBN on the relic density calculation and showed that they can strongly modify the calculated relic density and therefore change the relic density constraints on supersymmetric parameter space. `SuperIso Relic` makes it possible to evaluate the uncertainties on the relic density due to the cosmological model, and inversely, to make prediction on the early Universe properties using the particle physics constraints and the BBN constraints.

B.1 Description

`SuperIso Relic` is a mixed C / Fortran program devoted to the calculation of the relic density in addition to many flavour observables in supersymmetry. Sixteen main programs are provided in the package as guidelines, but the users are also invited to write their own main programs. In particular `slha.c` can scan files written following the SUSY Les Houches

Accord formats, and calculates the implemented observables. The main programs `cmssm.c`, `amsb.c`, `hcamsb.c`, `gmsb.c`, `mmamsb.c`, and `nuhm.c` have to be linked to at least one of the `SOFTSUSY` [63], the `ISASUGRA/ISAJET` [177], the `SPheno` [178] and/or the `SUSpect` [99] packages, in order to compute supersymmetric mass spectra and couplings within respectively the CMSSM, AMSB, HCAMSB, MMAMSB, GMSB or NUHM scenarios for the MSSM. The programs `cnmssm.c`, `ngmsb.c` and `nnuhm.c` have to be linked to `NMSSMTools` [179] to calculate the spectra within the CNMSSM, NGMSB or NNUHM scenarios for the NMSSM.

The main steps to compute the observables in `SuperIso Relic` are given in the following:

- Generation of a SLHA file with a spectrum generator (or supply of a SLHA file by the user),
- Scan of the SLHA file,
- Calculation of the widths of the Higgs bosons with `FeynHiggs` or `Hdecay`,
- Computation of the squared amplitudes of the annihilation diagrams involved in the relic density calculation,
- Computation of the thermally averaged total annihilation cross section,
- Solving of the Boltzmann equations and computation of the relic density,
- Calculation of the flavour physics observables.

It should be noted that the relic density calculation is performed even if the LSP is a charged particle.

The processes involved in the relic density calculation are all the annihilation and co-annihilation processes of the type

$$\tilde{i} + \tilde{j} \to k + l \tag{B.1}$$

where $\tilde{i}, \tilde{j}$ are supersymmetric particles and k, l are Standard Model particles. The number of involved processes is more than 3000 in the MSSM or 5000 in the NMSSM, and the number of diagrams is even larger. To generate all the squared amplitudes, we have written a `Mathematica` [186] script which uses the `LanHEP` [187] Lagrangians in `FeynArts` format, calls `FeynArts` [188] and `FormCalc` [189] and generates the necessary routines for the numerical computation of the amplitudes. These routines are part of `SuperIso Relic` and can be found in `src/relic` and therefore the user does not need to have `Mathematica` or to install other packages. They rely on `FeynHiggs` [100] or `Hdecay` [101] to calculate the widths of the Higgs bosons at two-loop level.
`Hdecay` and `FeynHiggs` are included in the `SuperIso Relic` package. Therefore the user does not need to download these programs separately.

The compilation process of all the needed routines is very long ($\sim$ hour), and their calculation can take time. Fortunately, all the squared amplitude routines are not necessary at the same time, as some processes have only negligible effects. Therefore, all the squared amplitudes are not computed for a SUSY parameter space point, and a selection is performed to save time.

B.2 Main routines

We review here the main routines of the code needed for the relic density calculation. The main procedures related to the flavour observable calculations are given in Appendix A.

The most relevant C routines are the following:

- `void Init_param(struct parameters* param)`

  This function initialises the `param` structure, setting all the parameters to 0, apart from the SM masses and the value of the strong coupling constant at the Z-boson mass, which receive the values given in the PDG [58].

- `int Les_Houches_Reader(char name[], struct parameters* param)`

  This routine reads the SLHA file named `name`, and put all the read parameters in the structure `param`. It should be noted that a negative value for `param->model` indicates a problem in reading the SLHA file, or a model not yet included in `SuperIso` (such as R-parity breaking models). In this case, `Les_Houches_Reader` returns 0, otherwise 1.

- `int test_slha(char name[])`

  This routine checks if the SLHA file is valid, and if so returns 1. If not, -1 means that in the SLHA generator the computation did not succeed (*e.g.* because of tachyonic particles), -2 means that the considered model is not currently implemented in `SuperIso`, and -3 indicates that the provided file is either not in the SLHA format, or some important elements are missing.

- `int softsusy_cmssm(double m0, double m12, double tanb, double A0, double sgnmu, double mtop, double mbot, double alphas_mz, char name[])`
- `int softsusy_nuhm(double m0, double m12, double tanb, double A0, double mu, double mA, double mtop, double mbot, double alphas_mz, char name[])`
- `int softsusy_gmsb(double Lambda, double Mmess, double tanb, int N5, double cGrav, double sgnmu, double mtop, double mbot, double alphas_mz, char name[])`
- `int softsusy_amsb(double m0, double m32, double tanb, double sgnmu, double mtop, double mbot, double alphas_mz, char name[])`

  The above routines call `SOFTSUSY` to compute the mass spectrum corresponding to

the input parameters, and return a SLHA file whose name has to be specified in the string `name`.

- `int isajet_cmssm(double m0, double m12, double tanb, double A0, double sgnmu, double mtop, char name[])`
- `int isajet_gmsb(double Lambda, double Mmess, double tanb, int N5, double cGrav, double sgnmu, double mtop, char name[])`
- `int isajet_nuhm(double m0, double m12, double tanb, double A0, double mu, double mA, double mtop, char name[])`
- `int isajet_amsb(double m0, double m32, double tanb, double sgnmu, double mtop, char name[])`
- `int isajet_mmamsb(double alpha, double m32, double tanb, double sgnmu, double mtop, char name[])`
- `int isajet_hcamsb(double alpha, double m32, double tanb, double sgnmu, double mtop, char name[])`

The above routines call `ISAJET` to compute the mass spectrum corresponding to the input parameters, and return a SLHA file whose name has to be specified in the string `name`.

- `int spheno_cmssm(double m0, double m12, double tanb, double A0, double sgnmu, double mtop, double mbot, double alphas_mz, char name[])`
- `int spheno_gmsb(double Lambda, double Mmess, double tanb, int N5, double sgnmu, double mtop, double mbot, double alphas_mz, char name[])`
- `int spheno_amsb(double m0, double m32, double tanb, double sgnmu, double mtop, double mbot, double alphas_mz, char name[])`

The above routines call `SPheno` to compute the mass spectrum corresponding to the input parameters, and return a SLHA file whose name has to be specified in the string `name`.

- `int suspect_cmssm(double m0, double m12, double tanb, double A0, double sgnmu, double mtop, double mbot, double alphas_mz, char name[])`
- `int suspect_gmsb(double Lambda, double Mmess, double tanb, int N5, double sgnmu, double mtop, double mbot, double alphas_mz, char name[])`

- `int suspect_amsb(double m0, double m32, double tanb, double sgnmu, double mtop, double mbot, double alphas_mz, char name[])`

  The above routines call `SUSpect` to compute the mass spectrum corresponding to the input parameters, and return a SLHA file whose name has to be specified in the string `name`.

- `int nmssmtools_cnmssm(double m0, double m12, double tanb, double A0, double lambda, double AK, double sgnmu, double mtop, double mbot, double alphas_mz, char name[])`
- `int nmssmtools_nnuhm(double m0, double m12, double tanb, double A0, double MHDGUT, double MHUGUT, double lambda, double AK, double sgnmu, double mtop, double mbot, double alphas_mz, char name[])`
- `int nmssmtools_ngmsb(double Lambda, double Mmess, double tanb, int N5, double lambda, double AL, double Del_h, double sgnmu, double mtop, double mbot, double alphas_mz, char name[])`

  The above routines call `NMSSMTools` to compute the mass spectrum corresponding to the input parameters, and return a SLHA file whose name has to be specified in the string `name`.

- `void ModelIni(struct parameters* param, double relicmass, double maxenergy)`

  This routine is an interface between the C routines and the Fortran routines and it defines all the Fortran variables using the C variables.

- `double findrelicmass(struct parameters* param, int *scalar)`

  This function determines the LSP mass, and checks if the LSP is scalar (`*scalar=1`) or fermionic (`*scalar=0`).

- `int Weff(double* res, double sqrtS, struct parameters* param, double relicmass)`

  This function calls the Fortran routines and returns the effective annihilation rate $W_{\rm eff}$ at a given center of mass energy `sqrtS`.

- `int Init_relic(double Wefftab[NMAX][2], int *nlines_Weff, struct parameters* param)`

This routine computes for different values of $\sqrt{s}$ the effective annihilation rates $W_{\rm eff}$ needed for the calculation of $\langle\sigma v\rangle$ using the `Weff` function, and collects them in table `Wefftab`.

- `double sigmav(double T, double relicmass, double Wefftab[NMAX][2], int nlines, struct parameters* param)`

  This function computes the averaged annihilation cross section $\langle\sigma v\rangle$ using the effective annihilation rates $W_{\rm eff}$ collected in table `Wefftab`.

- `double heff(double T, struct relicparam* paramrelic)`
  `double sgstar(double T, struct relicparam* paramrelic)`
  `double geff(double T, struct relicparam* paramrelic)`

  These three functions compute respectively $h_{\rm eff}$, $\sqrt{g_*}$ and $g_{\rm eff}$ at the temperature `T`.

- `double Yeq(double T,struct parameters* param, struct relicparam* paramrelic)`
  `double dYeq_dT(double T,struct parameters* param, struct relicparam* paramrelic)`

  The first function computes Y_{eq} at a temperature `T`, and the second one its derivative.

- `double Tfo(double Wefftab[NMAX][2], int nlines_Weff, double relicmass, struct parameters* param, double d, struct relicparam* paramrelic)`

  This function computes the freeze-out temperature, using the `Wefftab` generated previously.

- `double relic_density(double Wefftab[NMAX][2], int nlines_Weff, struct parameters* param, struct relicparam* paramrelic)`
  `double relic_calculator(char name[])`

  This main procedure computes the relic density using the `Wefftab` generated previously. `relic_calculator` is a container function which scans the SLHA file and computes the relic density.

- `void Init_cosmomodel(struct relicparam* paramrelic)`
  `void Init_modeleff(int model_eff, struct relicparam* paramrelic)`

```
void Init_dark_density(double dd0, double ndd, double T_end, struct
relicparam* paramrelic)
void Init_dark_entropy(double sd0, double nsd, double T_end, struct
relicparam* paramrelic)
```

These procedures define the cosmological model based on which the relic density is computed. `Init_cosmomodel` has to be called first to initialise the `paramrelic` structure. To alter the QCD equation-of-state, `Init_modeleff` must be called while specifying the model: `model_eff`$= 1 \cdots 5$ corresponds respectively to the models A, B, B2, B3 and C developed in [190], and `model_eff`$= 0$ to the older model formerly used in `Micromegas` and `DarkSUSY`, in which the hadrons are considered as ideal gas. If not specified, the model is set by default to B (`model_eff`$= 2$). `Init_dark_density` adds a dark energy density as in Eq. (2.22), with `dd0`$=\kappa_\rho$ and `ndd`$=n_\rho$, `Init_dark_entropy` adds a dark entropy density as in Eq. (2.23) and with `sd0`$=\kappa_s$ and `nsd`$=n_s$. If these routines are not called, no additional density will be added, and the calculation will be performed in the standard cosmological model.

- ```
  double dark_density(double T, struct relicparam* paramrelic)
  double dark_entropy(double T, struct relicparam* paramrelic)
  double dark_entropy_derivative(double T, struct relicparam* paramrelic)
  double dark_entropy_Sigmad(double T, struct relicparam* relicparam)
  ```

  These functions compute energy and entropy densities needed for the alternative cosmological models described in Section 2.1.

- ```
  int FeynHiggs(char name[], struct parameters* param)
  int Hdecay(char name[], struct parameters* param)
  ```

  These routines call `FeynHiggs` or `Hdecay` to compute the widths and masses of the Higgs bosons corresponding to the SLHA file `name` at the two-loop level, and puts these variables in the `param` structure.

The complete list of C procedures implemented in `SuperIso Relic` is available in `src/include.h`.

The Fortran routines can be found in `src/relic`. They have been generated automatically and perform the computation of all squared amplitudes. Because of the large number of these routines they will not be described further here. More information about the `FormCalc` specific routines can be found in the `FormCalc` manual [189].

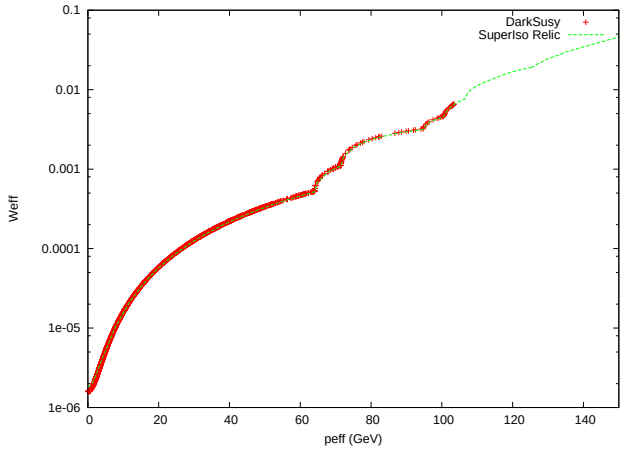

Figure B.1: W_{eff} in function of p_{eff}, computed with `SuperIso Relic` (dashed green line), and with `DarkSUSY` (red crosses). This comparison shows an excellent agreement.

B.3 Results

`SuperIso Relic` computes the relic density, and the results have been compared extensively to those of `DarkSUSY` and `Micromegas`. A very good agreement has been found even at the level of the calculation of the effective annihilation rate W_{eff}, as can be seen in Fig. B.1. In general, the results of `DarkSUSY`, `Micromegas`, and `SuperIso Relic` differ only by a few percent, but in some rare cases where a Higgs resonance occurs approximately at twice the mass of the LSP, the differences can be large. To avoid this problem, a very precise calculation of the masses and widths of the Higgs bosons is required, and we decided to use the two-loop calculations of `FeynHiggs` and `Hdecay` to obtain a better evaluation of the relic density in such cases.

`SuperIso Relic` can also be used in order to constrain SUSY parameter space, as it provides many different observables from flavour physics as well as the relic density. It allows in particular to test easily the influence of the cosmological model by modifying for example the QCD equation-of-state or the expansion rate, as can be seen in Fig. B.2.

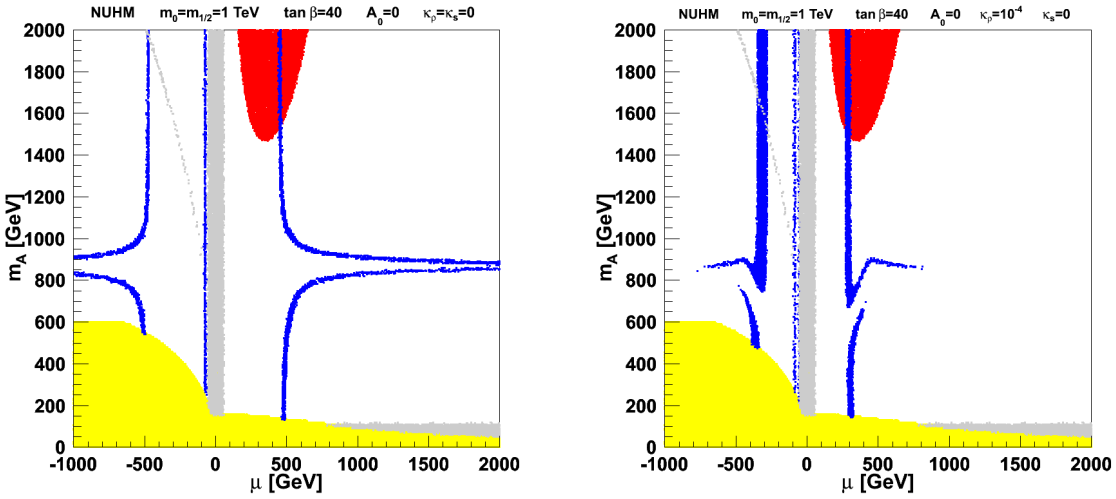

Figure B.2: Constraints on the NUHM parameter plane (μ, M_A), in the standard cosmological model (left), and in presence of a tiny energy overdensity with $\kappa_\rho = 10^{-4}$ and $n_\rho = 6$ (right). The red points are excluded by the isospin asymmetry of $B \to K^*\gamma$, the grey area is excluded by direct collider limits, the yellow zone involves tachyonic particles, and the blue strips are favoured by the WMAP constraints [69].

Bibliography

[1] A. J. Buras, hep-ph/9806471.

[2] F. Mahmoudi, Comput. Phys. Commun. **178** (2008) 745 [arXiv:0710.2067]; F. Mahmoudi, Comput. Phys. Commun. **180** (2009) 1579 [arXiv:0808.3144]; F. Mahmoudi, Comput. Phys. Commun. **180** (2009) 1718; `http://superiso.in2p3.fr` .

[3] G. D'Ambrosio, G. F. Giudice, G. Isidori and A. Strumia, Nucl. Phys. B **645** (2002) 155 [hep-ph/0207036].

[4] T. Hurth, E. Lunghi and W. Porod, Nucl. Phys. B **704** (2005) 56 [hep-ph/0312260].

[5] M. Misiak *et al.*, Phys. Rev. Lett. **98** (2007) 022002 [hep-ph/0609232].

[6] M. Benzke, S. J. Lee, M. Neubert and G. Paz, JHEP **1008** (2010) 099 [arXiv:1003.5012].

[7] P. Gambino and P. Giordano, Phys. Lett. B **669** (2008) 69 [arXiv:0805.0271].

[8] M. Misiak, M. Steinhauser, Nucl. Phys. B **764** (2007) 62 [hep-ph/0609241].

[9] A. L. Kagan and M. Neubert, Phys. Lett. B **539** (2002) 227 [hep-ph/0110078].

[10] S. W. Bosch and G. Buchalla, Nucl. Phys. B **621** (2002) 459 [hep-ph/0106081].

[11] C. Bobeth *et al.*, Phys. Rev. D **64** (2001) 074014 [hep-ph/0104284].

[12] F. Mahmoudi, S. Neshatpour and J. Orloff, JHEP **1208** (2012) 092 [arXiv:1205.1845].

[13] P. Dimopoulos *et al.* [ETM Collaboration], JHEP **1201** (2012) 046 [arXiv:1107.1441].

[14] A. Bazavov *et al.* [Fermilab Lattice and MILC Collaborations], Phys. Rev. D **85** (2012) 114506 [arXiv:1112.3051].

[15] E. T. Neil *et al.* [Fermilab Lattice and MILC Collaborations], PoS LATTICE **2011** (2011) 320 [arXiv:1112.3978].

[16] H. Na, C. J. Monahan, C. T. H. Davies, R. Horgan, G. P. Lepage and J. Shigemitsu, Phys. Rev. D **86** (2012) 034506 [arXiv:1202.4914].

[17] K. de Bruyn, R. Fleischer, R. Knegjens, P. Koppenburg, M. Merk and N. Tuning, Phys. Rev. D **86** (2012) 014027 [arXiv:1204.1735].

[18] K. de Bruyn, R. Fleischer, R. Knegjens, P. Koppenburg, M. Merk, A. Pellegrino and N. Tuning, Phys. Rev. Lett. **109** (2012) 041801 [arXiv:1204.1737].

[19] A. Ghinculov, T. Hurth, G. Isidori and Y. P. Yao, Nucl. Phys. B **685** (2004) 351 [hep-ph/0312128].

[20] T. Huber, T. Hurth and E. Lunghi, Nucl. Phys. B **802** (2008) 40 [arXiv:0712.3009].

[21] Z. Ligeti and F. J. Tackmann, Phys. Lett. B **653** (2007) 404 [arXiv:0707.1694].

[22] F. Kruger, L. M. Sehgal, N. Sinha and R. Sinha, Phys. Rev. D **61** (2000) 114028 [Erratum-ibid. D **63** (2001) 019901] [hep-ph/9907386].

[23] W. Altmannshofer, P. Ball, A. Bharucha, A. J. Buras, D. M. Straub and M. Wick, JHEP **0901** (2009) 019 [arXiv:0811.1214].

[24] F. Kruger and J. Matias, Phys. Rev. D **71** (2005) 094009 [hep-ph/0502060].

[25] U. Egede, T. Hurth, J. Matias, M. Ramon and W. Reece, JHEP **1010** (2010) 056 [arXiv:1005.0571].

[26] C. Bobeth, G. Hiller and G. Piranishvili, JHEP **0807** (2008) 106 [arXiv:0805.2525].

[27] U. Egede, T. Hurth, J. Matias, M. Ramon and W. Reece, JHEP **0811** (2008) 032 [arXiv:0807.2589].

[28] C. Bobeth, G. Hiller and D. van Dyk, JHEP **1007** (2010) 098 [arXiv:1006.5013].

[29] C. Bobeth, G. Hiller and D. van Dyk, JHEP **1107** (2011) 067 [arXiv:1105.0376].

[30] M. Beneke, T. Feldmann and D. Seidel, Nucl. Phys. B **612** (2001) 25 [hep-ph/0106067].

[31] M. Beneke, T. Feldmann and D. Seidel, Eur. Phys. J. C **41** (2005) 173 [hep-ph/0412400].

[32] J. Charles, A. Le Yaouanc, L. Oliver, O. Pene and J. C. Raynal, Phys. Rev. D **60** (1999) 014001 [hep-ph/9812358].

[33] B. Grinstein and D. Pirjol, Phys. Rev. D **70** (2004) 114005 [hep-ph/0404250].

[34] M. Beylich, G. Buchalla and T. Feldmann, Eur. Phys. J. C **71** (2011) 1635 [arXiv:1101.5118].

[35] K. Ikado *et al.*, Phys. Rev. Lett. **97** (2006) 251802 [hep-ex/0604018].

[36] B. Aubert *et al.* [BABAR Collaboration], Phys. Rev. D **76** (2007) 052002 [arXiv:0705.1820].

[37] W.-S. Hou, Phys. Rev. D **48** (1993) 2342.

[38] F. Mahmoudi and O. Stal, Phys. Rev. D **81** (2010) 035016 [arXiv:0907.1791].

[39] A. G. Akeroyd and S. Recksiegel, J. Phys. G **29** (2003) 2311 [hep-ph/0306037].

[40] H. Itoh, S. Komine and Y. Okada, Prog. Theor. Phys. **114** (2005) 179 [hep-ph/0409228].

[41] L. J. Hall, R. Rattazzi and U. Sarid, Phys. Rev. D **50** (1994) 7048 [hep-ph/9306309].

[42] R. Hempfling, Phys. Rev. D **49** (1994) 6168.

[43] M. S. Carena, M. Olechowski, S. Pokorski, and C. E. M. Wagner, Nucl. Phys. B **426** (1994) 269 [hep-ph/9402253].

[44] T. Blazek, S. Raby, and S. Pokorski, Phys. Rev. D **52** (1995) 4151 [hep-ph/9504364].

[45] J. Charles *et al.* [CKMfitter Group Collaboration], Eur. Phys. J. C **41** (2005) 1 [hep-ph/0406184]. Updated results and plots available at: `http://ckmfitter.in2p3.fr`

[46] B. Aubert *et al.* [BABAR Collaboration], Phys. Rev. D **77** (2008) 011107 [arXiv:0708.2260].

[47] I. Adachi *et al.* [Belle Collaboration], arXiv:0809.3834 [hep-ex]; K. Hara *et al.* [Belle Collaboration], arXiv:1006.4201 [hep-ex].

[48] T. Hurth and F. Mahmoudi, Nucl. Phys. B **865** (2012) 461 [arXiv:1207.0688].

[49] R. Aaij *et al.* [LHCb Collaboration], Phys. Rev. Lett. **108** (2012) 231801 [arXiv:1203.4493].

[50] T. Aaltonen *et al.* [CDF Collaboration], Phys. Rev. Lett. **100** (2008) 101802 [arXiv:0712.1708].

[51] LHCb Collaboration, LHCb-CONF-2012-008.

[52] CDF Collaboration, CDF note 10047.

[53] D. Asner *et al.* [Heavy Flavor Averaging Group Collaboration], arXiv:1010.1589 [hep-ex] and online updates at `http://www.slac.stanford.edu/xorg/hfag`.

[54] P. del Amo Sanchez *et al.* [BABAR Collaboration], Phys. Rev. D **82** (2010) 051101 [arXiv:1005.4087].

[55] W. Wang, arXiv:1102.1925 [hep-ex].

[56] B. Aubert *et al.* [BABAR Collaboration], Phys. Rev. Lett. **93** (2004) 081802 [hep-ex/0404006].

[57] M. Iwasaki *et al.* [Belle Collaboration], Phys. Rev. D **72** (2005) 092005 [hep-ex/0503044].

[58] K. Nakamura *et al.* [Particle Data Group], J. Phys. G **37** (2010) 075021 and 2011 partial update for the 2012 edition.

[59] P. Ball, V. M. Braun and A. Lenz, JHEP **0708** (2007) 090 [arXiv:0707.1201].

[60] P. Ball and R. Zwicky, Phys. Rev. D **71** (2005) 014029 [hep-ph/0412079].

[61] P. Ball and R. Zwicky, JHEP **0604** (2006) 046 [hep-ph/0603232].

[62] T. Hurth, G. Isidori, J. F. Kamenik and F. Mescia, Nucl. Phys. B **808** (2009) 326 [arXiv:0807.5039].

[63] B. C. Allanach, Comput. Phys. Commun. **143** (2002) 305 [hep-ph/0104145].

[64] A. G. Akeroyd, F. Mahmoudi and D. Martinez Santos, JHEP **1112** (2011) 088 [arXiv:1108.3018].

[65] S. Chatrchyan *et al.* [CMS Collaboration], Phys. Rev. Lett. **107** (2011) 221804 [arXiv:1109.2352].

[66] CMS Collaboration, CMS-PAS-SUS-12-005.

[67] CMS and LHCb Collaborations, LHCb-CONF-2011-047, CMS-PAS-BPH-11-019.

[68] A. Djouadi and S. Rosiers–Lees (conv.) *et al.*, hep-ph/9901246.

[69] E. Komatsu *et al.* [WMAP Collaboration], Astrophys. J. Suppl. **192** (2011) 18 [arXiv:1001.4538].

[70] S. Burles and D. Tytler, Astrophys. J. **499** (1998) 699 [astro-ph/9712108]; S. Burles and D. Tytler, Astrophys. J. **507** (1998) 732 [astro-ph/9712109].

[71] P. Gondolo and G. Gelmini, Nucl. Phys. B **360** (1991) 145; J. Edsjö and P. Gondolo, Phys. Rev. D **56** (1997) 1879 [hep-ph/9704361].

[72] G. Bélanger *et al.*, Comput. Phys. Commun. **176** (2007) 367 [hep-ph/0607059]; G. Belanger *et al.*, Comput. Phys. Commun. **180** (2009) 747 [arXiv:0803.2360].

[73] P. Gondolo *et al.*, JCAP **0407** (2004) 008 [astro-ph/0406204].

[74] A. Arbey and F. Mahmoudi, Comput. Phys. Commun. **181** (2010) 1277 [arXiv:0906.0369]; A. Arbey and F. Mahmoudi, Comput. Phys. Commun. **182** (2011) 1582; `http://superiso.in2p3.fr/relic/` .

[75] P. Gondolo and G. Gelmini, Nucl. Phys. B **360** (1991) 145.

[76] J. Edsjö and P. Gondolo, Phys. Rev. D **56** (1997) 1879.

[77] B. Ratra and P.J.E. Peebles, Phys. Rev. D **37** (1988) 3406.

[78] C. Armendariz-Picon *et al.*, Phys. Rev. D **63** (2001) 103510 [astro-ph/0006373].

[79] A. Arbey, Phys. Rev. D **74** (2006) 043516 [astro-ph/0601274]; A. Arbey and F. Mahmoudi, Phys. Rev. D **75** (2007) 063513 [hep-th/0703053].

[80] M. Kamionkowski and M.S. Turner, Phys. Rev. D **42** (1990) 3310; F. Rosati, Phys. Lett. B **570** (2003) 5 [hep-ph/0302159]; D. Comelli, M. Pietroni and A. Riotto, Phys. Lett. B **571** (2003) 115 [hep-ph/0302080]; P. Salati, Phys. Lett. B **571** (2003) 121 [astro-ph/0207396]; S. Profumo and P. Ullio, JCAP **0311** (2003) 006 [hep-ph/0309220]; C. Pallis, JCAP **0510** (2005) 015 [hep-ph/0503080]; C. Pallis, Nucl. Phys. B **751** (2006) 129 [hep-ph/0510234]; D.J.H. Chung *et al.*, JHEP **0710** (2007) 016, arXiv:0706.2375 [hep-ph].

[81] V. Barger *et al.*, Phys. Lett. B **566** (2003) 8 [hep-ph/0305075]; N. Okada and O. Seto, Phys. Rev. D **70** (2004) 083531 [hep-ph/0407092].

[82] A. Arbey and F. Mahmoudi, Phys. Lett. B **669** (2008) 46 [arXiv:0803.0741].

[83] A. Arbey and F. Mahmoudi, JHEP **1005** (2010) 051 [arXiv:0906.0368].

[84] A. Arbey, M. Battaglia and F. Mahmoudi, Eur. Phys. J. C **72** (2012) 1847 [arXiv:1110.3726].

[85] Z. Ahmed *et al.* [CDMS-II Collaboration], Science **327** (2010) 1619 [arXiv:0912.3592]; Z. Ahmed *et al.* [CDMS-II Collaboration], Phys. Rev. Lett. **106** (2011) 131302 [arXiv:1011.2482]; E. Armengaud *et al.* [EDELWEISS Collaboration], Phys. Lett. B **702** (2011) 329 [arXiv:1103.4070]; J. Angle *et al.* [XENON10 Collaboration], Phys. Rev. Lett. **107** (2011) 051301 [arXiv:1104.3088]; M. Felizardo, T. A. Girard, T. Morlat, A. C. Fernandes, A. R. Ramos, J. G. Marques, A. Kling and J. Puibasset *et al.*, Phys. Rev. Lett. **108** (2012) 201302 [arXiv:1106.3014]; E. Behnke *et al.* [COUPP Collaboration], Phys. Rev. D **86** (2012) 052001 [arXiv:1204.3094]; D. Y. .Akimov, H. M. Araujo, E. J. Barnes, V. A. Belov, A. Bewick, A. A. Burenkov, V. Chepel and A. Currie *et al.*, Phys. Lett. B **709** (2012) 14 [arXiv:1110.4769]; E. Armengaud *et al.* [EDELWEISS Collaboration], Phys. Rev. D **86** (2012) 051701 [arXiv:1207.1815].

[86] E. Aprile *et al.* [XENON 100 Collaboration], Phys. Rev. Lett. 107 (2011) 131302 [arXiv:1104.2549].

[87] E. Aprile *et al.* [XENON100 Collaboration], arXiv:1207.5988 [astro-ph.CO].

[88] C. Savage, G. Gelmini, P. Gondolo and K. Freese, JCAP **0904** (2009) 010 [arXiv:0808.3607].

[89] C. E. Aalseth *et al.* [CoGeNT Collaboration], Phys. Rev. Lett. **106** (2011) 131301 [arXiv:1002.4703].

[90] G. Angloher, M. Bauer, I. Bavykina, A. Bento, C. Bucci, C. Ciemniak, G. Deuter and F. von Feilitzsch *et al.*, Eur. Phys. J. C **72** (2012) 1971 [arXiv:1109.0702].

[91] G. Jungman, M. Kamionkowski, K. Griest, Phys. Rept. **267** (1996) 195 [hep-ph/9506380].

[92] A. Arbey, M. Battaglia and F. Mahmoudi, Eur. Phys. J. C **72** (2012) 1906 [arXiv:1112.3032].

[93] A. Arbey, M. Battaglia and F. Mahmoudi, Eur. Phys. J. C **72** (2012) 2169 [arXiv:1205.2557].

[94] LEP2 SUSY Working Group, Note LEPSUSYWG/02-04.1.

[95] M. Ackermann *et al.* [Fermi-LAT Collaboration], Phys. Rev. Lett. **107** (2011) 241302 [arXiv:1108.3546].

[96] P. Z. Skands *et al.*, JHEP **07** (2004) 036 [hep-ph/0311123].

[97] B. C. Allanach *et al.*, Comp. Phys. Commun. **180** (2009) 8 [arXiv:0801.0045].

[98] R. Brun, F. Rademakers, Nucl. Instr. Meth. A **389** (1997) 81.

[99] A. Djouadi, J.-L. Kneur, G. Moultaka, Comput. Phys. Commun. **176** (2007) 426 [hep-ph/0211331].

[100] S. Heinemeyer, W. Hollik, G. Weiglein, Comput. Phys. Commun. **124** (2000) 76 [hep-ph/9812320]; S. Heinemeyer, W. Hollik, G. Weiglein, Eur. Phys. J. C **9** (1999) 343 [hep-ph/9812472].

[101] A. Djouadi, J. Kalinowski, M. Spira, Comput. Phys. Commun. **108** (1998) 56 [hep-ph/9704448].

[102] M. Muhlleitner, A. Djouadi, Y. Mambrini, Comput. Phys. Commun. **168** (2005) 46 [hep-ph/0311167].

[103] T. Sjostrand, S. Mrenna, P. Z. Skands, JHEP **0605** (2006) 026 [hep-ph/0603175].

[104] H. Lai *et al.* [CTEQ Collaboration] Eur. Phys. J. C **12** (2000) 375 [hep-ph/9903282].

[105] W. Beenakker, R. Hopker, M. Spira, hep-ph/9611232.

[106] S. Ovyn, X. Rouby, V. Lemaitre, arXiv:0903.2225.

[107] CMS Collaboration, CMS-PAS-HIG-11-009.

[108] CMS Collaboration, CMS-PAS-SUS-11-003.

[109] CMS Collaboration, CMS-PAS-SUS-11-010.

[110] CMS Collaboration, CMS-PAS-SUS-11-011.

[111] M. Cacciari, G. P. Salam, G. Soyez, JHEP **04** (2008) 063 [arXiv:0802.1189].

[112] M. Cacciari, G. P. Salam, Phys. Lett. B **641** (2006) 57 [hep-ph/0512210].

[113] A. L. Read, J. Phys. G **28** (2002) 2693.

[114] G. Bayatian *et al.* [CMS Collaboration], J. Phys. G **34** (2007) 995.

[115] J. A. Conley *et al.*, arXiv:1103.1697.

[116] O. Buchmueller *et al.*, Eur. Phys. J. C **72** (2012) 1878 [arXiv:1110.3568].

[117] ATLAS Collaboration, CERN-PH-EP-2012-167 and F. Gianotti, for the ATLAS Collaboration, CERN Seminar, July 4th, 2012.

[118] CMS Collaboration, CMS PAS HIG-12-020 and J. Incandela, for the CMS Collaboration, CERN Seminar, July 4th, 2012.

[119] The CDF and D0 Collaborations, FERMILAB-CONF-12-318-E.

[120] A. Arbey, M. Battaglia, A. Djouadi, F. Mahmoudi and J. Quevillon, Phys. Lett. B **708** (2012) 162 [arXiv:1112.3028].

[121] A. Arbey, M. Battaglia, A. Djouadi and F. Mahmoudi, JHEP **1209** (2012) 107 [arXiv:1207.1348].

[122] M. Carena, S. Gori, N. R. Shah and C. E. M. Wagner, JHEP **1203** (2012) 014 [arXiv:1112.3336].

[123] H. Baer, V. Barger and A. Mustafayev, Phys. Rev. D **85** (2012) 075010 [arXiv:1112.3017]; S. Heinemeyer, O. Stal and G. Weiglein, Phys. Lett. B **710** (2012) 201 [arXiv:1112.3026]; P. Draper, P. Meade, M. Reece and D. Shih, Phys. Rev. D **85** (2012) 095007 [arXiv:1112.3068]; O. Buchmueller *et al.*, Eur. Phys. J. C **72** (2012) 2020 [arXiv:1112.3564]; S. Akula, B. Altunkaynak, D. Feldman, P. Nath and G. Peim, Phys. Rev. D **85** (2012) 075001 [arXiv:1112.3645]; C. Strege, G. Bertone, D. G. Cerdeno, M. Fornasa, R. R. de Austri and R. Trotta, JCAP **1203** (2012) 030 [arXiv:1112.4192]; C. Beskidt, W. de Boer, D. I. Kazakov and F. Ratnikov, JHEP **1205** (2012) 094 [arXiv:1202.3366]; M. Carena, S. Gori, N. R. Shah, C. E. M. Wagner and L. -T. Wang, JHEP **1207** (2012) 175 [arXiv:1205.5842]; M. W. Cahill-Rowley, J. L. Hewett, A. Ismail and T. G. Rizzo, Phys. Rev. D **86** (2012) 075015 [arXiv:1206.5800].

[124] G. Aad *et al.* [ATLAS Collaboration], Phys. Lett. B **705** (2011) 174 [arXiv:1107.5003].

[125] S. Chatrchyan *et al.* [CMS Collaboration], Phys. Lett. B **713** (2012) 68 [arXiv:1202.4083].

[126] G. Aad *et al.* [ATLAS Collaboration], Phys. Rev. Lett. **106** (2011) 131802 [arXiv:1102.2357].

[127] ATLAS Collaboration, Note ATLAS-CONF-2012-091.

[128] CMS Collaboration, Note CMS PAS HIG-2012-015.

[129] ATLAS Collaboration, Note ATLAS-CONF-2012-092.

[130] CMS Collaboration, Note CMS PAS HIG-2012-016.

[131] CMS Collaboration, Note CMS PAS HIG-2012-019.

[132] CMS Collaboration, Note CMS PAS HIG-2012-018.

[133] S. Dittmaier *et al.*, [LHC Higgs cross section working group], arXiv:1101.0593 [hep-ph].

[134] J. Baglio and A. Djouadi, JHEP **1103** (2011) 055 [arXiv:1012.0530].

[135] A. Djouadi, Phys. Rept. **459** (2008) 1 [hep-ph/0503173].

[136] R. Barate *et al.* [ALEPH Collaboration, DELPHI Collaboration, L3 Collaboration, OPAL Collaboration, and The LEP Working Group for Higgs Boson Searches], Phys. Lett. B **565** (2003) 61 [hep-ex/0306033].

[137] J. A. Casas, J. R. Espinosa, M. Quiros and A. Riotto, Nucl. Phys. B **436** (1995) 3 [Erratum-ibid. B **439** (1995) 466] [hep-ph/9407389].

[138] A. Dabelstein, Z. Phys. C **67** (1995) 495 [hep-ph/9409375].

[139] M. S. Carena, J. R. Espinosa, M. Quiros and C. E. M. Wagner, Phys. Lett. B **355** (1995) 209 [hep-ph/9504316].

[140] M. S. Carena, M. Quiros and C. E. M. Wagner, Nucl. Phys. B **461** (1996) 407 [hep-ph/9508343].

[141] H. E. Haber, R. Hempfling and A. H. Hoang, Z. Phys. C **75** (1997) 539 [hep-ph/9609331].

[142] S. Heinemeyer, W. Hollik and G. Weiglein, Phys. Lett. B **455** (1999) 179 [hep-ph/9903404].

[143] M. S. Carena, H. E. Haber, S. Heinemeyer, W. Hollik, C. E. M. Wagner and G. Weiglein, Nucl. Phys. B **580** (2000) 29 [hep-ph/0001002].

[144] D. M. Pierce, J. A. Bagger, K. T. Matchev and R. j. Zhang, Nucl. Phys. B **491** (1997) 3 [hep-ph/9606211].

[145] A. H. Chamseddine, R. L. Arnowitt and P. Nath, Phys. Rev. Lett. **49** (1982) 970.; R. Barbieri, S. Ferrara and C. A. Savoy, Phys. Lett. B **119** (1982) 343; L. J. Hall, J. D. Lykken and S. Weinberg, Phys. Rev. D **27** (1983) 2359; N. Ohta, Prog. Theor. Phys. **70** (1983) 542.

[146] M. Dine and W. Fishler, Phys. Lett. B **110** (1982) 227; C. Nappi and B. Ovrut, Phys. Lett. B **113** (1982) 1785; L. Alvarez-Gaumé, M. Claudson and M. Wise, Nucl. Phys. B **207** (1982) 96; M. Dine and A. E. Nelson, Phys. Rev. D **48** (1993) 1277 [hep-ph/9303230]; M. Dine, A. E. Nelson and Y. Shirman, Phys. Rev. D **51** (1995) 1362 [hep-ph/9408384]; G. F. Giudice and R. Rattazzi, Phys. Rept. **322** (1999) 419 [hep-ph/9801271].

[147] L. Randall and R. Sundrum, Nucl. Phys. B **557** (1999) 79 [hep-th/9810155]; G. F. Giudice, M. A. Luty, H. Murayama and R. Rattazzi, JHEP **9812** (1998) 027 [hep-ph/9810442]; J. A. Bagger, T. Moroi and E. Poppitz, JHEP **0004** (2000) 009 [hep-th/9911029].

[148] J. Ellis, A. Lahanas, D. Nanopoulos and K. Tamvakis, Phys. Lett. B **134** (1984) 429; J. Ellis, C. Kounnas and D. Nanopoulos, Nucl. Phys. B **241** (1984) 406; A. Benhenni, J. -L. Kneur, G. Moultaka and S. Bailly, Phys. Rev. D **84** (2011) 075015 [arXiv:1106.6325]; T. Li, J. A. Maxin, D. V. Nanopoulos and J. W. Walker, arXiv:1111.4204 [hep-ph].

[149] A. Djouadi *et al.*, JHEP **0807** (2008) 002 [arXiv:0801.4321]; A. Djouadi, U. Ellwanger and A. M. Teixeira, Phys. Rev. Lett. **101** (2008) 101802 [arXiv:0803.0253]; A. Djouadi, U. Ellwanger and A. M. Teixeira, JHEP **0904** (2009) 031 [arXiv:0811.2699].

[150] S.S. AbdusSalam et al., Eur. Phys. J. C **71** (2011) 1835 [arXiv:1109.3859].

[151] J. R. Ellis, T. Falk, K. A. Olive and Y. Santoso, Nucl. Phys. B **652** (2003) 259 [hep-ph/0210205]; H. Baer, A. Mustafayev, S. Profumo, A. Belyaev and X. Tata, Phys. Rev. D **71** (2005) 095008 [hep-ph/0412059]; J. R. Ellis, K. A. Olive and P. Sandick, Phys. Rev. D **78** (2008) 075012 [arXiv:0805.2343]; L. Roszkowski, R. Ruiz de Austri, R. Trotta, Y. -L. S. Tsai and T. A. Varley, Phys. Rev. D **83** (2011) 015014 [arXiv:0903.1279].

[152] M. S. Carena, S. Heinemeyer, C. E. M. Wagner and G. Weiglein, Eur. Phys. J. C **26** (2003) 601 [hep-ph/0202167].

[153] B. Allanach *et al.*, JHEP **0409** (2004) 044 [hep-ph/0406166].

[154] H.E. Haber and Y. Nir, Phys. Lett. B **306** (1993) 327; H.E. Haber, hep-ph/9505240.

[155] J.F. Gunion, A. Stange, S. Willenbrock et al., hep-ph/9602238.

[156] E. Boos et al., Phys. Rev. D **66** (2002) 055004; E. Boos et al., Phys. Lett. B **622** (2005) 311; A. Djouadi and Y. Mambrini, JHEP **0612** (2006) 001; E. Boos, A. Djouadi and A. Nikitenko, Phys. Lett. B **578** (2004) 384.

[157] H. Baer and J. Wells, Phys. Rev. D **57** (1998) 4446; W. Loinaz and J.D. Wells, Phys. Lett. B **445** (1998) 178; K.S. Babu and C.F. Kolda, Phys. Lett. B **451** (1999) 77; M. Carena, S. Mrenna and C.E.M. Wagner, Phys. Rev. D **62** (2000) 055008;

S. Heinemeyer, W. Hollik and G. Weiglein, Eur. Phys. J. C **16** (2000) 139; D. Noth and M. Spira, JHEP **1106** (2011) 084.

[158] G. Aad *et al.* [ATLAS Collaboration], JHEP **1206** (2012) 039 [arXiv:1204.2760].

[159] S. Schael *et al.* [ALEPH and DELPHI and L3 and OPAL and LEP Working Group for Higgs Boson Searches Collaborations], Eur. Phys. J. C **47** (2006) 547 [hep-ex/0602042].

[160] A. Djouadi, Phys. Lett. B **435** (1998) 101 [hep-ph/9806315].

[161] A. Djouadi, V. Driesen, W. Hollik and J. I. Illana, Eur. Phys. J. C **1** (1998) 149 [hep-ph/9612362].

[162] U. Haisch and F. Mahmoudi, arXiv:1210.7806 [hep-ph].

[163] M. Spira, A. Djouadi, D. Graudenz and P. M. Zerwas, Nucl. Phys. B **453** (1995) 17 [hep-ph/9504378].

[164] B. A. Kniehl and M. Spira, Z. Phys. C **69** (1995) 77 [hep-ph/9505225].

[165] R. Dermisek and I. Low, Phys. Rev. D **77** (2008) 035012 [hep-ph/0701235].

[166] G. Cacciapaglia, A. Deandrea and J. Llodra-Perez, JHEP **0906**, 054 (2009) [arXiv:0901.0927].

[167] I. Low, R. Rattazzi and A. Vichi, JHEP **1004**, 126 (2010) [arXiv:0907.5413].

[168] M. S. Carena, D. Garcia, U. Nierste and C. E. M. Wagner, Nucl. Phys. B **577** (2000) 88 [hep-ph/9912516].

[169] A. Djouadi, arXiv:1208.3436 [hep-ph].

[170] A. Arvanitaki and G. Villadoro, JHEP 1202 (2012) 144 [arXiv:1112.4835].

[171] D. Albornoz Vasquez, G. Belanger, R. M. Godbole and A. Pukhov, Phys. Rev. D **85** (2012) 115013 [arXiv:1112.2200].

[172] H. Baer, A. Belyaev, T. Krupovnickas and X. Tata, JHEP **0402** (2004) 007 [hep-ph/0311351]; H. Baer, T. Krupovnickas and X. Tata, JHEP **0406** (2004) 061 [hep-ph/0405058]; A. Djouadi, M. Drees and J.-L. Kneur, Phys. Lett. B **624** (2005) 60; [hep-ph/0504090].

[173] M. R. Ahmady and F. Mahmoudi, Phys. Rev. D **75** (2007) 015007 [hep-ph/0608212].

[174] P. Bechtle *et al.*, Comput. Phys. Commun. **181** (2010) 138 [arXiv:0811.4169]; P. Bechtle *et al.*, Comput. Phys. Commun. **182** (2011) 2605 [arXiv:1102.1898].

[175] P. Z. Skands *et al.*, JHEP **0407** (2004) 036 [hep-ph/0311123].

[176] B. C. Allanach *et al.*, Comput. Phys. Commun. **180** (2009) 8 [arXiv:0801.0045].

[177] H. Baer *et al.*, hep-ph/0312045.

[178] W. Porod, Comput. Phys. Commun. **153** (2003) 275 [hep-ph/0301101].

[179] U. Ellwanger and C. Hugonie, Comput. Phys. Commun. **177** (2007) 399 [hep-ph/0612134]; U. Ellwanger and C. Hugonie, Comput. Phys. Commun. **175** (2006) 290 [hep-ph/0508022].

[180] D. Eriksson, J. Rathsman and O. Stal, Comput. Phys. Commun. **181** (2010) 189 [arXiv:0902.0851].

[181] F. Mahmoudi *et al.*, Comput. Phys. Commun. **183** (2012) 285 [arXiv:1008.0762].

[182] U. Ellwanger, J.F. Gunion and C. Hugonie, JHEP **0507** (2005) 041 [hep-ph/0503203].

[183] H. Baer, C. Balazs and A. Belyaev, JHEP **0203** (2002) 042 [hep-ph/0202076].

[184] A. Arbey, Comput. Phys. Commun. **183** (2012) 1822 [arXiv:1106.1363].

[185] A. Arbey and F. Mahmoudi, Nuovo Cim. C **33N2** (2010) 151 [arXiv:1002.4096].

[186] S. Wolfram, ISBN 1579550223.

[187] A. Semenov, Comput. Phys. Commun. **180** (2009) 431 [arXiv:0805.0555].

[188] T. Hahn, Comput. Phys. Commun. **140** (2001) 418 [hep-ph/0012260]; T. Hahn and C. Schappacher, Comput. Phys. Commun. **143** (2002) 54 [hep-ph/0105349].

[189] T. Hahn and M. Perez-Victoria, Comput. Phys. Commun. **118** (1999) 153 [hep-ph/9807565]; T. Hahn and M. Rauch, Nucl. Phys. Proc. Suppl. **157** (2006) 236 [hep-ph/0601248].

[190] M. Hindmarsh and O. Philipsen, Phys. Rev. D **71** (2005) 087302 [hep-ph/0501232].

Résumé

Des informations sur la nouvelle physique peuvent être extraites de plusieurs secteurs indépendants et en particulier : les recherches directes du Higgs et de nouvelles particules aux collisionneurs, qui sont entrées dans une nouvelle ère avec le démarrage du LHC, les informations indirectes des données de physique des saveurs, en utilisant les résultats obtenus aux usines à B et récemment aussi au LHC, et enfin les informations indirectes sur la densité relique de matière noire et les recherches directes de matière noire, en particulier au vu des résultats récents des expériences XENON, CoGENT, CRESST, ... Combiner les informations des différents secteurs est en effet riche d'implications et permet de réduire l'espace des paramètres des scénarios de nouvelle physique. Nous avons démontré l'existence de telles synergies dans le contexte de la supersymétrie pour différents scénarios contraints ainsi que pour un scénario plus général du MSSM (pMSSM).

Mots-clés : Supersymétrie, Physique des Saveurs, Matière Noire, LHC

Abstract

Information on new physics can be extracted from several independent sectors and in particular: direct search for Higgs and new particles at colliders, which has entered a new era with the start of the LHC, indirect information from flavour physics data, using valuable results obtained at the B factories and recently also at the LHC, and finally indirect information from dark matter relic density and direct dark matter searches using in particular the recent results from XENON, CoGENT, CRESST, ... experiments. Combining the information from the different sectors has indeed very rich implications and allows squeezing the parameters of the new physics scenarios. We have demonstrated such synergies in the context of supersymmetry for various constrained scenarios as well as for a more general MSSM (pMSSM) scenario.

Keywords : Supersymmetry, Flavour Physics, Dark Matter, LHC